THERMAL IDENTIFICATION OF CLANDESTINE BURIALS: A SIGNATURE ANALYSIS AND IMAGE CLASSIFICATION APPROACH

John A. Servello, B.A.

Thesis Prepared for the Degree of

MASTER OF SCIENCE

UNIVERSITY OF NORTH TEXAS

December 2010

APPROVED:

Harrell Gill-King, Major Professor
Samuel F. Atkinson, Committee Member
Thomas L. Beitinger, Committee Member
Arthur J. Goven, Chair of the Department of Biological Sciences
James D. Meernik, Acting Dean of the Robert B. Toulouse School of Graduate Studies

Servello, John A. Thermal identification of clandestine burials: A signature analysis and image classification approach. Master of Science (Biology), December 2010, 170 pp., 73 tables, 62 figures, references, 29 titles.

Clandestine burials, the interred human remains of forensic interest, are generally small features located in isolated environments. Typical ground searches can be both time-consuming and dangerous. Thermal remote sensing has been recognized for some time as a possible search strategy for such burials that are in relatively open areas; however, there is a paucity of published research with respect to this application.

This project involved image manipulation, the analyses of signatures for “graves” of various depths when compared to an undisturbed background, and the use of image classification techniques to tease out these features. This research demonstrates a relationship between the depth of burial disturbance and the resultant signature. Further, image classification techniques, especially object-oriented algorithms, can be successfully applied to single band thermal imagery. These findings may ultimately decrease burial search times for law enforcement and increase the likelihood of locating clandestine graves.

ACKNOWLEDGEMENTS

I would like to thank Mr. Bill Estes and the University of North Texas (UNT) Grounds department, as well as a contingent of friends that helped me prepare the research site. Their donated time and effort was invaluable in the earliest stages.

Special thanks to the flight personnel out of the Texas Department of Public Safety Aircraft Division in Forney, Texas: Assistant Chief John Brannon (ret.), Lieutenant Barry Wind, Sergeant Keith Davis, Sergeant Jim Rohrman, Officer Clay Lacey, and Officer Matt Murphy. Without their time, experience, observation, and dedication, this research would not have been possible.

Thanks go to Dr. Bruce Hunter and his staff at the UNT Center for Spatial Analysis, who provided both valuable advice and access to some of the software required for this study.

Thanks are due to Dr. A. Frank Servello, for his assistance with the site map survey techniques, and for his continuing motivations.

Lastly, thanks to the members of my committee for their continuing support, advice and guidance throughout this process.

This project was partially funded by the UNT Department of Biological Sciences Beth Baird Scholarship Fund. Thank you for selecting me and for providing the funding for much of the equipment (tools, computers, software, *etc.*) needed in this research.

TABLE OF CONTENTS

LIST OF TABLES

LIST OF FIGURES

CHAPTER 1

INTRODUCTION

This research examined the potential use of airborne thermal scanners to locate simulated clandestine graves. Clandestine graves are the unauthorized burials of deceased persons of forensic interest (France et al. 1992), and are generally small features measuring one by two meters or less that consist of disturbed soil and human remains (Killam 1990). Previous research has suggested that such disturbances typically appear relatively cooler than the surrounding non-disturbed soil following the completion of active exothermic decomposition (France et al. 1997; unreferenced 2006 personal correspondence with J Stremersch).

The U.S. Department of Justice states a prevalence of "as many as 100,000 active missing persons cases in the United States," with a yearly incidence of "tens of thousands of people [that] vanish under suspicious circumstances" (Ritter 2007). An unknown number of decedents are buried in clandestine graves nationwide at any given time. Thermal remote sensing techniques have been recognized as a standard approach to the location of clandestine graves for some time (France et al. 1992 and 1997). Currently, there is a limited amount of available published research on the thermal identification of clandestine graves. This lack of controlled studies, particularly image analyses, has left the method both somewhat time-consuming and ineffective because of the difficulty in distinguishing burial signatures from other anthropogenic, e.g., cisterns, old wells, buried refuse, etc., and natural artifacts, e.g., uprooted trees, acequias, etc. However, the inhibitive costs to law enforcement associated with

clandestine grave searches, such as time, manpower, and risk, could be substantially reduced if the techniques are refined.

This study used signatures from established controls (standardized, artificial graves) in an attempt to develop refined image analysis for more effective discrimination between clandestine graves and the surrounding environment. The research involved image manipulation and enhancement techniques to tease out more detail from surrounding noise. Additionally, classification algorithms were incorporated to determine the feasibility of identifying disturbances. Future research will focus on improving these techniques, as well as discrimination between clandestine burials and other manmade and natural artifacts. Such techniques should eventually reduce the time, costs, and manpower associated with the search for clandestine burials.

The project was made possible through a collaborative effort with the Texas Department of Public Safety Aircraft Section (DPS). A DPS helicopter, equipped with a 3-5μm L-3 Wescam 12DS200 imager, was used to capture digital thermal video over a series of control burials. The final approach should yield a more efficient search methodology supported by improved image analysis. These protocols will be made available to law enforcement agencies. The results of this and subsequent projects will be used to develop improved protocols for thermal discrimination of potential grave sites, which would substantially reduce law enforcement search times during ground-truthing.

Simulated graves (referenced as units) produced for this project did not include added animal remains. Instead, the project focused on the variables of depth and precipitation, and their effects on unit thermal signatures when controlling for soil type.

This information was used to simulate what an actual clandestine grave thermal signature under similar soil and environmental conditions should look like in the absence of active decomposition. Future research should include both control units and units with added remains for cross comparisons. Studies could then be expanded into different climatic and soil zones.

CHAPTER 2

RELEVANT LITERATURE

2.1 Remote Sensing Concepts

Remote sensing is the process of collecting information about features, e.g., differential reflectivity to assess vegetation cover or concentrated pollutants in bodies of water, or events of interest, e.g., tracking storm systems or wildfires, with detection equipment that is not in immediate contact with the area of interest. These techniques typically involve the use of specialized sensors that record electromagnetic radiation (EM) phenomena. All incoming EM is either reflected by the atmosphere or a surface, transmitted by the atmosphere, absorbed by the atmosphere or a surface, or radiated by the surface. Energy transmitted through the atmosphere may be reflected or absorbed by various earth surfaces. Those absorbed are converted for natural or potentially anthropogenic processes and later radiated outward. Further, energy that is radiated from a surface will also interact with the atmosphere, as described above. Remote sensors have been developed to detect EM in specific bandwidths, including ultraviolet, visible light, near infrared, middle infrared, thermal infrared, and microwave. Detection of these energies is only possible within atmospheric windows, the portions of the bands where EM is transmitted by the atmosphere and not readily absorbed (Jenson 2006).

Sensors may be passive or active types. Passive technology detects only EM that has been reflected (e.g., visible light, near IR) or radiated from a surface (e.g., thermal IR). Because these sensors are non-penetrating, they only record surface behaviors. However, qualitative assessments of what is observed on the “first surface”

may be indicative of a buried feature, such as an underground hot spring or a buried coal fire. Regarding active types, including active microwave and radar, the sensor acts as a source of EM. A beam is directed toward a surface of interest, and the sensor collects data reflected or backscattered back. Such sensor types can be also be used to directly study subsurface features in the right conditions because they have the ability to penetrate (Jenson 2006).

2.2 Thermal Remote Sensing

Thermal remote sensing, in this case the detection of the 3-14μm thermal infrared EM, was the technique selected for this project because the technology is readily available to law enforcement for standard policing activities. Thermal scanning is a passive approach that involves the detection of heat radiated from a surface. The thermal equipment mounted on airborne platforms used by various law enforcement agencies typically detects heat in the 3-5 μm (mid wave infrared/MWIR) and 8-14 μm (long wave/LWIR) atmospheric windows (Jenson 2006).

All objects with a temperature greater than absolute zero will radiate heat. Hotter objects, such as the sun (6000K), will display maximum exittance of shorter wavelength EM (in the case of the sun, visible light). The earth is relatively much cooler (300K) and radiates longer wavelength EM, such as radiowave and thermal. Thermal remote sensors do not detect and display the actual kinetic temperature of a surface, but instead detect radiant flux, or the photons emitted, from the surface. Some systems allow for the measurement of radiant flux to determine the radiant temperature, which

typically correlates with kinetic temperature. Differences between kinetic and radiant temperature are due primarily to emissivity (Scollar et al. 1990; Jenson 2006).

Emissivity is the ratio of EM radiated by a real world object of certain kinetic heat to that of a blackbody radiator of the same temperature. A blackbody can be described as a theoretical construct which absorbs all EM that strikes its surface, and emits all wavelengths of EM, with peak exittance defined by internal temperature. For example, the Sun approximates a 6000K blackbody. Emissivity values range between 0 and 1, with good emitters, which are typically good absorbers, e.g., water, closer to 1. Weaker radiators, such as metals, are typically bad absorbers because they readily reflect insolation. Regarding this project, distilled water has a high emissivity, while dry soil is relatively lower. An increase of soil moisture content subsequently raises emissivity for that soil. This concept is critical with respect to thermal remote sensing: objects with the same kinetic energy but different emissivity values should contrast. For example, a human (98.6°F) standing on a concrete pad the same temperature should still show up as “hot” on the scanner because the concrete is of a lower emissivity (Scollar et al. 1990; Jenson 2006).

2.3 Thermal Remote Sensing and Soil Disturbance

Numerous studies have demonstrated the potential application of thermal imaging in identifying disturbed soil. Johnson et al. (1997) described characteristic spectral differences between pristine and disturbed soils due to grain size. Land mines have been located thermally by both recognition of disturbed soil and by emitted heat from the mines in controlled studies (Winter et al. 1996). Irvine et al. (1997) further

demonstrated that the disturbed soils of known 1950s and 1960s era waste trenches associated with Oak Ridge National Laboratory were cooler than the surrounding soils due to increased moisture content. Thermal image temperature contrast was subsequently used to aid in the identification of previously undocumented trenches.

2.4 Applications in Archaeology

Thermal remote sensing has also been applied to archaeological prospecting. This method is typically employed for the purposes of the identification of surface and subsurface disturbances (Scollar et. al1990). Imagery collected by the NASA thermal multispectral scanner (TIMS) was used to identify prehistoric footpaths in highland Costa Rica (Sheets and Sever, 1991) and roadways in Chaco Canyon, New Mexico (Sever and Wagner 1991), that were not visible to the naked eye.

Similarly, thermal scanning has been used to identify buried, subsurface archaeological features. Ben-Dor et. al, (2001) used this method over an Early Bronze Age site in the Leviah Enclosure (Golan Heights), where numerous exposed basalt stones, the remnants of prehistoric construction material, had been observed. A helicopter-mounted thermal imager recorded nighttime video footage over the site. Extracted images were then rectified to a site map and used to discriminate additional stones, some contiguous with those exposed, that were buried in accumulated sediment. Thermal findings were later validated by excavation: stones were found to be between five and 50 centimeters below the surface. Although thermal remote sensing is passive and cannot penetrate a surface, the buried stones could be detected partially because they radiated heat at a slower rate than the surrounding matrix.

2.5 Applications in Forensic Anthropology

Rapid hydrolysis during the earlier stages of decomposition produces heat release from decomposing remains. “Casper’s dictum,” a rule of thumb proposed by 19th century pathologist Johann Casper that is still recognized today, states that what takes time “X” on the ground will be twice as long in the water and eight times as long in the ground (Casper’s Dictum…[2007]). Bass and Rodriguez (1985) noted these slower rates using six cadavers buried at various depths. Further, temperature probes associated with the burials revealed that during the exothermic portion of decomposition, the remains were relatively warmer than the surrounding grave soil, and temperatures measured from bodies that were buried at shallower levels were relatively hotter than those at greater depths. Similar to buried basalt stones, these heat signatures can be detected thermally.

Davenport (2001) presented an overview of various remote sensing techniques, both passive and active, and the application of those methods in clandestine grave searches. He noted that the primary goal in these exercises was to look for observed contrasts at the surface, or near-surface in the case of active sensors. Regarding thermal remote sensing, Davenport noted that graves could potentially be discriminated due to differential cooling patterns of the grave when compared to the background. Relevant factors affecting the contrast listed include grave moisture content, solar intensity (i.e., the load of solar energy on the surface), heat transfer, and likely, soil-type. Further, Davenport’s contention was that this method was best used when the interred corpse was in the earlier stages of exothermic decomposition (heat release).

France and colleagues (1992 and 1997) used truck-mounted thermal imagers to identify heat signatures on simulated graves containing pigs that were actively decomposing. They further noted that the disturbed soils in these simulated graves appeared thermally cooler than the surrounding undisturbed matrix following exothermic decomposition (France et. al 1997). Aircraft-mounted imagers used in an unpublished 1997 study in Belgium yielded similar results (unreferenced 2006 personal correspondence with J Stremersch).

2.6 Preliminary Research

The concepts described above were used in an April 2006 pilot study. A preliminary test was conducted in association with the Texas Department of Public Safety (TXDPS) using a site at the University of North Texas Discovery Park (UNTDP), where access could be controlled. Three adjacent units, each measuring 1 by 2 meters, were excavated to depths of 0.46 meters (1.5 feet; Unit 1), 0.91 meters (3 feet; Unit 2), and 1.52 meters (5 feet; Unit 3). They were then refilled without added biological material and subsequently scanned at night with an L-3 Wescam 12DS200 thermal imager mounted on a TXDPS helicopter. Additional scans were also obtained over a nearby historical International Order of Odd Fellows (IOOF) cemetery for comparison in Denton, Texas. The resulting video demonstrated a contrast between the disturbed and non-disturbed soils at both the prepared site and the cemetery (see Figures 1 and 2 below). Failure to fully discriminate was likely due to excessive rainfall over the previous four days.

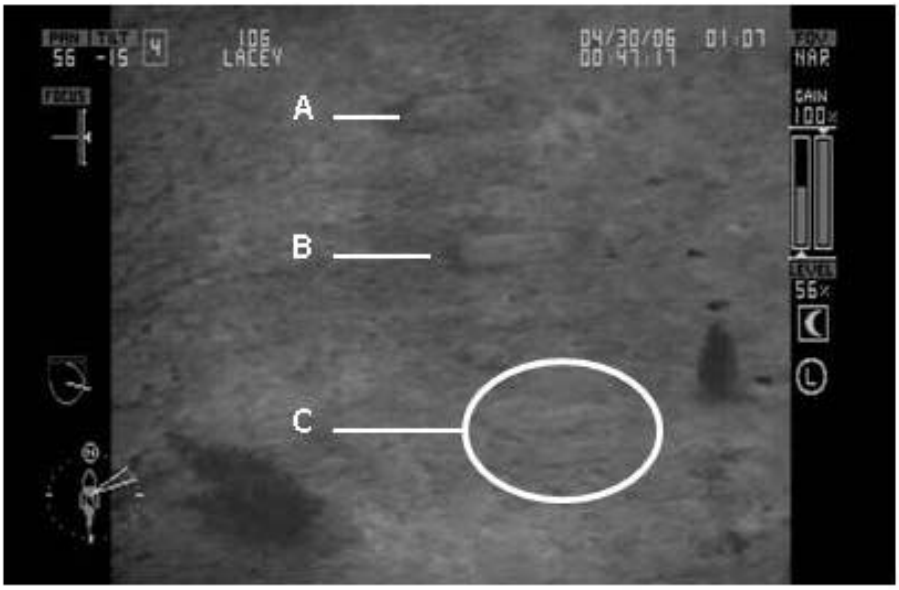

Figure 1. Thermal image of the preliminary test site at 500 feet, April 2006 flight. Darker features are warm. Scale is approximately 1:200. The outlines of units A (0.5 meters) and B (1.o meter) are readily observed. Unit C (1.5 meters) appears faint. Poor discrimination was likely due to excessive rainfall.

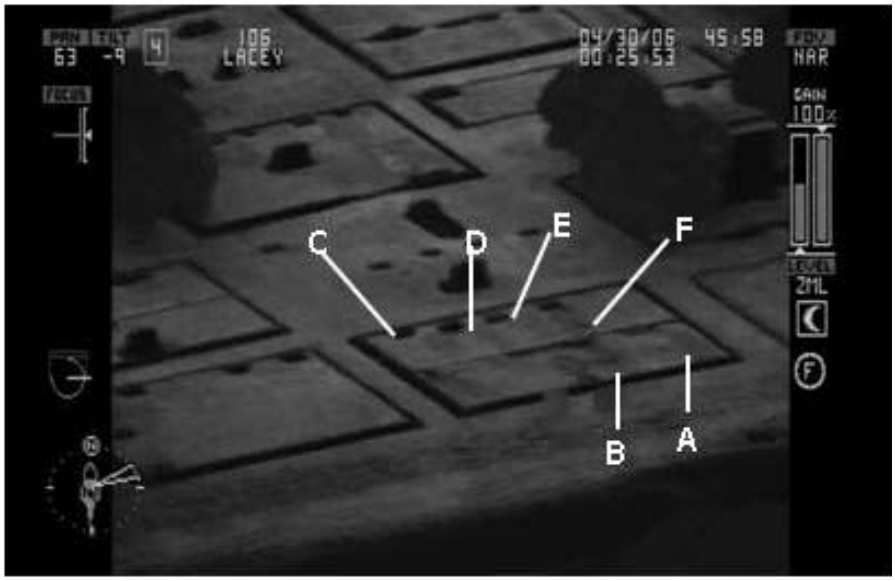

Figure 2. Thermal image of an historic cemetery in Denton, Texas at 600 feet, April 2006 flight. Darker features are warm. Scale is approximately 1:400. Graves were dated by ground-truthing the following morning.

A. 1988, 1940
B. 1983
C. 1943
D. 1968
E. 1977
F. 2001 (appears warmer)

Images captured over the UNTDP site were later analyzed at the UNT Center for Remote Sensing (CRS). The Erdas Imagine 9.1 software package was used to generate 17x37 pixel subset images of the three UNTDP units (see Figure 3). The software was further used to acquire the pixel brightness values (BV) that comprised each of those subsets. Subset BV distributions were then analyzed with custom-written programs for the SAS 9.1 (Statistical Analysis Software) programming language. BV distributions for each subset image were non-normal (Shapiro-Wilks normality test, all $P < 0.05$), highly significantly different (ANOVA on ranked data, $P < 0.0001$), and represented three statistically identifiable groups: Unit 1 > Unit 2 > Unit 3 (SNK multiple range test on ranked data, $\alpha = 0.05$). Thermal signatures became cooler, and were composed of a greater number of darker (lower BV) pixels, as depth increased.

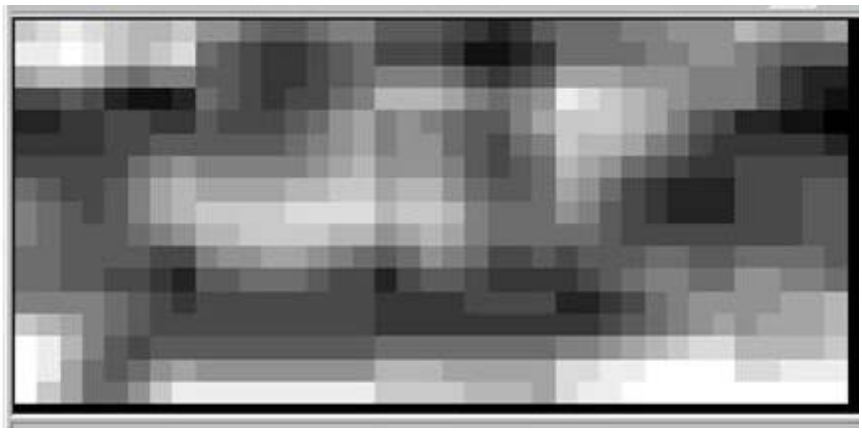

Figure 3. UNT Discovery Park, Unit C, April 2006 flight. 17x37 array of eight bit pixels, $n = 629$. The distribution of brightness values is highly significantly different from normal: Shapiro-Wilk, $W = 0.9537$, $P < 0.0001$. [30, 34, 36, 39, 46]

CHAPTER 3

MATERIALS AND METHODS

3.1 Area of Interest

The research site is located in Denton, Texas, at the University of North Texas Discovery Park (UNTDP) campus. The immediate area of interest (AOI), approximately 120 square meters, includes the three original simulated burials (units) that were placed in April 2006. The site is in an undeveloped and minimally-impacted portion on the of the UNTDP campus near the northwestern corner of the property line. The maximum elevation at the site is 220.68 meters along the north side (NCTCOG 2007). Elevation gradually decreases across the site, with a major drop-off into a drainage ditch along the southern site edge. Figures 5 and 6 below present the campus (wide field of view) and the immediate AOI, with associated contour intervals.

Denton is characterized as having a humid subtropical climate, meaning hot summers and relatively mild winters. The mean yearly ambient temperature is roughly 17.7°C, with yearly rainfall equaling approximately 96 centimeters. Precipitation is spread out across the year, with peak rainfall typically in May. Figure 4 below presents average monthly normal temperatures (high and low) and precipitation (Ford 1980; Denton Climatology…[2010]).

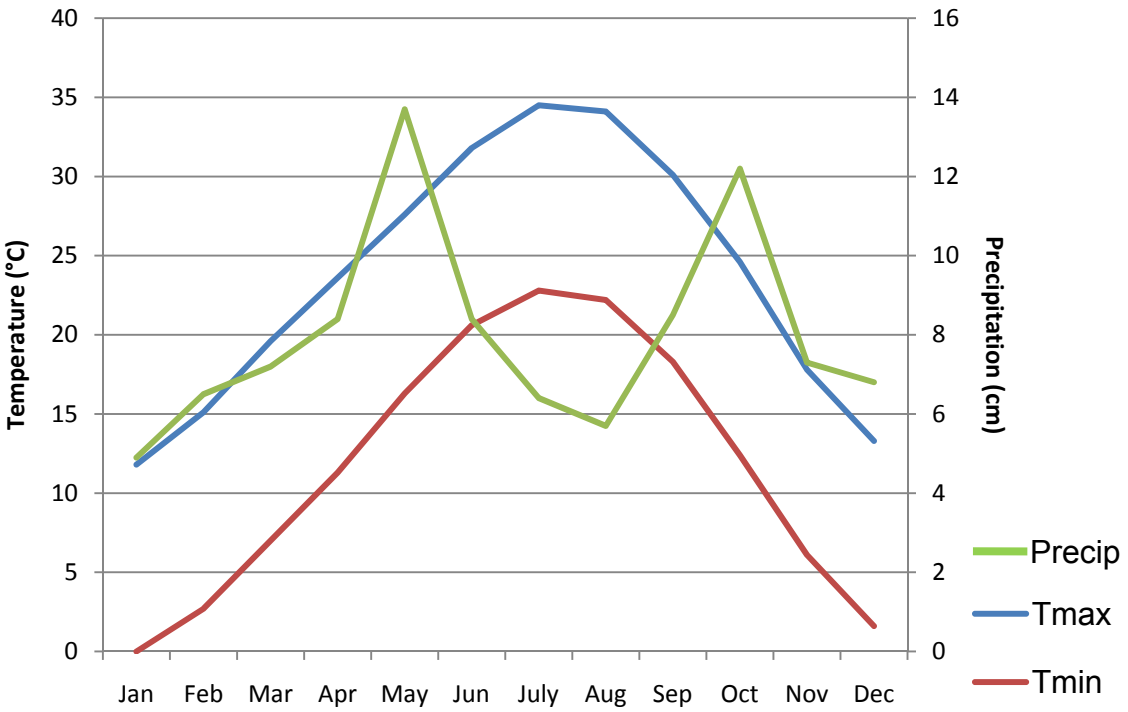

Figure 4. NOAA 30 Year Normals (1971-2000) for Denton, Texas. Maximum and minimum temperatures (left axis) by month are presented in degrees Celsius. Precipitation (right axis) by month is reported in centimeters.

Mean soil temperatures at depths greater than 50 centimeters for the Denton area are typically between 15°C and 22°C, with average summer and winter temperatures differing by greater than 6°C. Deeper levels in these soils maintain moisture for most of the year and dry out periodically only in the summer months. Local mean temperature for groundwater in shallower depths is approximately 19°C, or 1-2°C warmer than the mean ambient temperature, and fluctuates seasonally with the local climate (Heath 1983). The immediate AOI consists of Justin fine sandy loam soils, with slopes between one and three percent (Ford 1980). This soil series is characterized as well-drained, with moderately slow permeability. The upper soil layers are slightly acidic, becoming more alkaline at the lower levels. The five distinct layers in this series are described in Appendix A.

Denton is located in the Cross Timbers ecozone, which is recognized for expanses of prairie grasses interspersed with clusters of woodland. Vegetation in the AOI consists primarily of prairie grasses, including little bluestem, hairy gramas, and western ragweed. Multiple mesquite shrubs, as well as a medium-sized cedar tree (invasive) are within the AOI. A stand of post oaks is located in an undeveloped adjacent parcel to the west of the site (McMahan et al. 1984).

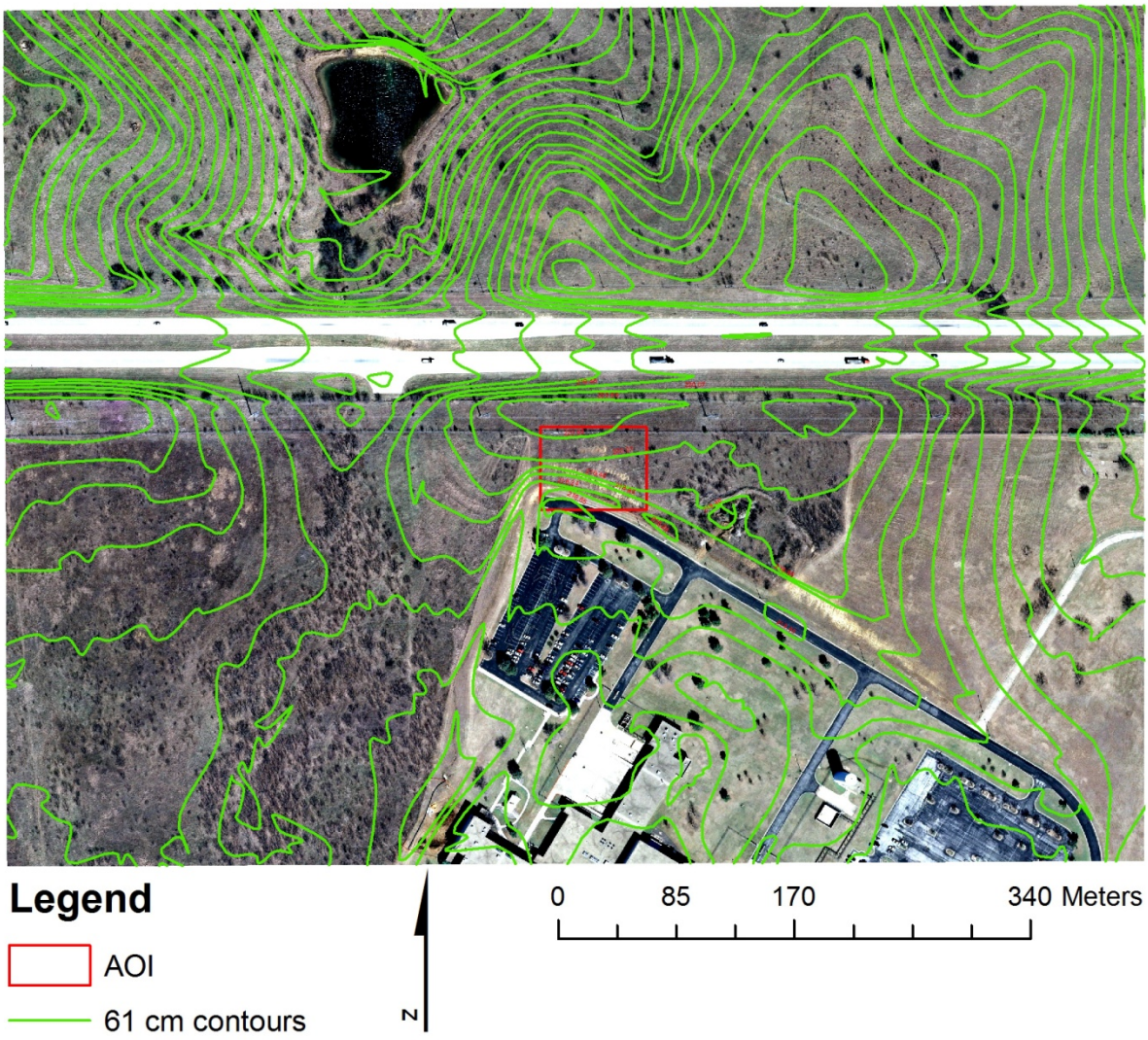

Figure 5. University of North Texas Discovery Park and study Area of Interest with contour lines (61 cm intervals, North Central Texas Council of Governments digital elevation model).

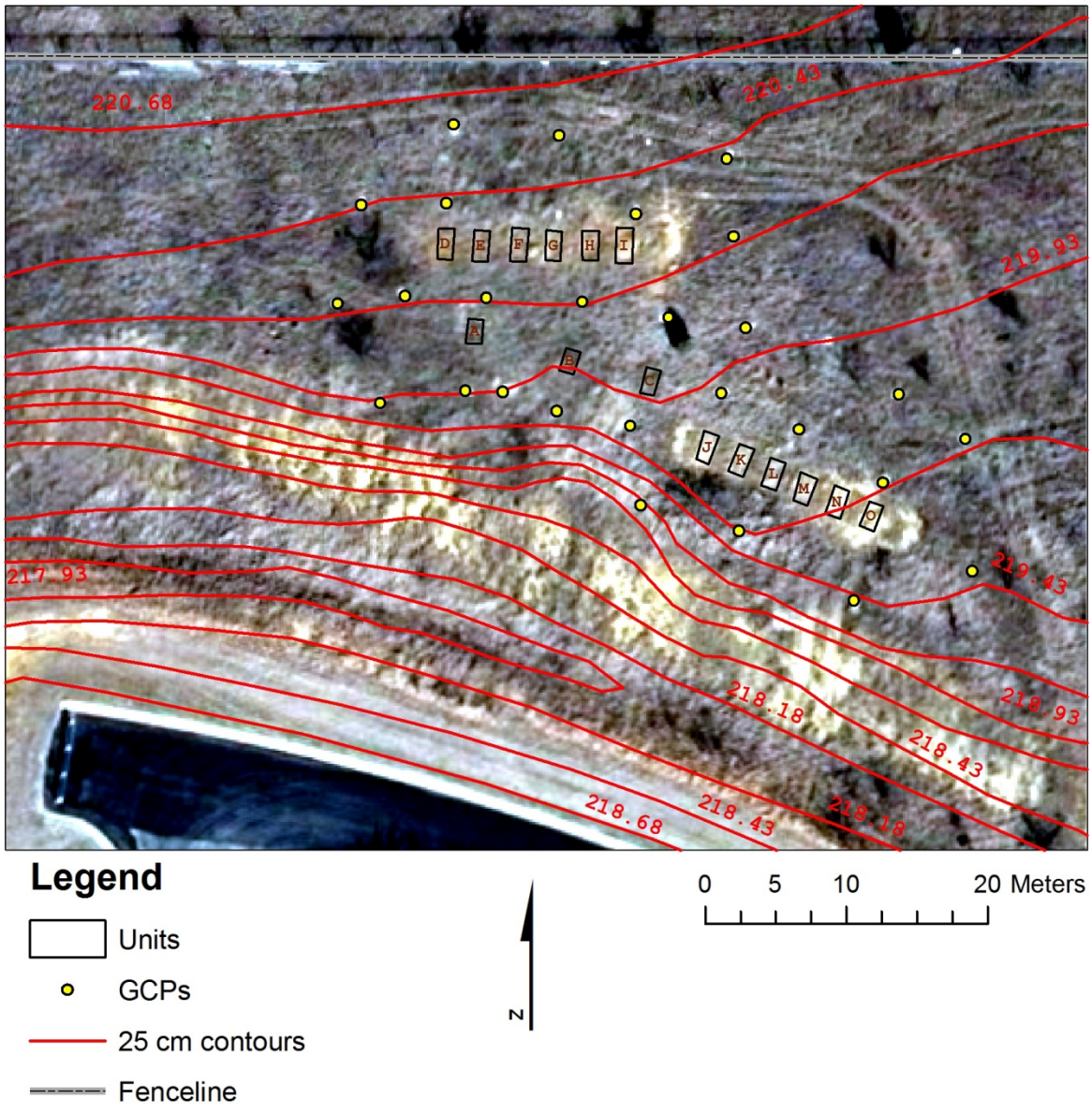

Figure 6. Research site on the in north-eastern aspect of the Discovery Park campus with disturbed units, stone ground control points (GCPs), and contour lines (25 cm intervals). Disturbed units include the preliminary set (units A-C), Set A (units D-I) and Set B (units J-O).

3.2 Research Site Set-up and Data Collection

The current research units were placed adjacent to the preliminary study. The site consisted of two locations, identified as Sets A and B. Each set consisted of six units measuring one by two meters. Units were excavated to the following depths: 0.25,

0.5 (two units), 1.0 (two units) and 1.5 meters, respectively. Site units were laid out prior to excavation using standard archaeological techniques (Saul et al. 2007):

1. Hammer in place a twelve inch galvanized nail (A)
2. Pull a two meter line from point 1 and place a second nail (B)
3. From A, pull a one meter line
4. From B, pull a second line (2.24 meters), representing the hypotenuse of a right triangle
5. Bring the lines from A and B together. Where they meet, place the third nail (C)
6. Repeat the process for the fourth point (D), drawing a one meter line from B and a 2.24 meter hypotenuse from A

The total number of experimental units (disturbed soil) was fifteen when including the original three from the preliminary study set. Ten additional control subsets (undisturbed areas) were later added to the map in ArcGIS (see below, Layer Preparation in ArcGIS).

Prior to excavation, local soil and vegetation data, as well as weather information for the preceding five years, were gathered. Initial groundbreaking was performed by backhoe on 23 May 2008. The units were then completed to proper dimensions with shovels and hand-tools on the following day. All excavated material was collected on tarps lying on ground adjacent to the units. Observed soil strata were identified with the Denton County Soil Manual (Ford 1980), and pertinent soil information, including soil type and permeability, were recorded. Soil profiles were then photographed with a Pentax *istDS SLR digital camera. Soil descriptions are presented in Appendix A. Soil and plant material removed from a specific unit were then backfilled with shovels. The site map, presented in Figure 6 overlay above, was generated on 28 June 2008 using a K&E Paragon Self-Indexing Alidade, Model 760000.

The entire research site, including Sets A, B, and the preliminary set, was scanned five times at altitudes between roughly 150 and 245 meters (500 to 800 feet)

above ground level with a helicopter-mounted L-3 Wescam Sonoma Model 12DS200. A sixth flight used a newer 3-5μm sensor that was being beta-tested by DPS (Model 12DS650). The 12DS200 consists of a three sensor payload encased in a lightweight, four-axis gyro-stabilized gimbal. Sensors include the following: a daylight color (RGB) camera with continuous zoom; a laser illuminator used by police to "paint targets", and; a 3-5μm staring focal plane array Indium antimonide (InSb) forward looking infrared (FLIR) sensor. The color camera and laser were not used for this study. The thermal sensor is operated at super-cooled temperatures. Imagery can be recorded through three fields of view (wide, middle and narrow); all output imagery is of 8-bit radiometric resolution. Permission to convey detailed sensor specifications, as well as Mean Resolvable Temperature Difference ("temperature resolution") and actual spatial resolution capabilities, could not be obtained from the manufacturer.

Flights were scheduled over the course of 18 months between August 2008 and February 2010 to account for a variety of environmental conditions. Scans were collected in the late evening to early morning hours, to ensure maximum contrast, and recorded live to an on-board flash drive. Both the scanner and the helicopter were operated by Texas Department of Public Safety personnel. Thermal scans were later converted to standard MPEG format upon return to the hangar and stored on a 2.0GB Cruzer Titanium Flashdrive. Weather data from the National Oceanic and Atmospheric Administration (NOAA) regional marking station, located approximately 4.5 miles from the project site at the Denton County Municipal Airport, were collected for the duration of the study and are presented in Appendices B-D (NCDC 2010). *In situ* research was conducted on sunny, clear days. Trips included documentation of invading vegetation,

as well as changes in unit physical appearance over time, such as superficial soil breakdown or possible soil compaction. All units were digitally photographed.

3.3 Data Collection

Thermal image analysis is typically qualitative (Jenson 2006). A scanner with the polarity set to "white equals hot" provides a grayscale thermal image composed of targets that are warmer (appearing light) or cooler (appearing dark) when compared with surrounding known targets in the image. Typical quantitative techniques, including the derivation of target temperature (kinetic) from radiant temperature, are extremely difficult and require highly sensitive equipment and specific knowledge of target properties, such as emissivity and moisture content (Jenson 2006). Image analysis for this project focused on the grayscale pixel variation of test units in aerial thermal images and subsequent image classification. It was hypothesized that units should appear thermally cooler (France et al. 1992 and 1997, Irvine et al. 1997), therefore the subset images should be composed of a greater number of darker (lower value) pixels.

3.3.1 Layer Preparation in ArcGIS

Prior to image analyses, preparations were made using the ESRI ArcGIS 9® software package. A file geodatabase was created in ArcCatalog® and populated with the site map, as well as the following created feature classes: ground control points (GCPs); unit corners; units, and; sample boxes (subsets). Additional files acquired from the North Central Texas Council of Governments (NCTCOG 2007 and 2009) were added, including a 2009 aerial image and the 2007 contour shapefile. The native

projection for the NCTCOG data was North American Datum 1983 (NAD83) Texas State Plane, North Central Texas, in feet. Both datasets were generated during NCTCOG winter surveys. The aerial photo was shot from 4800 feet (1463 meters) above ground level on a leaf-off, cloud free day, and was georeferenced by NCTCOG. The associated two-foot (61 centimeter) contour layer was generated from stereo-image: the images were collected at no greater than 5500 feet (1676 meters) altitude. Resulting contours were smoothed at NCTCOG. Both NCTCOG files were projected to NAD83 Universal Transverse Mercator Zone 14N North Central Texas, in meters (NAD83 UTM Zone 14N NCT, m). Projections for the site map and the above feature classes were defined in the same coordinate system.

The site map was rectified to the aerial image using the series of stone ground control points. Spatial coordinates were drawn from the stone locations on the map (center pixel of an “X”) as well as the spatial coordinates of the same stone in the aerial image. A first order transformation was selected (27 ground control points, total RMS_{error} = 0.29897) with nearest neighbor interpolation to establish the relationship between the map and the image.

Features were then added to the GCPs, unit corners, and unit classes created above. All new features were generated in ArcMap® Editor. The GCPs file consisted of 27 points corresponding to stones located on the map. The unit corner class consisted of 60 points (four points for each unit by 15 total units) that were used for a snapping environment for polygons created in the unit class. These polygons corresponded directly with the units on the site map. The ArcMap® Advanced Editing Tools option was then used to generate a rectangular “sample” area within each unit polygon. That

sample was copied and rotated to properly fit within the other 14 experimental units. An additional 10 sample subsets were placed in undisturbed areas throughout the site. Lastly, each subset was selected and exported as an individual feature class (25 total).

3.3.2 Image Selection

All analyzed images were originally sampled from MPEG data recorded during scheduled flights. Selected images included the following: raw images; enhanced images, and; filtered images. Raw images represented individual frames in the video (one frame out of 30 frames per second) using the Topaz Moment® media player, exported as JPEGs. Images selected from each flight video were primarily near and mid-range field of view (FOV). Collected images were converted to TIFF format (Windows Paint).

Enhanced images were also produced by Topaz Moment®. However, instead of being single frame stills, these are images that are interpolated by four consecutive frames, a technique referred to as super-resolution (unreferenced 2009 personal correspondence with A Yang). All enhanced images were generated from consecutive frames that included the captured raw image to ensure the same FOV and scale.

Super-resolution techniques were originally developed for data collected by sensors located on orbital platforms. Although the actual Topaz Labs® algorithms are unavailable for proprietary reasons, the general concepts behind super-resolution are well understood. Given a series of consecutive images, the data collected by the sensor are slightly different for each scan due to: 1) sensor error/mis-calibration; 2) data potentially lost during download, and; 3) additional possible errors introduced during

image processing. Each of these and other factors suggest that although resolution capabilities for a sensor (e.g., spatial, spectral, and radiometric) may be “X,” recorded data observed on an image will always be less than the maximum. Using a series of images, the data that are missing in one may be present in another. Thus, a series of images can be used to generate a new image that is of “higher resolution” than originals. Companies such as Topaz Labs® have applied these principals to generating enhanced images from consecutive video frames (Park et al. 2003; Farsiu 2004; unreferenced 2009 personal correspondence with A Yang).

Each pair of raw and enhanced images was duplicated. The duplicated images were then subjected to customized filters built with Topaz Simplify v.3®. Filter design focused on edge detection and area contrast in an effort to further “tease out” additional details and increase contrast between the disturbed units and the undisturbed surroundings.

Thermal data recorded during each flight included two available polarities (white equals hot, and an inverse black equals hot). Regardless of the polarity selected, the sensor gathers the same information, thus, established relationships between image features as observed by the user will reverse when the polarity is switched. This is demonstrated statistically in Appendix E.

A review of the collected flight data revealed that disturbed units were best visually discriminated when they appeared relatively dark against a light, undisturbed background, regardless of hot/cold considerations. Since polarity presentation is based on user preference, images selected for later analyses included only those in which units appeared relatively dark. It should be noted that a “dark” unit may be either

warmer or cooler than the background, depending on the flight. Units appeared relatively cool when compared to the background on only one of the six flights. Those same units appeared warm in four of the other flights, and faint to not present at all in one.

3.3.3 Image Preparation

Raw, enhanced and filtered images were loaded individually into ArcMap® and defined (NAD 83 UTM Zone 14N NCT m), along with the rectified site map, aerial photo, and pertinent feature classes. The site map was zoomed in to the corresponding extent of the FOV for the recorded image. Image transparency was adjusted to between 10 and 20% with the ArcGIS® Effects tool. The image was then set to fill the full extent of the viewer and permanently rectified to the site map using the ArcMap®Georeferencing tool. Links were drawn from thermal signatures of identifiable stones and/or the centers of individual unit signatures to corresponding points on the map. Overlaid feature classes, including the GCPs, units, and sample boxes, were used to properly identify link points on the map. Associated link tables were saved for all rectified images. All rectifications were first order (affine) polynomials with total $RMS_{error} \leq 0.5$. Cell values for all rectified images were calculated by cubic convolution interpolation. Output cell sizes were rounded to the nearest hundredth.

3.3.4 Band Selection

Although the sensor only gathers emitted radiation in one bandwidth (3-5μm), the output imagery is three-band, red-green-blue (RGB) composite grayscale. True

grayscale consists of equal parts of the three primary colors. Brightness value intensity in the study images is almost, but not quite identical. It should be understood that each band presents the same information. These slight shifts are for presentation only. When band levels are equal, the output is slightly brighter and has relatively lower contrast between lighter and darker image features. Figure 7 below displays an unrectified frame as captured from flight footage (a), and that same image converted (via Photoshop Elements 7®) to actual grayscale (b).

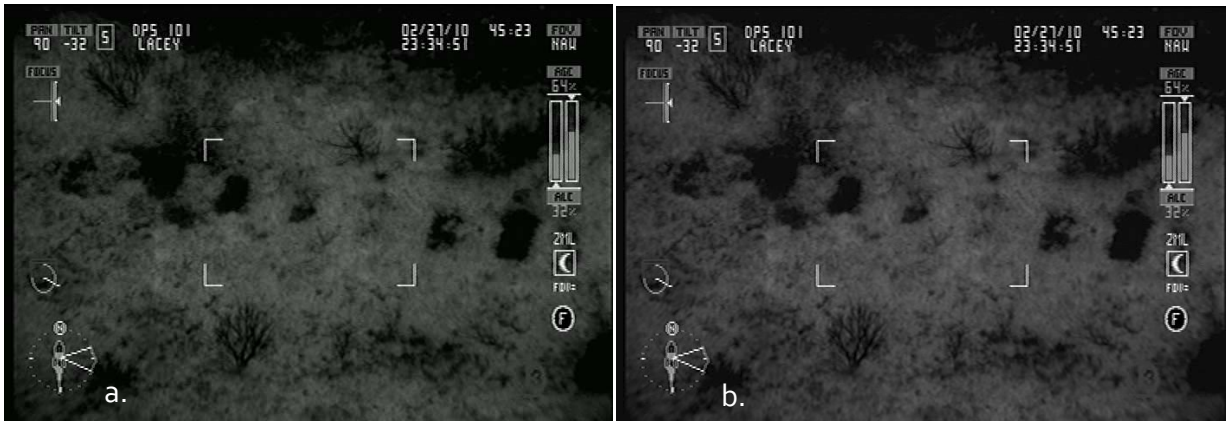

Figure 7. The three-band composite (a) and actual grayscale (b) versions of image 6r11 (unrectified). Contrast between image features is less pronounced in (b).

Prior to applying the sampling (extraction) scheme described below, a rectified image was taken from each flight and sampled repeatedly from each band. Although the bands were distinct from each other, relationships between samples were consistent across all three bands (see Appendix F). Because these three bands are providing redundant information, only one stretched band (Red: Band 1) was used for later sampling.

3.3.5 Subset Image Extractions and Pixel Data Acquisition

Samples from unit and control area signatures recorded in the FOV of a given rectified image were extracted. The individual sample class files generated above were used as feature masks. Extracted raster samples were then converted to ascii text files that consisted of the BVs making up the sample. Units that displayed poor alignment following rectification were omitted from extraction due to the possibility of interference from signature edge defects. Signatures or control areas partially or completely out of the FOV were not examined. Additionally, samples were not collected from any unit that was partially obscured by the viewer display icons (e.g., target, operator identification, etc.). The text files were then imported to an assigned Microsoft® Excel 2007 workbook. Following upload, additional attributes (variables) were added for each dataset, including a unit identifier (A-Y), depth, a set identifier, and the image type. The following model (Figure 8) was built in ArcGIS® Model Builder and used to perform extractions and ascii conversions:

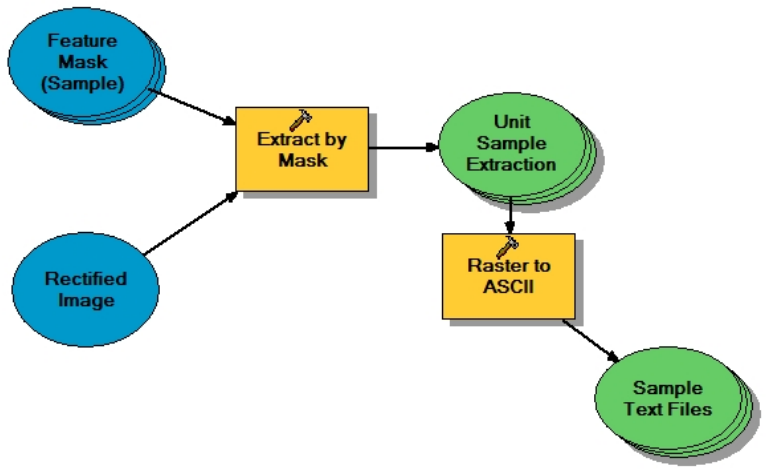

Figure 8. Unit Extraction and Conversion Model ArcMap® 9.0.

3.3.6 Statistical Analyses

Subset BV distribution variation was analyzed with SAS 9.2®. Procedures selected were parametric or nonparametric, dependent upon the outcome of normality testing on subset pixel distributions. Procedures included: 1) one-way ANOVA or Kruskall-Wallis, as necessary; 2) Student-Newman-Keuls (SNK) multiple range test (non-ranked or ranked), and; 3) Pearson's or Spearman's correlation. Conditions tested were: 1) differences between disturbed unit signatures and non-disturbed controls; 2) differences within a Set based on depth of disturbance, and; 3) associations between thermal signature and depth. All procedures described above in section 3.3 are presented diagrammatically in Appendix G.

3.4 Classification Study

Image classification in remote sensing is the process of assigning the BVs of features recorded in an image to proper, identifiable classes. The output classified image serves as a thematic map consisting of various land covers and land uses, such as prairie grass, forest, pond, roadway, etc. Lu and Wang (2007) identify multiple issues that can ultimately affect the accuracy of a classification, including: 1) complexity of the landscape (e.g., heterogenous, homogenous, rugged, etc.); 2) the data sources (resolutions, climatic conditions when collected, etc.); 3) processing methods used for the data, and; 4) the actual algorithms selected for classification.

Traditional classification techniques, or "hard classifiers," are done on a pixel-by-pixel basis. The two basic methods are "unsupervised" and "supervised". Although there are multiple algorithms that can be used for either selection, each process can be

readily generalized. Unsupervised classification involves a two step approach, in which the user defines the number of clusters (e.g., 25, 50, 100, etc.) to which pixels in an image should be assigned. The process then populates each cluster with pixels based on spectral characteristics (brightness value, or BV). The user then merges multiple clusters of pixels into a single known class. For example, three clusters recognized to represent water would be combined as one. Conversely, supervised classification requires the user to identify known examples from each class in the image (e.g., grassland, forest, etc.). The analyst selects areas from each land cover or land use area to serve as training sites for class signatures. The classification software then places all remaining “unknown” pixels into various classes based on the pixel BV.

Object oriented classifications are relatively newer techniques that have become more prevalent as the availability of higher spatial resolution imagery has increased. These techniques in some ways can be viewed as a combination of unsupervised and supervised classification. The method consists of two primary steps. First, the image is segmented, a process that splits the image into contiguous objects. Each object is composed of a group of pixels which are closely related, both spectrally and spatially. This differs from the traditional classifiers in that those classification types are based solely on spectral characteristics (BVs only) and do not account for geographical relationships.

The initial segmentation, somewhat analogous to the unsupervised process, is followed by user defined manipulation and rule building. Closely related objects are merged together a larger individual objects. For example, a segmented image of a cement-constructed helicopter landing pad may consist initially of 15 objects: these

objects can then be joined together as a single object by the user. Various algorithms can also be used to separate objects into different classes based on shared attribute characteristics or dissimilarities (e.g., mean object brightness, area, circular/ellipsoid/rectangular shape, length/width, linearity, etc.). User-defined attribute threshold levels are used to classify objects. An example of this would be classifying all objects with a mean brightness greater than 110 and area greater than 300 pixels as "control. "

While the traditional methods have been used more extensively in remote sensing, the object oriented models are fast becoming acceptable and sometimes preferred alternatives. Whiteside (2005) compared the results of both a per-pixel (supervised) and object oriented classifications in a land use study using multispectral images collected by the Advanced Spaceborne and Thermal Emission and Reflection Radiometer (ASTER) over an area of interest (AOI) in the Australian Northern Territory. The latter method reportedly generated higher accuracy output images. Similar findings were reported in a coal fire mapping study, conducted in Mongolia, China that also compared resulting classified ASTER images (Yan et. al, 2006). Willhauck (2000) used both methods in a change detection study (deforestation in Tierra del Fuego Province, Argentina) using older digitized aerial photos and newer Satellite Pour l'Observation de la Terra (SPOT) images. The author reported that although accuracy levels were comparable, the hierarchial tree developed for the object oriented could be reapplied for future images for change detection and potentially save a lot of time. All authors reported speckled appearance, or a "salt and pepper" effect, observed on traditionally classified images.

Traditional and object-oriented techniques were used to classify a selection of rectified images generated above. Images were selected from three flights, and included both near and middle FOV. Duplicated units in Sets A and B (two each of 0.5 and 1.0 m units) were used to test the Erdas Imagine® supervised classification function. Treating one pair of units in a location as “graves of known depth,” training sites were selected from those units to see if the other “unknown” pair could be properly classified, as well as other represented classes, such as vegetation/control, trees, ditch, etc. Conversely, process trees constructed in Trimble eCognition Developer 8® were developed to separate units based on depth (classes for 0.25, 0.5, 1.0, and 1.5m disturbances) from all other represented class identifications.

Image classifications were performed for multiple reasons. Initially, this was done to test the robusticity of both methods to see how well disturbed unit signatures were discriminated from undisturbed backgrounds that exhibited similar spectral characteristics. Successful thermal image classifications represent a potential tool for future law enforcement reconnaissance, especially as real-time classification programs become available. Additionally, the results could help determine the feasibility of using classification techniques to discriminate between undisturbed areas and potential burials, as well as other anthropogenic and natural soil disturbances.

Prior to conducting any classifications, all images were converted in ArcMap® to Imagine (.img) format. Converted images were then cropped with the Erdas Imagine® Subset function to remove as much of the peripheral readout as possible. No features of major interest, e.g., disturbed units, were included in the cropped area.

3.4.1 Supervised Classification

Classes attempted with this method included: 1) current units by depth, in meters; 2) preliminary units as a group; 3) control (undisturbed area); 4) trees; 5) ditch, and; 6) readout. For reasons of presence or absence within a given image, it should be noted that not all classes were applicable in each classification. The recommended number of sample pixels per class was determined as follows:

$$n = k + 1,$$

where n represents the number of pixels, and k is the number of available bands in the image (Jenson 2006). Due to redundancy, there was essentially only one band (n = 2); therefore, the total recommended number of pixels should be at least "10n," or at least 20 pixels per class.

Training sites were selected using the Erdas Imagine® seed option. The defined maximum seed size was dependent on the type of image: "raw-based" image seed size was 10 pixels, and up to 50 pixels were used for "enhanced-based" images. The seed Euclidian distance was set to 5, which excluded pixels with BVs that were five units greater or less than the seed pixel. All classes started out with a minimum of 10 training sites, although many of the training signatures were later deleted or merged with other classes based on excessive signature overlap. The minimum distance algorithm was selected for all subsequent supervised classifications.

3.4.2 Object-Oriented Classifications

The same subset images generated above were classified with Trimble eCognition Developer 8®. Process trees (rule sets) were developed for each

classification. The initial step (parent process) in each case applied the multiresolution segmentation algorithm, which broke each image into contiguous segments. When necessary (image dependent), multiple objects that comprised one feature, such as a disturbed unit or a tree, were manually merged together.

All subsequent rule set steps (child processes) assigned objects to classes based on object features. These features consisted primarily of actual value (mean object brightness and maximum-minimum difference in brightness), geometry (object area, and shape characteristics: e.g., roundness, compactness, rectangularity, asymmetry, etc.), and relative position (object distance of *X* or *Y* units from a given image border). Rule set design consisted of earlier child processes that identified individual classes that were not disturbed units, including ditch, trees, and control areas. Once non-disturbances were classified, the last set of child processes assigned units to specific classes, including the current study units by depth, and preliminary units collectively.

3.4.3 Accuracy Assessment

The accuracy of classifications produced from both methods was assessed by using error matrices. A stratified random sample of 64 pixels was generated in Erdas Imagine® for each supervised classification. Pixels were identified and labeled based on the class that the individual pixels should belong to. Due to the small size of the immediate AOI, the assigned classes for reference data and the above samples were the same in each supervised classification assessment. Error matrices conducted in eCognition® were based on training and test area (TTA) masks constructed from each

segmented image. Similar to the process described above, objects, each consisting of multiple pixels, were sampled for each class based on a known “real world” identity. Error matrices for both methods calculated accuracy levels by comparing the labeled identification of pixels or objects against how they were eventually classified. All classification procedures described in section 3.4 are available diagrammatically in Appendix G.

CHAPTER 4

RESULTS

A total of seven flights were conducted. These included six flights for the current study and well as the preliminary run from April 2008. All but the final flight (Number 6) used the L-3 Wescam 12DS200 imager. The sensor used on flight six was a new sensor being field-tested for the manufacturer. General flight information is presented in Table 1 below.

Table 1. Pertinent flight data for the seven scheduled surveys. With the exception of the Preliminary Set, units were not observed in the Flight 2 survey (*). Thermal discrimination for the preliminary flight was relatively poor.

Flight	Date	Conditions	On site	Altitude (ft)	Temp(°C)	Unit
P	4/29/06	warm, wet	4/30/2006, 0045hrs	500	13.9	cool, poor
1	8/28/08	hot, wet	8/28/2008, 0135hrs	650	26.1	warm
2	11/21/08	cold, damp	11/22/2008, 0005hrs	650	5	not observed*
3*	9/1/09	hot, dry	9/2/2009, 0000hrs	650	22.5	warm
4	9/2/09	hot, dry	9/3/2009, 0000hrs	800	23.9	warm
5	10/20/09	warm, wet	10/21/2009, 0005hrs	700	20.6	cool
6	2/27/10	cold, dry	2/27/2010, 2325hrs	650	3.3	warm

4.1 Statistical Analyses Results

All images selected for analysis were rectified to the site map. Image rectifications were conducted using an affine polynomial, with the associated root mean square error (RMSerror) value less than 0.5. Brightness values for the new raster grids were calculated by cubic convolution interpolation. A table for each rectified image,

including the RMSerror, number of links, and the samples extracted is presented in Appendix H.

Analyzed images (32 total) were arranged in eight series. Each series consisted of four rectified images, including the following: raw (r), enhanced (e), filtered-raw (rf), and filtered-enhanced (ef). The selected image nomenclature reflects the flight number, image number, and type of image. For example, the four images belonging to series 1_23 are from flight one, image number 23, and are identified 1r23, 1e23, 1r23f, and 1e23f).

No images were analyzed for the preliminary, second and third flights. The preliminary site set-up pre-dated placement of stone ground control points (GCPs). The lack of GCPs and other known features from newer units in Sets A and B left a shortage of link sites to the map. All attempts at rectifying preliminary flight images produced badly warped outputs. Similarly, flight two images yielded poor to no discrimination of units. The preliminary set exhibited slightly warm signatures, however, the remaining newer units were not readily observed. Data from the third flight failed to record due to equipment malfunction, although the in flight sensor readout on the monitor looked no different from those recorded during flight four conducted on the following evening.

Statistical results for series 1_23, 6_11, 4_25, and 5_26 are presented below. Except for series 5_26, these image sets were selected for presentation due to the best visual contrast in the raw image. Additionally, the representative series include both middle-to-wide (whole site) and narrow (individual Sets A and B) FOV's. Series 5_26 displays some distortion due to sensor miscalibration. However, it was included because flight five was the only survey during which the units appeared relatively cool.

Rectified frames and associated statistical results for the four remaining image series (1_22, 4_22, 5_2, and 6_10) are available in Appendices I and J, respectively. Samples consisting of units and controls were extracted from each image and analyzed with SAS 9.2®.

4.1.1 Image Series 1_23

Series 1_23 consists of narrow FOV shots of units D through I (Set A), as well as preliminary units A and B. The four images in this series are displayed in Figure 9, a-d, below. The cell size for 1r23 and 1r23f is 0.05meters; the corresponding value for 1e23 and 1e23f is 0.02 meters. Four units (E-H) and two controls were sampled from each image. Image 1r23 also included units D and I. Units A and B were not sampled. The majority of samples collected were not distributed normally: there were three exceptions from image 1r23f. Results of Shapiro-Wilks (image samples from 1r23 and 1r23f) and Kolmogorov-Smirnov (images 1e23 and 1e23f, sample sizes greater than 2000 pixels) normality testing are presented in Table 2, a-d. Box plots of the five number summaries may be viewed in Figure 10, a-d.

Samples from each group were highly significantly different from each other (Kruskall-Wallis, i.e., one way analysis of variance on ranked data), and in each case, separated into statistically distinct groups (SNK on ranked data, α=0.05). Further, there is a significant negative association between depth of disturbance and pixel brightness value (Spearman's ranked correlation). The results for all three tests are available in Table 3.

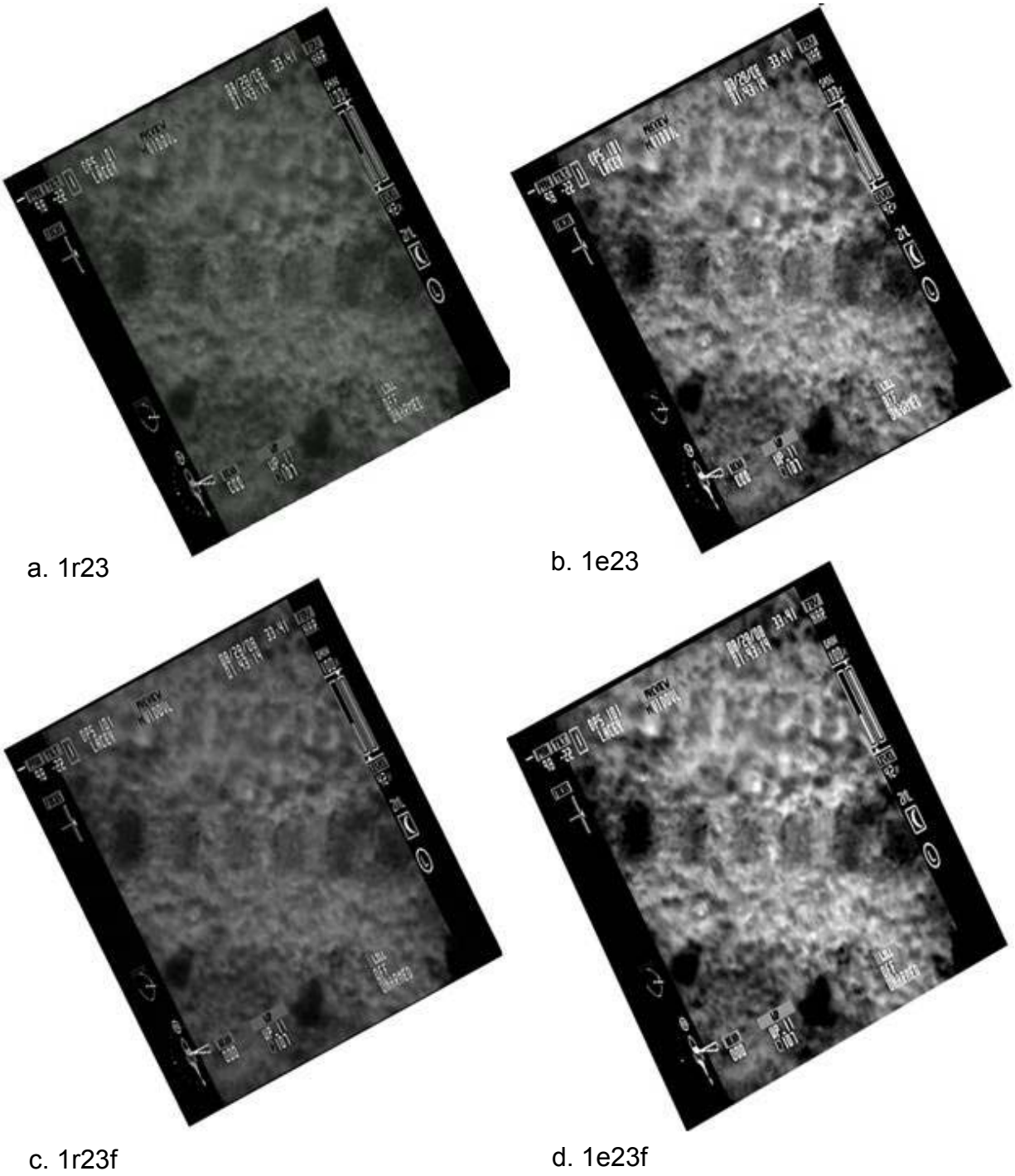

a. 1r23

b. 1e23

c. 1r23f

d. 1e23f

Figure 9, a-d. Rectified images comprising series 1_23. Image 1r23 (a.) is the rectified version of the original frame capture. Image 1e23 (b.) is rectified from the original enhanced image. 1r23f (c.) and 1e23f (d.) were generated from filtering the original, unrectified images. Viewed left to right in the middle of each image are Set A units (D through I). Two additional units from the Preliminary Set are present in the bottom of the image (units A and B).

Table 2. Sample size and normality results for BV sample distributions extracted from image series 1_23. Shapiro-Wilk *W* normality (S-W *W*) and probability are reported in (a) and (b). Kolmogorov-Smirnov *D* normality (K-S *D*) and probability are presented for (c) and (d). "*" denotes normal distributions in (b). Control units are reported as (Con).

a. Image 1r23

Unit ID	*n*	S-W *W*	*P*
D	490	0.8521	< 0.0001
E	491	0.9915	= 0.0064
F	492	0.9908	= 0.0037
G	489	0.9886	= 0.0007
H	493	0.9804	< 0.0001
I	492	0.99	= 0.0019
(P)	492	0.9766	< 0.0001
(S)	492	0.9249	< 0.0001

b. Image 1e23

Unit ID	*n*	K-S *D*	*P*
E	3073	0.0491	< 0.01
F	3073	0.0637	< 0.01
G	3074	0.0908	< 0.01
H	3075	0.0573	< 0.01
(P)	3073	0.0703	< 0.01
(S)	3073	0.131	< 0.01

c. Image 1r23f

Unit ID	*n*	S-W *W*	*P*
E	491	0.9965	= 0.3674*
F	492	0.9965	= 0.3571*
G	489	0.9957	= 0.2017*
H	493	0.9926	= 0.0151
(P)	492	0.9671	< 0.0001
(S)	492	0.9383	< 0.0001

d. Image 1e23f

Unit ID	*n*	K-S *D*	*P*
E	3073	0.0628	< 0.01
F	3073	0.0563	< 0.01
G	3074	0.1012	< 0.01
H	3075	0.0622	< 0.01
(P)	3073	0.0876	< 0.01
(S)	3073	0.1394	< 0.01

a. 1r23

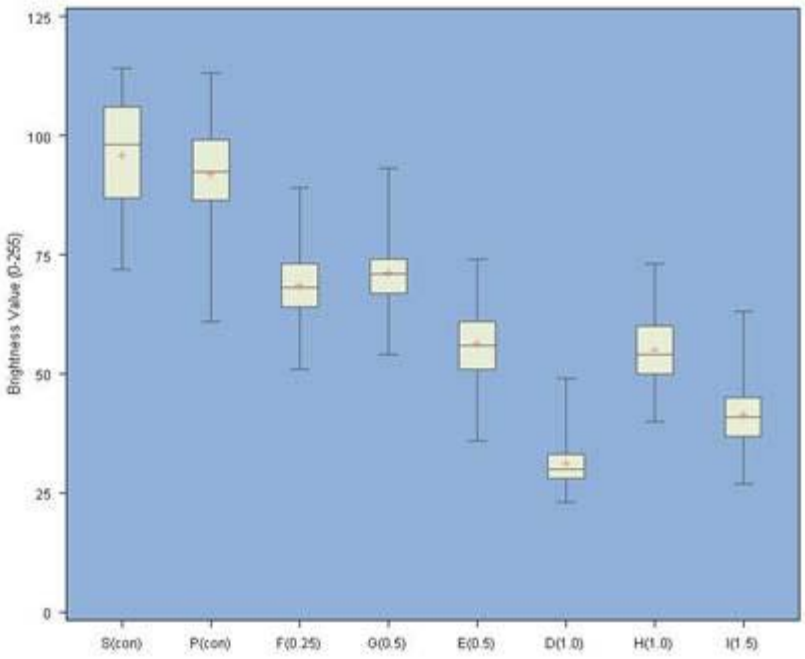

b. 1r23f

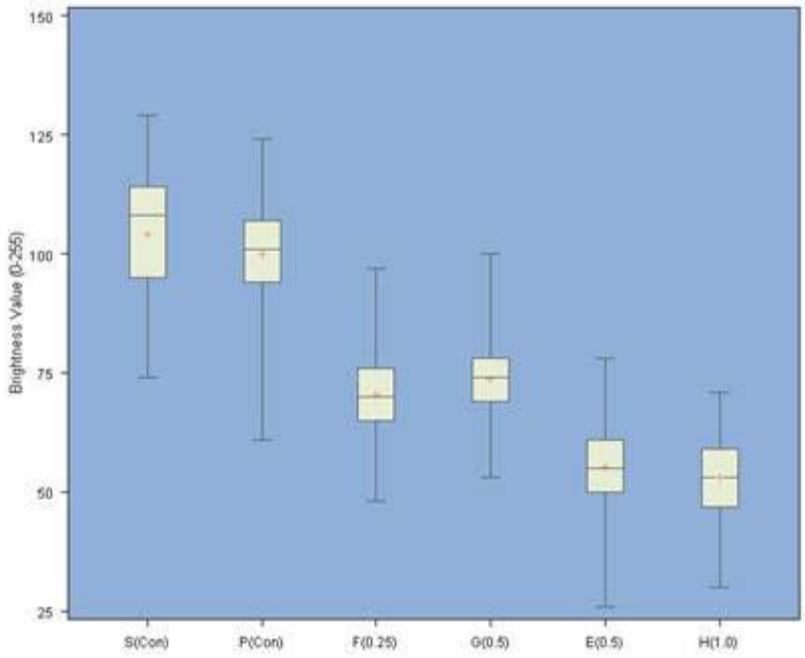

c. 1e23

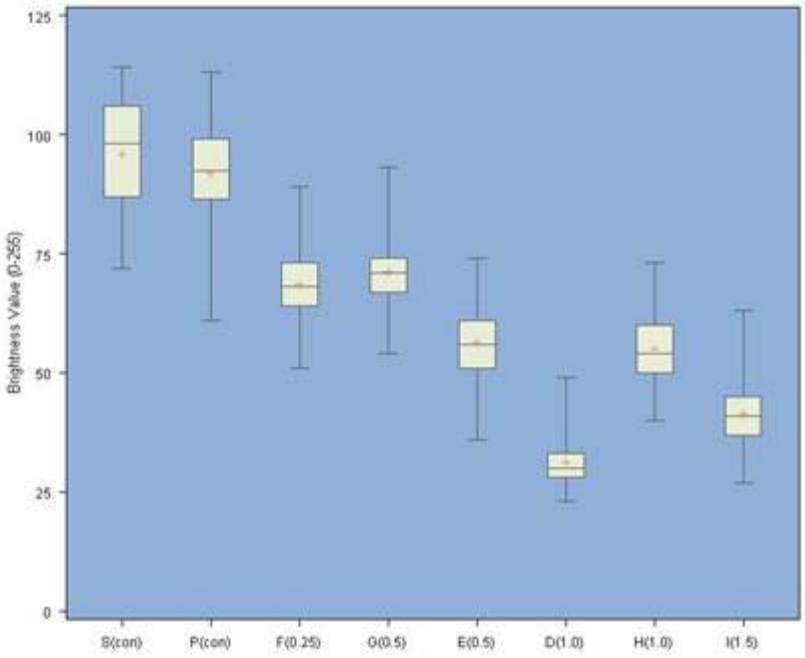

d. 1e23f

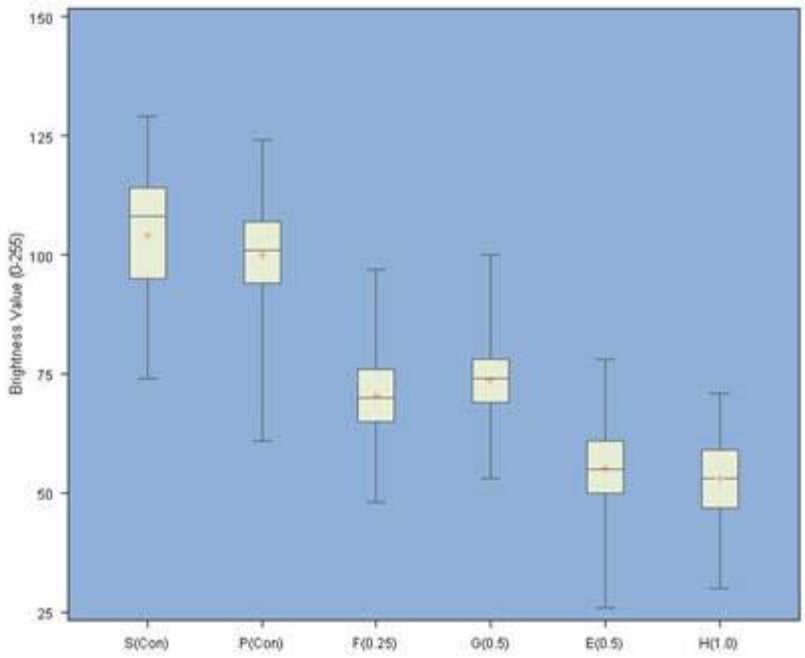

Figure 10, a-d. Box plots of five number summaries for extracted samples. Plots are arranged left to right by increasing depth of disturbance, from control (no disturbance) to 1.5 meters. Depths are presented in "()" next to the unit identifier.

Table 3. Results of Kruskall-Wallis analysis of variance on ranked data, Student-Neumann-Keuls on ranked data, and Spearman's correlation analysis for image series 1_23. Samples from each image are highly significantly different and each sample is statistically distinct. Depths are reported as (meters). (Con) denotes no disturbance (depth = 0m). Significant negative correlation between depth of disturbance and brightness value is noted.

Image	K-W *H*	DF	*P*	SNK Grouping	r_s	*P*
1r23	3524.55	7	< 0.0001	S(con) > P(con) >G(0.5) > F(0.25) > E(0.5) > H(1.0) > I(1.5) > D(1.0)	-0.8693	< 0.0001
1r23f	2505.87	5	< 0.0001	S(con) > P(con) > G(0.5) > F(0.25) > E(0.5) > H(1.0)	-0.8402	< 0.0001
1e23	15307.6	5	< 0.0001	S(con) > P(con) > G(0.5) > F(0.25) > E(0.5) > H(1.0)	-0.8329	< 0.0001
1e23f	15603	5	< 0.0001	S(con) > P(con) > G(0.5) > F(0.25) > E(0.5) > H(1.0)	-0.846	< 0.0001

4.1.2 Image Series 6_11

Series 6_11 was comprised of narrow FOV images over Set B (units J – O). Cell sizes were 0.04 (images 6r11 and 6r11f) and 0.02 (6e11 and 6e11f) meters, respectively. Image 6r11 is presented in Figure 11. The remaining three images are available in Appendix I. Each of the four images provided sample extractions for all six units and at least control. An additional control was sampled for images 6r11 and 6r11f. There were no normally distributed samples (Shapiro-Wilks normality test). Normality results for image 6r11 are presented in Table 4. Box plots displaying five number summaries for the eight 6r11 samples are presented in Figure 12. Summaries for the remaining three images are available in Appendix J.

The samples extracted from each image were highly significantly different (Kruskall Wallis one way analysis of variance on ranked data) and separated into identifiable groups for each of the four images (SNK multiple range test on ranked data). Similar to that observed in series 1_23, there was a highly significant negative correlation between depth of disturbance and pixel value (Spearman's ranked correlation). Analyses results for 6_11 images are presented in Table 5.

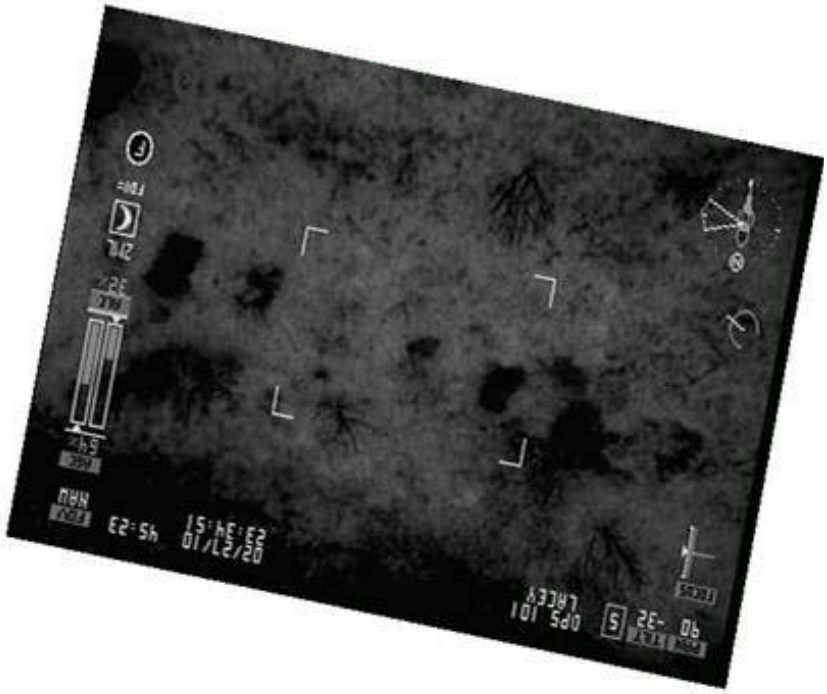

Figure 11. Image 6r11, consisting of Set B units, left to right (J through O). The signature for unit L (0.25 meter unit) is faint.

Table 4. Sample size and normality results for BV sample distributions extracted from image 6r11. Shapiro-Wilk *W* normality (S-W *W*) and probability are reported. Control units are reported as (Con).

Unit ID	*n*	S-W *W*	*P*
J	769	0.358	< 0.0001
K	769	0.9096	< 0.0001
L	768	0.9938	< 0.0001
M	770	0.9693	< 0.0001
N	769	0.7427	< 0.0001
O	768	0.4926	< 0.0001
(T)	769	0.9597	< 0.0001
(U)	769	0.9356	< 0.0001

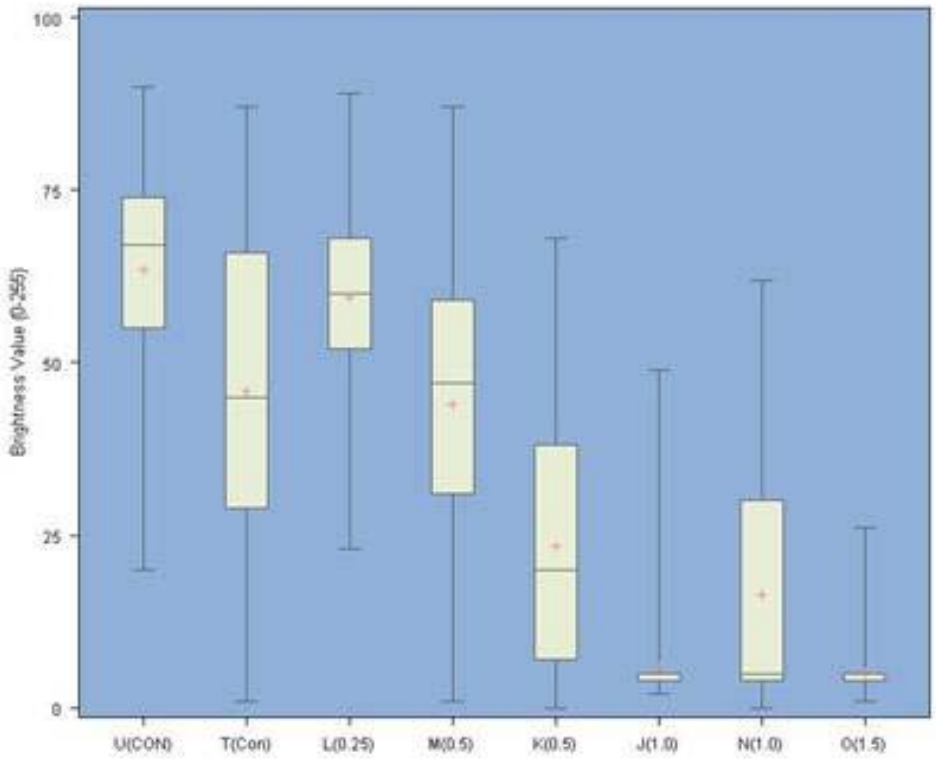

Figure 12. Box plots of five number summaries for the eight samples extracted from image 6r11. Plots are arranged left to right by increasing depth of disturbance, from control (no disturbance) to 1.5 meters. Depths are presented in "()" next to the unit identifier.

Table 5. Results of Kruskall-Wallis analysis of variance on ranked data, Student-Neumann-Keuls on ranked data, and Spearman's correlation analysis on image series 6_11. Samples from each image are highly significantly different and each sample is statistically distinct. Depths are reported as (meters). (Con) denotes no disturbance (depth = 0m). Highly significant negative correlation between depth of disturbance and brightness value is noted.

Image	K-W *H*	DF	*P*	SNK Grouping	r_s	*P*
6r11	4194.77	7	< 0.0001	U(con) > L(0.25) > T(con) > M(0.5) > K(0.5) > N(1.0) > J(1.0) > O(1.5)	-0.7558	< 0.0001
6r11f	3933.43	7	< 0.0001	L(0.25) = U(con) > M(0.5) = T(con) > K(0.5) > N(1.0) > O(1.5) > J(1.0)	-0.6258	< 0.0001
6e11	16288.8	6	< 0.0001	U(con) > L(0.25) > M(0.5) > K(0.5 > N(1.0) > O(1.5) > J(1.0)	-0.8222	< 0.0001
6e11f	16261.7	6	< 0.0001	T(con) > L(0.25) > M(0.5) > K(0.5 > N(1.0) > O(1.5) > J(1.0)	-0.8207	< 0.0001

4.1.3 Image Series 4_25

Series 4_25 consists of a wide FOV over the entire site. Please see Figure 13, image 4r25, below). The remaining three rectified images are presented in Appendix I. Images 4r25 and 4r25f cell sizes are 0.10 meters; the cell size for the other two images is 0.05 meters. Each image was sampled 13 times (six units, seven controls), with the exception of image 4e25 (six units, six controls). An additional four units were sampled from image 4r25f. Shared unit extractions included three from Set A (units E, F, and G), three from Set B (J, K and L).

All samples, except two from both 4r25 and 4r25f, consisted of non-normal distributions (Shapiro-Wilk's test). Normality results for image 4r25 are presented in

Table 6. Box plots for sample descriptive statistics are presented in Figure 14. Normality results and five number summaries for samples belonging to images 4r25f, 4e25, and 4e25f are in Appendix J. Samples again were highly significantly different (Kruskall-Wallis analysis of variance on ranked data) and separated into statistically distinct groups (SNK on ranked data). The previously observed significant negative relationship between depth of disturbance and unit signature occurred (Spearman's ranked correlation). Series 4_25 statistics are presented in Table 7.

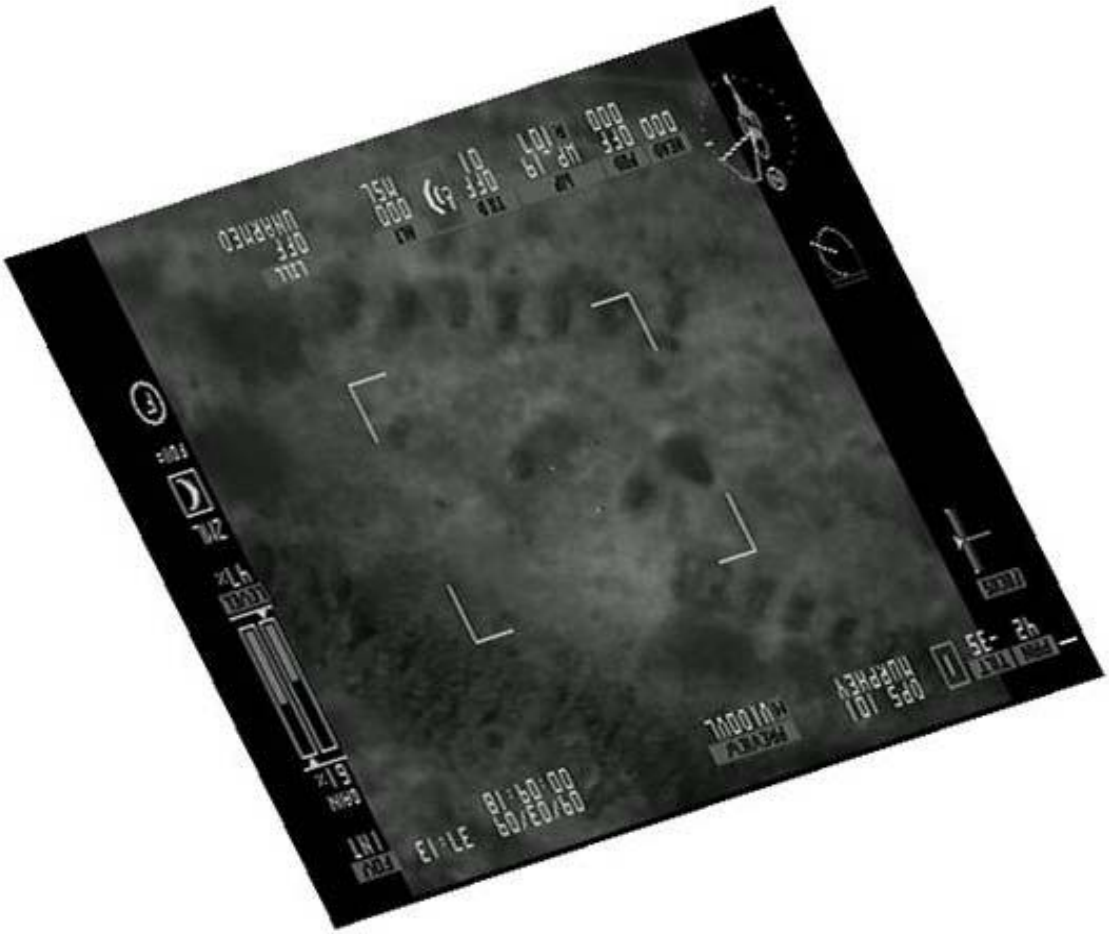

Figure 13. Image 4r25, a wide FOV image over the entire site. Set A units are toward the top of the image, with Set B units located toward the lower right corner. The Preliminary Set is visible in the center, within the target area of the monitor.

Table 6. Sample size and normality results for BV sample distributions extracted from image 6r11. Shapiro-Wilk *W* normality (S-W *W*) and probability are reported. Control units are reported as (Con). "*"denotes a normal distribution.

Unit ID	*n*	S-W *W*	*P*	Unit ID	*n*	S-W *W*	*P*
E	128	0.9823	=0.0927*	(P)	125	0.9282	<0.0001
F	125	0.8664	<0.0001	(Q)	125	0.9793	=0.0517*
G	130	0.913	<0.0001	(R)	125	0.9167	<0.0001
J	121	0.8931	<0.0001	(T)	125	0.9503	<0.0002
K	124	0.9597	<0.0001	(U)	125	0.9423	<0.0001
L	122	0.9625	=0.0018	(V)	121	0.971	=0.0104
				(Y)	128	0.964	=0.0018

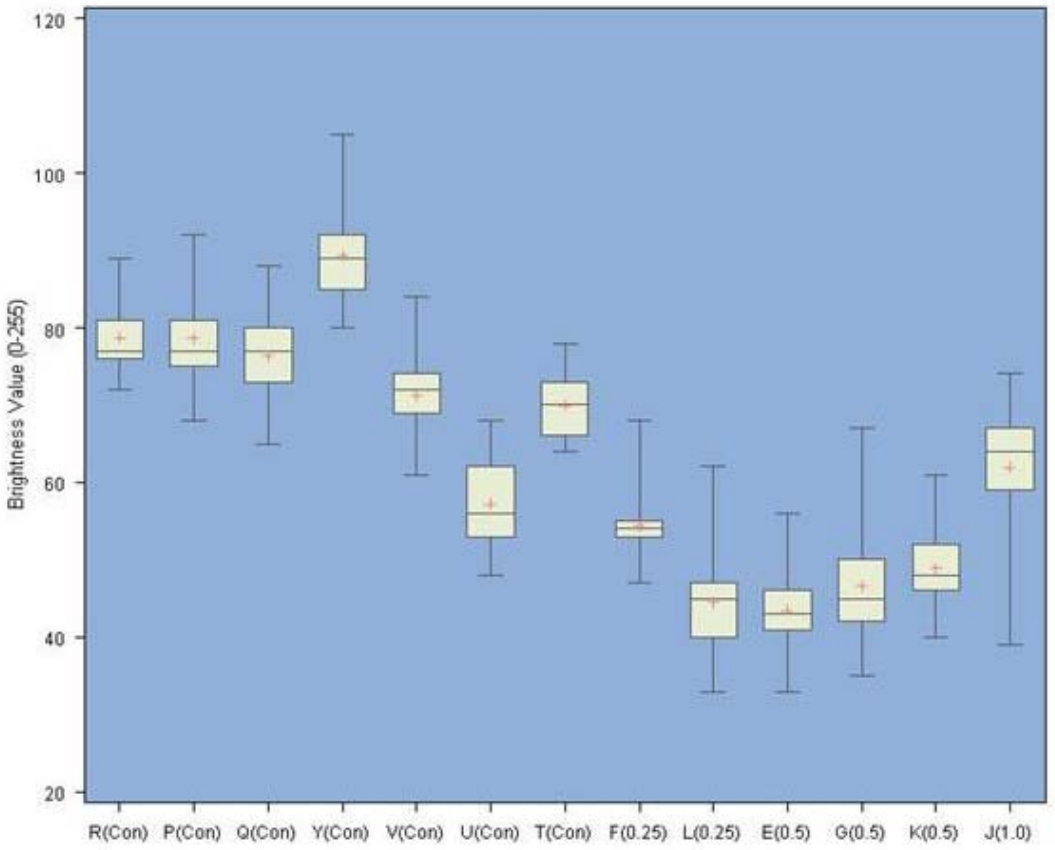

Figure 14. Box plots of five number summaries for the 13 samples extracted from image 4r25. Plots are arranged left to right by increasing depth of disturbance, from control (no disturbance) to one meter. Depths are presented in "()" next to the unit identifier.

Table 7. Results of Kruskall-Wallis analysis of variance on ranked data, Student-Neumann-Keuls on ranked data, and Spearman's correlation analysis on image series 4_25. Samples from each image are highly significantly different from each other and separate out into statistically groups. Depths are reported as (meters). (Con) denotes no disturbance (depth = 0m). Significant negative correlation between depth of disturbance and brightness value is noted.

Image	K-W *H*	DF	*P*	SNK Grouping	r_s	*P*
4r25	1436.42	12	< 0.0001	Y(con) > R(con) = P(con) > Q(con) > V(con) > T(con) > J(1.0) > U(con) > F(0.25) > K(0.5) > G(0.5) > L(0.25) > E(0.5)	-0.7198	< 0.0001
4r25f	1421.65	12	< 0.0001	Y(con) > R(con) > P(con) = Q(con) > V(con) > T(con) > J(1.0) > U(con) > F(0.25) > K(0.5) > G(0.5) = L(0.25) > E(0.5)	-0.7103	< 0.0001
4e25	5147.09	11	< 0.0001	Y(con) > R(con) = P(con) > Q(con) > V(con) > U(con) > J(1.0) > F(0.25) > K(0.5) = L(0.25) > G(0.5) > E(0.5)	-0.7376	< 0.0001
4e25f	6318.89	14	< 0.0001	Y(con) > R(con) > P(con) > Q(con) > V(con) > J(1.0) > U(con) > F(0.25) > H(1.5) > K(0.5) > G(0.5) = L(0.25) > E(0.5) > N(1.0) > M(0.5)	-0.6655	< 0.0001

Statistical separations presented in Table 7 were not clear on first observation. The sets were examined independently to determine if this was due to differences between the unit sets: Set A units with associated controls, and; Set B samples with

nearby controls. Significant sample differences (Kruskall-Wallis) and distinct groups (SNK on ranked data) were observed within each set. Negative correlation between unit depth and signature was also observed (Spearman's ranked correlation), however, the relationship was much more pronounced within Set A. Results are presented for image 4r25 Sets A and B in Table 8. Sample box plots for the separated sets are presented in Figure 15.

Table 8. Results of Kruskall-Wallis analysis of variance on ranked data, Student-Neumann-Keuls on ranked data, and Spearman's correlation analysis on Sets A and B of image 4r25. Negative correlation is significant for both sets, but is less pronounced in Set B.

Image	K-W *H*	DF	*P*	SNK Grouping	r_s	*P*
4r25 Set A	617.08	5	< 0.0001	R(con) = P(con) > Q(con) > F(0.25) > G(0.5) > E (0.5)	-0.8971	< 0.0001
4r25 Set B	741.84	6	< 0.0001	Y(con) > V(con) > T(con) > J(1.0) > U(con) > K(0.5) > L(0.25)	-0.5634	< 0.0001

a. 4r25 Set A

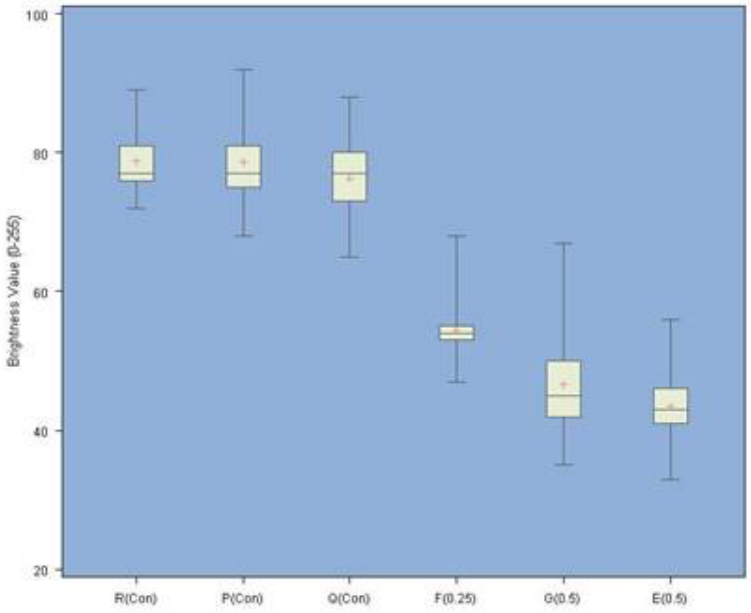

b. 4r25 Set B

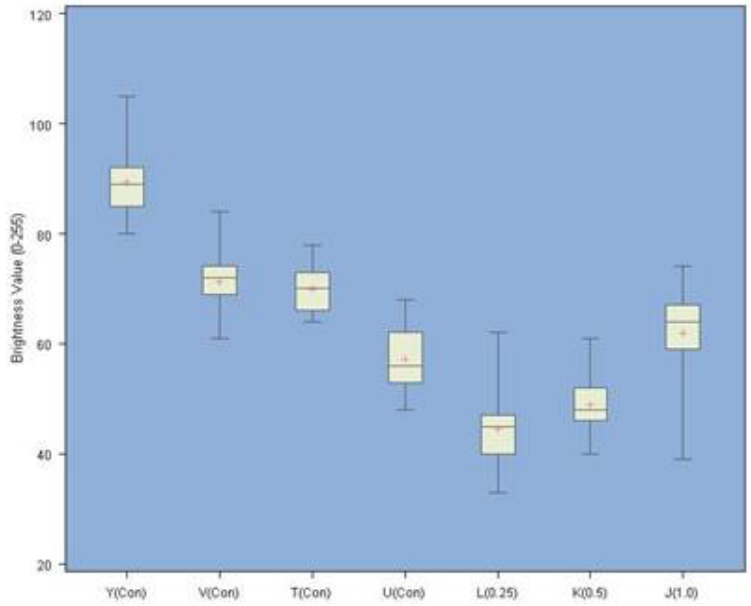

Figure 15. Box plots of five number summaries for Sets A and B samples extracted from image 4r25. Plots are arranged left to right by increasing depth of disturbance, from control (no disturbance) to one meter. Depths are presented in "()" next to the unit identifier.

4.1.4 Image Series 5_26

The 5_26 set consisted of four wide FOV shots over the entire site. The three preliminary units were not visible. All other units appeared relatively cool. Cell sizes for the two raw images (5r26 and 5r26f) were 0.15 meters; the corresponding enhanced pair was 0.07 meters. Each image yielded a minimum of 19 samples (10 units, 9 controls). Image 5r26 is presented in Figure 16, below. The remainder of the image series is presented in Appendix I.

Samples extracted from both enhanced images (5e26 and 5e26f) consisted of distributions significantly different from normal (Shapiro-Wilks normality test). 21 samples were extracted from image 5r26 (11 units, 10 controls), of which ten were normally distributed (Table 9). Likewise, six of the 20 samples extracted from 5r26f were normal. Five number summary box plots for samples collected from 5r26 may be viewed in Figure 17. Normality and descriptive statistics for images 5r26f, 5e26, and 5e26f are presented in Appendix J.

With respect to each image in the series, samples extracted were highly significantly different from each other (Kruskall-Wallis analysis of variance on ranked data). Although these samples separated into statistically distinct groups (SNK on ranked data), the combination of both Sets A, B and all controls made interpretation difficult. Additionally, significant negative correlation was noted between signature and depth (Spearman's ranked correlation), although the association appears to be somewhat weak. Results for each of the above analyses are reported in Table 10.

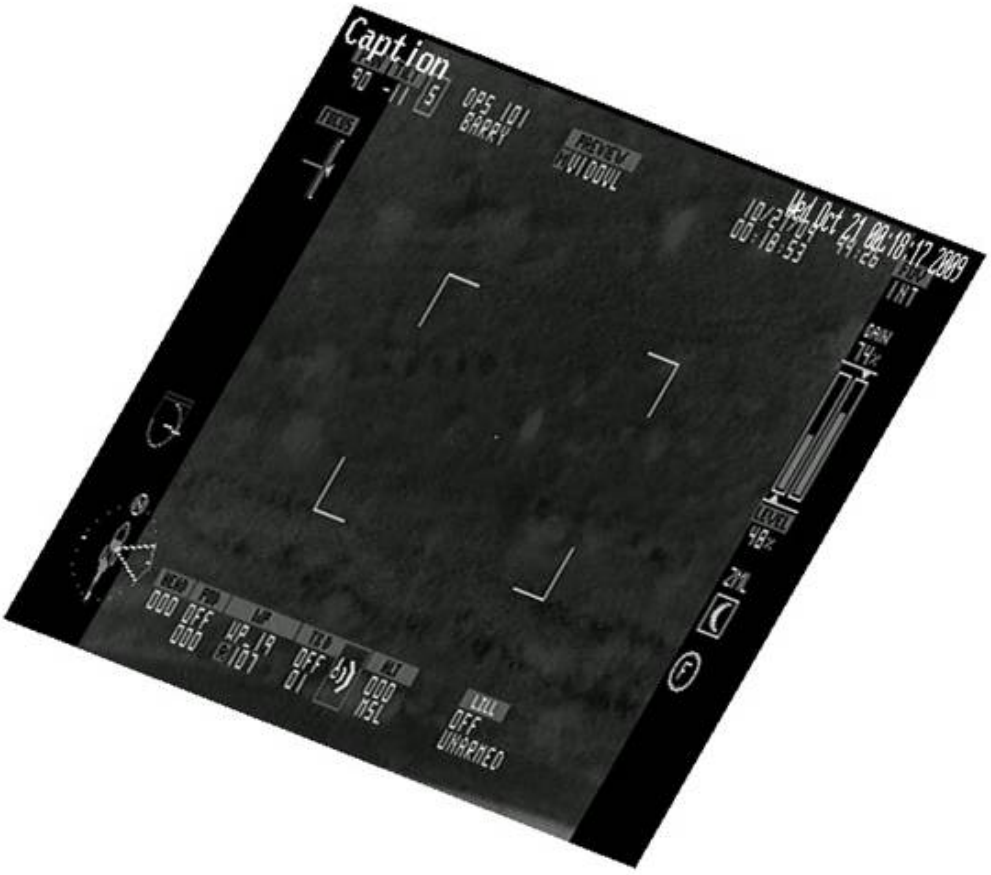

Figure 16. Image 5r26, a wide FOV image over the entire site. The light colored object in the middle is a cedar tree (relatively warm). Set A units are located above and to the left of the tree, while Set B units are located below and slightly to the right. Both unit sets appear relatively cool. Preliminary units could not be discriminated in this flight.

Table 9. Sample size and normality results for BV sample distributions extracted from image 5r26. Shapiro-Wilk *W* normality (S-W *W*) and probability are reported. Control units are reported as (Con). "*" denotes a normal distribution.

Unit ID	*n*	S-W *W*	*P*	Unit ID	*n*	S-W *W*	*P*
E	59	0.9592	=0.05*	(P)	56	0.951	=0.0236
F	56	0.9737	=0.2585*	(Q)	56	0.9787	=0.4204*
G	60	0.9614	=0.0553*	(R)	56	0.7828	<0.0001
H	60	0.9538	=0.0237	(S)	56	0.962	=0.0754*
I	60	0.9764	=0.2962*	(T)	56	0.9394	=0.0073
J	55	0.9457	=0.0149	(U)	56	0.9364	=0.0055
K	54	0.9536	=0.0358	(V)	55	0.9433	=0.0117
L	54	0.9349	=0.0058	(W)	55	0.9687	=0.1605*
M	54	0.9761	=0.3517*	(X)	60	0.977	=0.3147*
N	55	0.9313	=0.0037	(Y)	60	0.9679	=0.1148*
O	54	0.9588	=0.0608*				

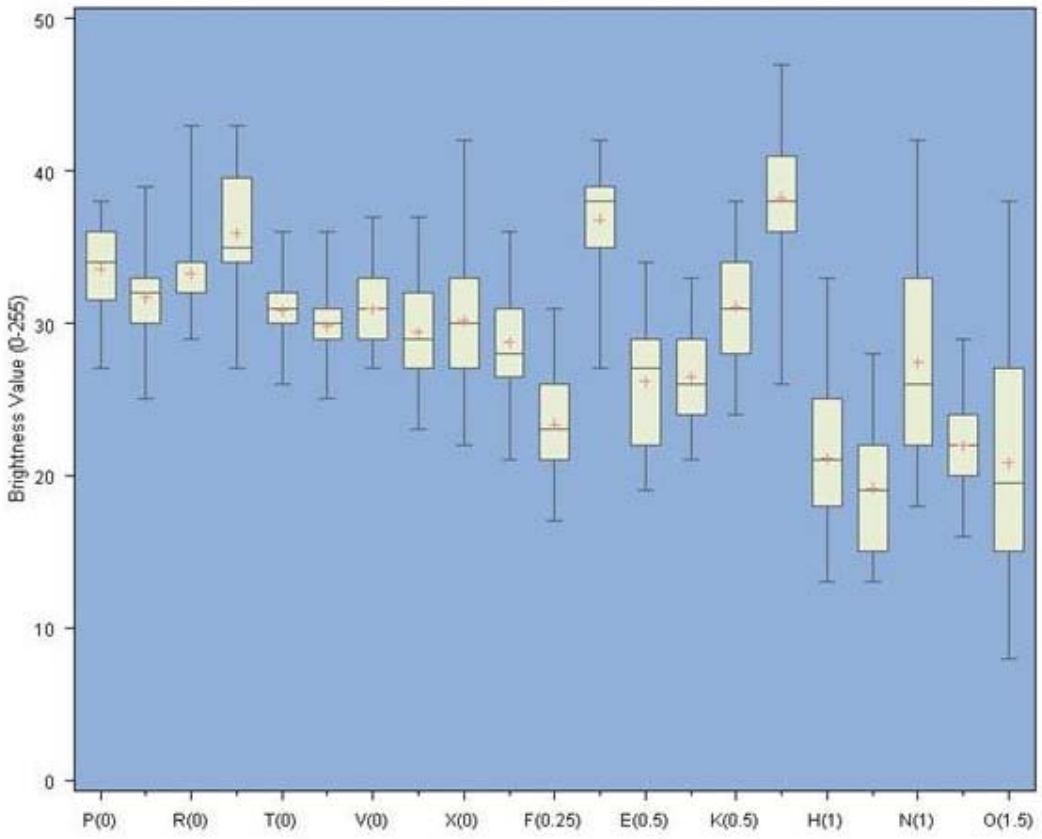

Figure 17. Box plots of five number summaries for the 21 samples extracted from image 5r26. Plots are arranged left to right by increasing depth of disturbance, from control (no disturbance) to 1.5 meters. Depths are presented in "()" next to the unit identifier.

Table 10. Results of Kruskall-Wallis analysis of variance on ranked data, Student-Neumann-Keuls on ranked data, and Spearman's correlation analysis on image series 5_26. Samples from each image are highly significantly different and separate out statistically. Depths are reported as (meters). (Con) denotes no disturbance (depth = 0m). Significant negative correlation between depth of disturbance and brightness value is noted.

Image	K-W *H*	DF	*P*	SNK Grouping	r_s	*P*
5r26	749.96	20	< 0.0001	M(0.5) = L(.25) = S(0) > P(0) = R(0) > Q(0) = K(0.5) = V(0) = T(0) = X(0) = U(0) = W(0) = Y(0) > N(1) = G(0.5) = E(1) > O(1.5) = F(0.25) = H(1) = I(1.5) = J(1)	-0.4951	< 0.0001
5r26f	634.8	19	< 0.0001	M(0.5) = L(.25) = P(0) = R(0) > S(0) = Q(0) = T(0) > K(0.5) = V(0) > X(0) = U(0) = E(0.5) = W(0) > G(0.5) = Y(0) = N(1) > H(1) = F(0.25) = I(1.5) = J(1)	-0.3945	< 0.0001
5e26	3906.49	20	< 0.0001	M(0.5) > S(0) = L(0.25) > R(0) = P(0) > Q(0) > K(0.5) = V(0) = T(0) = U(0) > X(0) > Y(0) = N(1) = E(0.5) > G(0.5) = W(0) > F(0.25) > I(1.5) = O(1.5) > H(1) > J(1)	-0.5043	< 0.0001
5e26f	3406.99	19	< 0.0001	M(0.5) > S(0) > P(0) = R(0) = L(0.25) > Q(0) = K(0.5) = U(0) = W(0) = T(0) > V(0) > E(0.5) = X(0) > Y(0) > N(1) = Q(0) > F(0.25) > H(1) = I(1.5) > J(1)	-0.4964	< 0.0001

Much like the case for image 4r25, group separation presented in Table 10 was not clear. Units for this image were re-examined independently by set. Significant differences were noted between samples within a Set (Kruskall-Wallis). Statistical groups emerged from both sets (SNK on ranked data), although Set B remained somewhat ambiguous. Negative correlation between unit depth and signature was also observed (Spearman's ranked correlation). Again, similar to that seen for image 4r25, the relationship was relatively stronger within Set A. Analyses results for both sets of image 5r26 are presented Table 11; box plots of the samples are available in Figure 18.

Table 11. Results of Kruskall-Wallis analysis of variance on ranked data, Student-Neumann-Keuls on ranked data, and Spearman's correlation analysis on Sets A and B of image 5r26. Negative correlation is significant for both sets, but is much less pronounced in Set B.

Image	K-W *H*	DF	*P*	SNK Grouping	r_s	*P*
5r26 Set A	365.63	8	< 0.0001	S(con) > P (con) > R(con) > Q(con) > G(0.5) > E(0.5) > F(0.25) > I(1.5) > H(1.0)	-0.6855	< 0.0001
5r26 Set B	353.58	11	< 0.0001	M(0.5) = L(0.25) > K(0.5) = T(con) = V(con) = X(con) = U(con) = W(con) = Y(con) = N(1.0) > O(1.5) > J(1.0)	-0.2291	< 0.0001

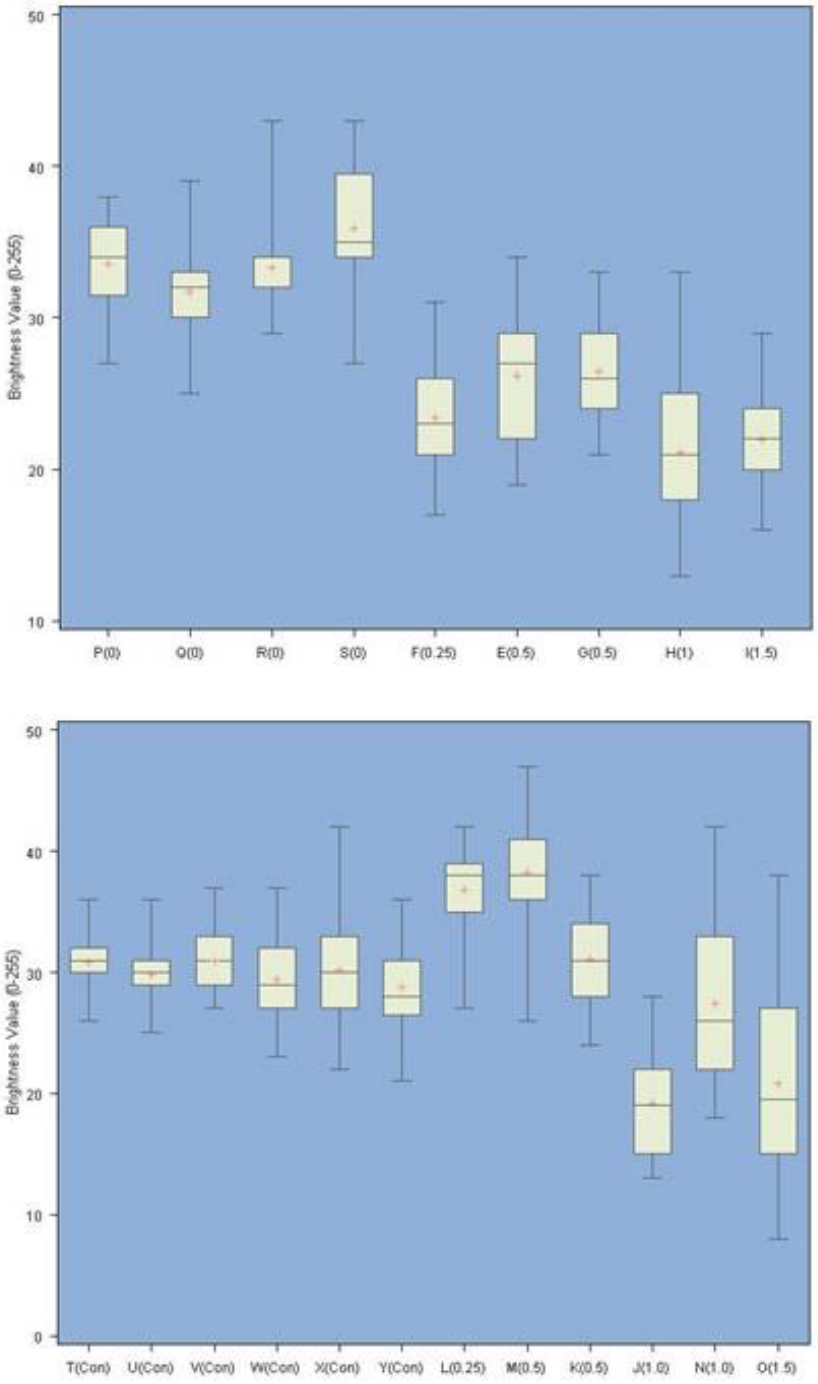

Figure 18. Box plots of five number summaries for Sets A and B samples from image 5r26. Plots are arranged left to right by increasing depth of disturbance, from control (no disturbance) to 1.5 meters. Depths are presented in "()" next to the unit identifier.

4.2 Classification Study

All classifications were performed on rectified images generated for the statistical analyses described above. Selections were cropped prior to classification to exclude a maximum amount of unnecessary readout information on the image periphery. Series 1_23, 4_25 and 6_11 were used in the classification study based on both good visual discrimination and differing FOV's over the research area. Series 5_26 was excluded from this portion of the study due to the previously mentioned calibration issues. Presented below are classifications and accuracy assessments for the complete series 1_23, and individual images 6r11 and 4r24. The remainder of the classified images and assessments for series 6_11 and 4_24 are presented in Appendices K and L, respectively.

4.2.1 Image Series 1_23

The four images comprising series 1_23 were classified by both supervised and object-oriented methods. Classes attempted for the supervised set included the following: 1.0 meter units; 0.5 meter units; Preliminary units (grouped); Trees; Control, and; Readout. The 0.25 meter unit (F) blended primarily with the control class in all four cases. Output images generated with the supervised technique are presented in Figure 19, a-d, with associated legends.

Image 1r23 was the sole member of the group to contain all six classes in the final output. Class overlap was noted, primarily between the 1.0 meter and Preliminary unit classes. Additionally, the "unknown" 1.0 meter unit (H) classified at 0.5 meters, while the like 0.5 meter unit (G) blended with Control. Unit I (1.5 meters deep) grouped

spectrally with the 1.0 meter class. The remaining three images yield similar output classifications, although fewer classes were generated: significant signature overlap required class merging.

The same original image series was then subjected to an object-oriented procedure. Output classes for each image included: 1.5 meter units; 1.0 meter units; 0.5 meter units; 0.25 meter units; Preliminary units (grouped); Trees, and; Control. The Readout class was not applied. Following segmentation, some image objects were merged, including those associated with preliminary units in image 1r23, all units in images 1r23f, 1e23, and 1e23f, and trees for images 1e23 and 1e23f. Each of the above classes was then successfully generated. The output classifications, with legends, are presented in Figure 20,a-d. Accuracy levels by class and overall were considerably higher (approaching or at 100%) for the eCognition-produced images. Assessments are presented below in Table 12,a-d (supervised) and Table 13, a-d (object-oriented).

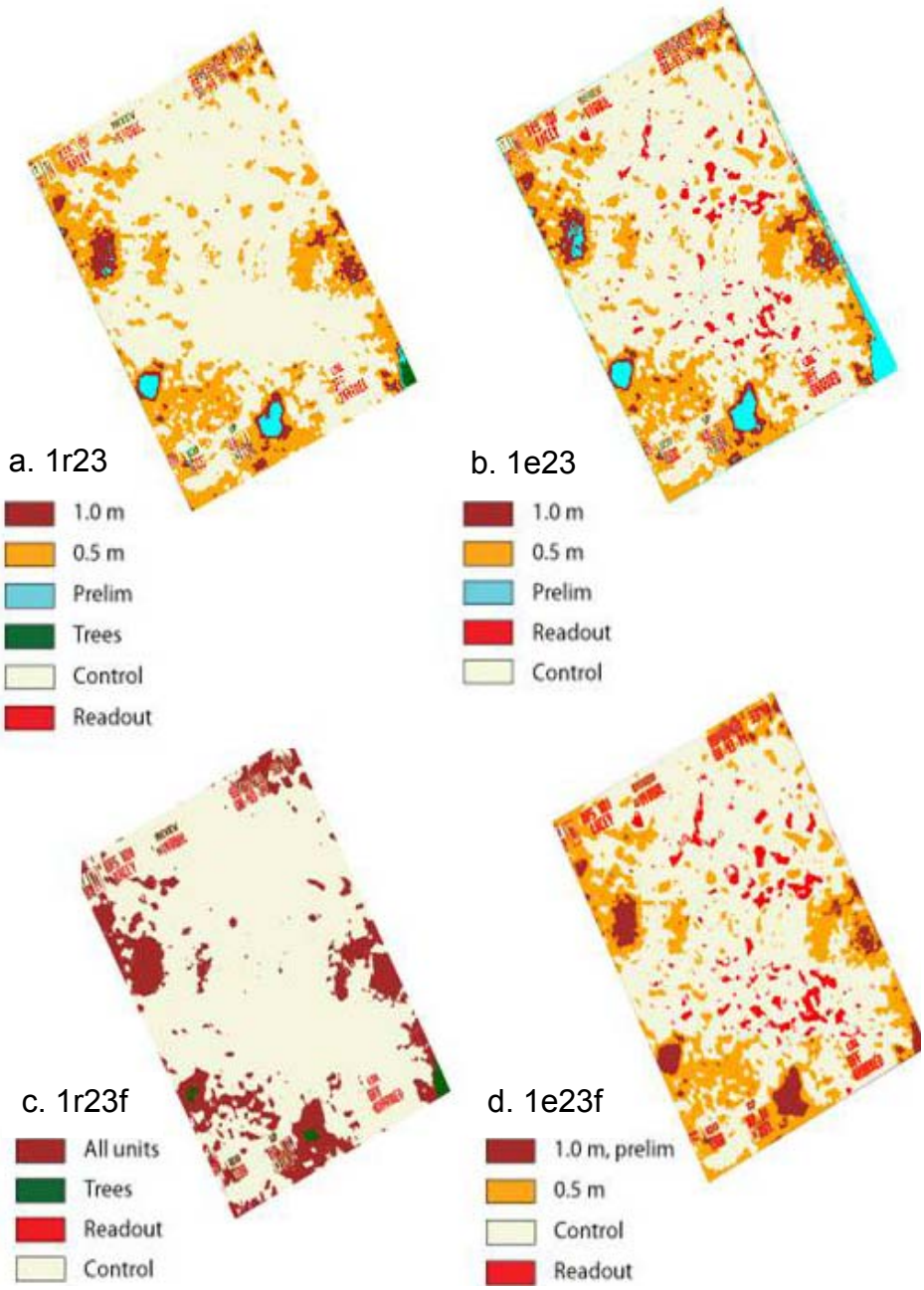

Figure 19, a-d. Supervised classifications of series 1_23.

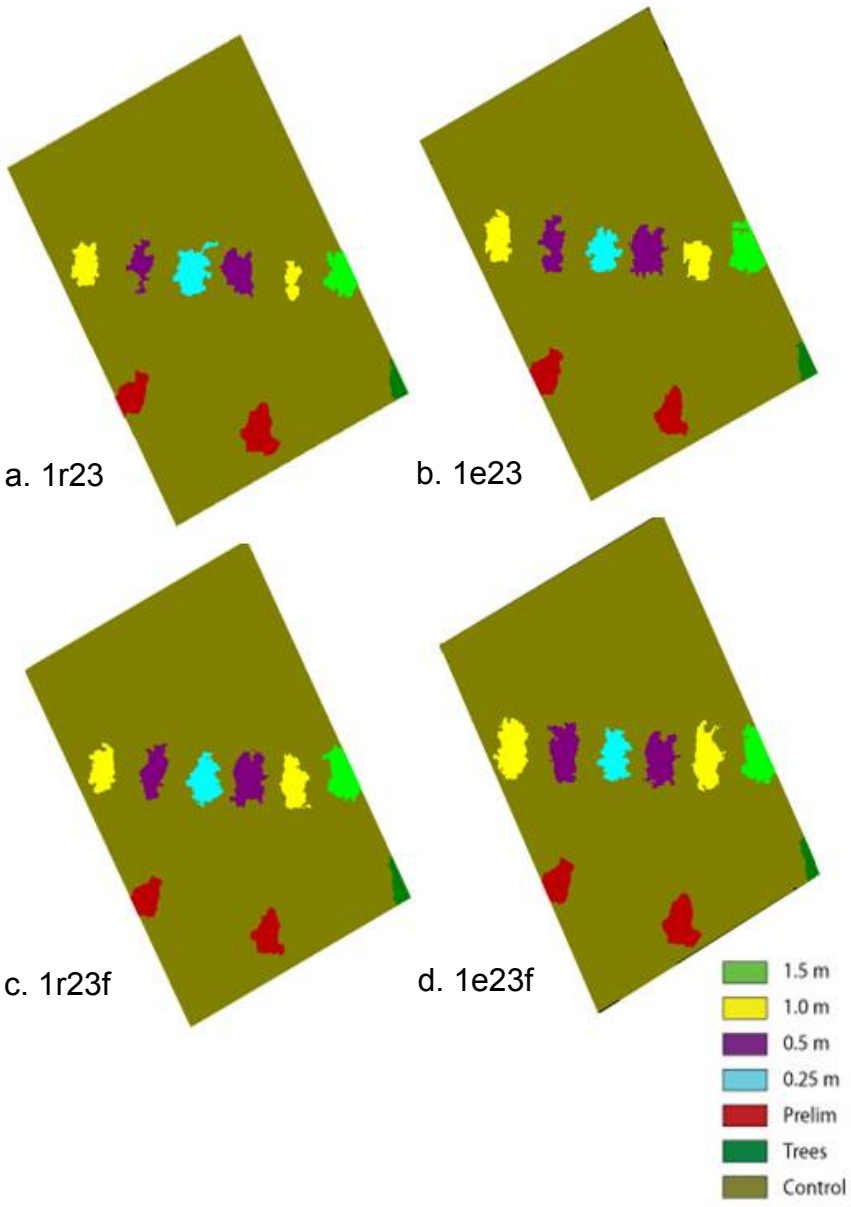

Figure 20, a-d. Object-oriented classifications of series 1_23.

Table 12, a-d. Supervised classification accuracy tables for image series 1_23.

a. 1r23

Class Name	Reference Totals	Classified Totals	Number Correct	Producer Accuracy	User Accuracy	Cond. Kappa
Unit D	3	3	1	76.00%	88.37%	0.3005
Unit E	3	16	0	0.00%	33.33%	-0.0492
Preliminary	2	1	1	0.00%	0.00%	1
Control	50	43	38	50.00%	100.00%	0.4684
Tree	2	0	0	\	\	0
Readout	4	1	1	25.00%	100.00%	1
Total	**64**	**64**	**39**			
Overall Accuracy 64.06%						
Overall Kappa	**0.2183**					

b. 1r23f

Class Name	Reference Totals	Classified Totals	Number Correct	Producer Accuracy	User Accuracy	Cond. Kappa
Unit D	5	3	1	20.00%	33.33%	0.2768
Unit E	2	15	0	0.00%	0.00%	-0.0323
Prelim/Tree	6	3	3	50.00%	100.00%	1
Control	46	40	33	71.74%	82.50%	0.3778
Readout	5	3	2	40.00%	66.67%	0.6384
Total	**64**	**64**	**39**			
Overall Accuracy 60.94%						
Overall Kappa	**0.2654**					

c. 1e23

Class Name	Reference Totals	Classified Totals	Number Correct	Producer Accuracy	User Accuracy	Cond. Kappa
Units	13	12	4	30.77%	33.33%	0.1634
Control	47	51	39	89.98%	76.47%	0.1142
Readout	4	1	1	25.00%	100.00%	1
Total	**64**	**64**	**44**			
Overall Accuracy 68.75%						
Overall Kappa	**0.1683**					

d. 1e23f

Class Name	Reference Totals	Classified Totals	Number Correct	Producer Accuracy	User Accuracy	Cond. Kappa
Unit D	6	4	4	66.67%	100.00%	1
Unit E	7	15	0	0.00%	0.00%	-0.1228
Control	50	41	34	68.00%	82.93%	0.2195
Readout	1	4	1	100.00%	25.00%	0.2381
Total	**64**	**64**	**39**			
Overall Accuracy 60.94%						
Overall Kappa	**0.1636**					

Table 13, a-d. Object-oriented classification accuracy tables for image series 1_23.

a. 1r23

Class Name	Classified Totals	Number Correct	Producer Accuracy	User Accuracy	Cond. Kappa
1.5 meter units	1004	1004	100.00%	100.00%	1
1.0 meter unit	924	924	100.00%	100.00%	1
0.5 meter unit	679	679	100.00%	100.00%	1
0.25 meter unit	1280	1280	100.00%	100.00%	1
Old Units	947	947	100.00%	100.00%	1
Control	15061	15061	100.00%	100.00%	1
trees	483	483	100.00%	100.00%	1
Total	**20378**	**20378**			
Overall Accuracy	**100.00%**				
Overall Kappa	**1.00**				

b. 1r23f

Class Name	Classified Totals	Number Correct	Producer Accuracy	User Accuracy	Cond. Kappa
1.5 meter units	1262	1262	100.00%	100.00%	1
1.0 meter unit	803	803	100.00%	100.00%	1
0.5 meter unit	972	972	100.00%	100.00%	1
0.25 meter unit	1052	1052	100.00%	100.00%	1
Old Units	1049	1049	100.00%	100.00%	1
Control	8641	8641	100.00%	100.00%	1
trees	3693	3693	100.00%	100.00%	1
Total	17472	17472			
Overall Accuracy	**100.00%**				
Overall Kappa	**1.00**				

c. 1e23

Class Name	Classified Totals	Number Correct	Producer Accuracy	User Accuracy	Cond. Kappa
1.5 meter units	8460	8460	0.00%	\	0
1.0 meter unit	6222	6222	100.00%	100.00%	1
0.5 meter unit	8934	8934	100.00%	100.00%	1
0.25 meter unit	7863	7863	100.00%	100.00%	1
Old Units	5718	5718	100.00%	100.00%	1
Control	47326	47326	100.00%	100.00%	1
trees	3382	3382	100.00%	100.00%	1
Total	**87905**	**87905**			
Overall Accuracy	**90.38%**				
Overall Kappa	**0.8573**				

d. 1 e 23f

Class Name	Classified Totals	Number Correct	Producer Accuracy	User Accuracy	Conditional Kappa
1.5 meter units	7712	7712	100.00%	100.00%	1
1.0 meter unit	8762	8762	100.00%	100.00%	1
0.5 meter unit	8790	8790	100.00%	100.00%	1
0.25 meter unit	7489	7489	100.00%	100.00%	1
Old Units	8358	8358	100.00%	100.00%	1
Control	29729	29729	100.00%	100.00%	1
trees	3703	3703	100.00%	100.00%	1
Total	**74543**	**74543**			
Overall Accuracy	**100.00%**				
Overall Kappa	**1.00**				

4.2.2 Image Series 6_11

Series 6_11 was subjected to the same routine described above. Classes sampled for the supervised classification included 1.0 meter and 0.5 meter units, Control, Trees, Ditch and Readout. The 0.25 meter unit (L) again blended primarily with the Control class. Each image in this series exhibited 100% spectral overlap between the Ditch, Tree, and two Unit classes and were therefore merged into one class (“Units,

etc."): the output observed in Figure 21a (supervised classification of image 6r11) includes the combined Units, Control, and Readout classes.

Images classified with eCognition® consisted of the above listed classes (sans Readout), as well as 0.25 meter and 1.5 meter units. Following segmentation, objects associated with Trees, Ditch, and some units (J, K and L) were manually merged. Similar to series 1_23, all classes were present in the output image: please see Figure 21b, object-oriented classified version of 6r11. Accuracy assessments are reported in Table 14. Overall accuracy for both methods as applied to image 6r11was high (93.75% and 100.00%, respectively); however, the seven thematic classes associated with the object-oriented output are more informative.

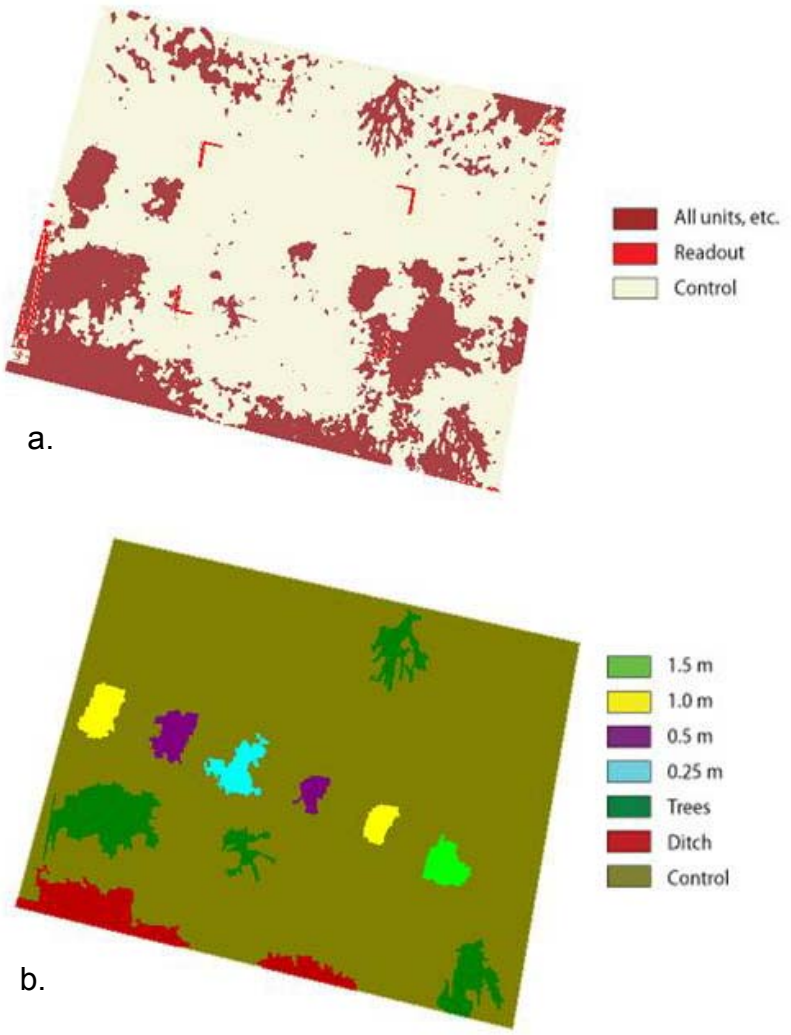

Figure 21. Supervised (a) and (b) object-oriented classifications of image 6r11.

Table 14. Accuracy assessments for supervised (a) and object-oriented (b) classifications of image 6r11.

a.

Class Name	Reference Totals	Classified Totals	Number Correct	Producer Accuracy	User Accuracy	Cond. Kappa
Unit, etc.	17	17	15	88.24%	88.24%	0.8398
Control	47	47	45	97.74%	97.74%	0.8398
Readout	0	0	0	\	\	0
Total	**64**	**64**	**60**			
Overall Accuracy 93.75%						
Overall Kappa 0.8398						

b.

Class Name	Classified Totals	Number Correct	Producer Accuracy	User Accuracy	Cond. Kappa
1.5 meter units	987	987	100.00%	100.00%	1
1.0 meter unit	1069	1069	100.00%	100.00%	1
0.5 meter unit	502	502	100.00%	100.00%	1
0.25 meter unit	1157	1157	100.00%	100.00%	1
Control	11470	11470	100.00%	100.00%	1
Trees	687	687	100.00%	100.00%	1
Ditch	1027	1027	100.00%	100.00%	1
Total	**16899**	**16899**			
Overall Accuracy	**100.00%**				
Overall Kappa	**1.00**				

4.2.3 Image Series 4_25

Although the application of supervised classification to series 4_25 yielded an increased number of classes over the previous image series (Ditch, Trees, Control, Readout), newer and preliminary unit signatures could not be separated out and were thus merged into one class. This was the case for all four images. Presented in Figure 22a is image 4r25, as classified with Erdas Imagine®. Significant, but not complete, signature overlapping is noted between the following classes: Units; Trees, and; Ditch.

Classes for Individual units by depth of disturbance (1.5, 1.0, 0.5 and 0.25 meters), as well as Preliminary Units, Trees, Ditch, and Control, were successfully generated with eCognition®. Prior to classification, tree-related objects were merged in all four images. Unit objects were merged only in image 4e25f. Figure 22b displays the object-oriented classification of image 4r25. Irregular unit classifications can be observed in both Sets A and B. These include the following: an elongated footprint for unit H (Set A); incomplete classification for unit J (Set B), and; Set B units N (1.0 meter) and O (1.5 meter) both classified as 1.0 meter units. Additionally, minor misclassifications included portions of the central targeting readout which was classified as Ditch, 0.5 meter and 1.0 meter units. An area adjacent to unit N (1.0 meter) was misclassified as a tree. Overall accuracy was still considerably higher for the object-oriented rather than supervised output (94.67% vs. 62.5%). Complete accuracy assessments for both 4r25 classification outputs are presented in Table 15.

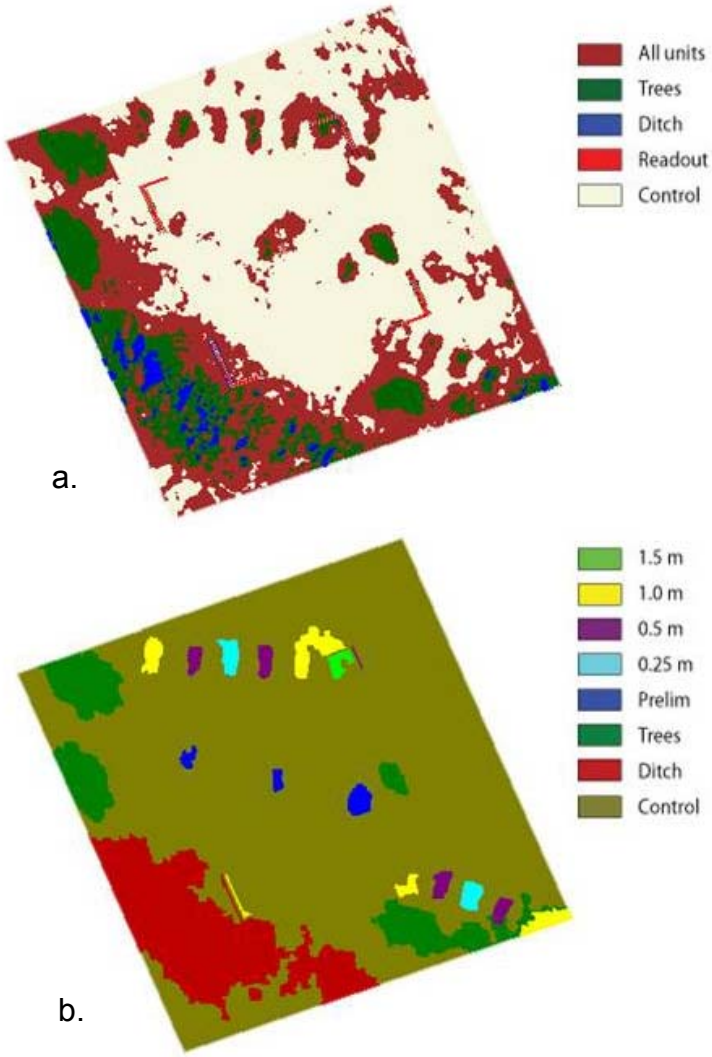

Figure 22. Supervised (a) and (b) object-oriented classifications of image 4r25.

Table 15. Accuracy assessments for supervised (a) and object-oriented (b) classifications of image 4r25.

a.

Class Name	Reference Totals	Classified Totals	Number Correct	Producer Accuracy	User Accuracy	Cond. Kappa
Units	8	20	4	50.00%	20.00%	0.0857
Trees	5	8	3	60.00%	37.50%	0.322
Ditch	9	1	1	11.11%	100.00%	1
Control	42	35	32	76.19%	91.43%	0.7506
Readout	0	0	0	\	\	0
Total	**64**	**64**	**40**			
Overall Accuracy 62.50%						
Overall Kappa 0.3645						

b.

Class Name	Reference Totals	Classified Totals	Number Correct	Producer Accuracy	User Accuracy	Cond. Kappa
1.5 meter units	201	201	201	100.00%	100.00%	1
1.0 meter unit	155	155	155	100.00%	100.00%	1
0.5 meter unit	176	176	176	100.00%	100.00%	1
0.25 meter unit	258	258	258	100.00%	100.00%	1
Old Units	107	107	107	100.00%	100.00%	1
Control	11896	12566	11896	94.67%	100.00%	0.7254
Trees	320	320	320	100.00%	100.00%	1
Ditch	1650	980	980	100.00%	59.39%	
Total	**14763**	**14763**				
Overall Accuracy	**94.67%**					
Overall Kappa	**0.7451**					

CHAPTER 5

DISCUSSION

5.1 Visual Examination of Unit Signatures

Clear, visual discrimination between disturbed units and the undisturbed background area was noted for nearly all flight surveys, with the exceptions of the preliminary and second flights. This contrast was expected based on previous research and cited literature. Generally speaking, disturbed unit signatures were more pronounced (darker) and displayed relatively defined margins with some degree of linearity. Adjacent control areas typically exhibited a lighter signature. Exceptions to this pattern occurred primarily along the northern and eastern portions of the research site, where control areas appeared slightly darker. However, no obvious linear orientations were observed in these undisturbed areas.

Disturbed units appeared relatively cool during the preliminary flight. It was assumed that disturbed units should appear relatively cooler than undisturbed surroundings in the absence of exothermic decomposition prior to the first survey in August 2008. The seven flights, including April 2006, were conducted in various weather regimes. The recorded thermal scans revealed that on a given flight, disturbed units could appear relatively warm, cool, or not visible at all. Disturbances appeared cool only on two flights, the preliminary and flight 5, and were relatively warm during flights 1, 3, 4 and 6. Flight 2 video yielded poor to no discrimination between units and the surroundings. The Preliminary Set appeared slightly warmer than the surroundings, but the remainder of units in Sets A and B could not be readily observed. The poor

results for this flight were due to excessive cloud cover prior to the flight, which minimized daytime solar loading of the surface.

The differences observed across the seven flights suggest that unit signature is dependent upon multiple weather-related variables, such as temperature, cloud cover, precipitation, relatively humidity, etc. However, an overall pattern between underlying weather conditions and resultant unit signature cannot be surmised due to the relatively low number of flights. Additionally, other variables not studied in this project, including soil moisture, soil temperature, porosity, and others, are also likely to be major factors in observed signatures. The only conclusion to be drawn at this point is that potential burials, in this or similar contexts, should appear as either hot or cold thermal defects that contrast with the neighboring or surrounding background. Future research should investigate the potential relationships between these and other variables, and their possible effects on thermal signature.

Manipulation of the images by enhancement and/or filtering methods did tend to increase visual contrast between the disturbed units and the control areas. However, these procedures did not have pronounced effects on the statistical relationships described in Chapter 4, and in some situations, the results became muddied. Similarly, accuracy assessments for classifications of manipulated images were for the most part no different than classifications performed on raw rectified frames. This was the case for both classification methods. This demonstrates that although image manipulation may qualitatively provide better visual discrimination between features, these techniques are not necessary for quantitative assessment.

5.2 Statistical Analyses

Based on the pilot study, it was predicted that unit signatures would not only be significantly different from undisturbed areas, but those signatures would also vary based on the depth of disturbance as well. Differences between disturbed and control areas were demonstrated statistically. Regarding the question of depth-related variation, there appeared to be a visual relationship between unit depth and the associated thermal signature in many of the selected images. Samples extracted from control areas and disturbed units were analyzed, revealing a significant negative correlation between depth and signature: signatures became more pronounced as the depth of the disturbances increased. This relationship was consistent in near FOV imagery of both Sets A and B.

It was also predicted that units of similar like depth would not be significantly different from each other and should group together into statistically distinct groups (i.e., control equals control, 0.5 meter equals 0.5 meter, etc.). It was further surmised that these groupings would be consistent across the two sets in the wide field of view imagery. These latter two predictions turned out to be incorrect.

Samples extracted from each unit and control area did separate out as statistically distinct groups from each other; however, like samples did not typically group together. This occurred because the signature samples were heterogeneous. Undisturbed areas were especially variable, with some spectral overlap with the darker disturbed unit signatures. Major factors likely included the following: slight differences in surface vegetation (e.g., vegetation density, height, among others); immediate

topography, as discussed below, and; limitations from collecting spectral information in only one band.

Although equal units did not group together, they did tend to separate out statistically by depth in near FOV images. Control samples were composed of higher mean-ranked pixels, meaning associated BVs in the original unranked samples were of higher value (approaching 255, or white). Thus, these samples generally separated out first. Conversely, lower-ranked samples extracted from disturbed units of greater depth, such as 1.0 and 1.5 meter units, tended to fall out last.

The shallowest units (0.25 meter) generally separated out just after, or sometimes interspersed, with the control samples. This was due to the high degree of signature overlap previously mentioned. In practical terms, this suggests that at least in this environmental setting, shallow burials are less likely to be discriminated thermally than deeper disturbances. The caveat to this would be that a shallow burial is probably of greater likelihood to be discovered by a ground search due to partial exposure of the interred remains.

The remaining disturbed units (0.5, 1.0 and 1.5 meters, respectively) were more likely to separate by depth, although there was overlap as depth increased. In some instances, 1.0 and 1.5 meter samples were not significantly different. Other cases presented 1.0 meter units that separated out as the lowest ranked group. This was not completely surprising, given unit appearances in the images. Aside from slight variation in unit shape, 1.0 and 1.5 meter units were spectrally similar, with BVs approaching zero. This similarity between deeper units suggests that although there is a significant negative association between depth of disturbance and unit signature, even greater

increases in depth (e.g., 2.0, 3.0, and 5.0 meters) are unlikely to yield a signature much different from that of a 1.5 meter unit.

Statistical relationships between the depth of disturbance and signature were much more confusing when dealing with wide FOV frames that encompassed both Sets. A relatively weaker negative correlation was noted when including all extracted units and controls. Additionally, when plotted, like depth signatures in Set B did not approximate those of Set A. Set B unit separation by depth was not as evident, displaying a great degree of Set B signature overlap with shallower Set A units and controls.

Analyzing the two sets independently yielded significant negative correlation in both cases, although the Spearman's rho value for Set B samples was considerably lower. This outcome differed from the analyses performed on the near FOV examples previously discussed, where negative associations were much stronger. The two most likely culprits responsible for this are as follows: diminished spatial resolution and MCRT associated with the wider FOV lens, and; changes in the immediate site topography. Regarding the first factor, image MCRT and spatial resolution will decrease at a smaller scale. Scale decrease may be due to changes in flight elevation, or in the case of this project, FOV change. This occurs because there is only one sensor array directed at the AOI and with wider FOV imagery, there are fewer overall pixels available to resolve a particular feature. Differences at the research site between the two Sets are therefore more pronounced in the wider FOV imagery. These differences are due to both the previously mentioned heterogeneity of the surface as well as the site topography.

The research site was relatively flat, gradually decreasing in elevation from the north (Set A) to south (Set B) end by approximately 50 centimeters. However, Set B was located adjacent to a drainage ditch characterized by a sharp downward slope of more than 1.25 meters. Any moisture located in Set A and the Preliminary units would drain relatively slowly, through the deposits and horizontally across the longer slope. The presence of the ditch, an artificial cut through the original slope, likely lead to rapid differential draining of the nearby Set B units, and accounts for some of the differences in the resulting signatures.

5.3 Classification Study

Supervised and object-oriented algorithms were applied to three selected image series (12 total images). The eCognition® generated outputs were of higher accuracy for each image. Poor supervised accuracy was due to the high degree of spectral overlap between image features. Accuracy increased for object-oriented classifications because other image attributes aside from BVs could be included.

High accuracy for Erdas® supervised classification was only achieved with the Flight 6 series. However, only three actual classes were generated: Control, Readout, and Everything Else. Ignoring the Readout class, Control represents all of the relatively cool, undisturbed areas while the final combined class is comprised of the warm features, such as disturbed units, trees, and so on. These four output images therefore offered essentially the same information as the original thermal panels.

Signature confusion in supervised classifications was a major issue in the other two flight series as well. Associated accuracy levels were considerably lower for these

eight images. The shallowest unit (G, 0.25 meter) was lost in the Flight 1 near FOV series, registering primarily as Control. Adjacent “unknown” units at 0.5 meter (G) unit and 1.0 meter (H) were misclassified as well. Unit G also tended to merge with control, while unit H was classified into the 0.5 meter class. The 1.5 meter unit (I) registered as 1.0 meter. Additionally, there was significant signature overlap between the deeper units, the tree, and the preliminary units. Likewise, all units were merged into one class for the wide FOV Flight 4 series, with pronounced overlap between Unit, Tree and Ditch classes. Spectral confusion was not completely surprising, especially with the wide FOV imagery, given the results of the statistical analyses.

Classifications generated with eCognition® did not include a Readout class. The segmentation patterns in each of the 12 images allowed for readout components to be blended, for the most part, into the Control class. Each of the three image series yielded outputs with all desired classes (Control, Ditch, Trees, Preliminary Set, and newer units grouped by depth). Overall accuracy levels for many of the object-oriented classifications were approaching or at 100%, with the lowest for image 1e23 (90.38%). The considerably higher accuracy for these outputs was likely due to the ability to use spatial relationships, as previously noted.

Accuracy levels achieved with the eCognition® software on these selected images can be somewhat misleading to an analyst. These images are large scale, and the main features of interest, disturbed units, are limited in number. Accuracy for this group of classifications was assessed by TTA masks, which require selecting known objects from each class from the unclassified, segmented image. When only one object for a given class is available for sampling, as was the case for 0.25 and 1.5 meter units

in the two near FOV image series, resultant accuracy for that class will automatically be 100%. Accuracy levels would likely decrease at smaller scales, although in a grave search context, image scale would need to remain fairly large in order to detect such small features.

The addition of other spectral bands, such as visible light or reflective infrared, would likely increase overall classification accuracy for both methods, especially the traditional hard classifier. The use of the thermal band alone introduces too much signature overlap, making it extremely difficult to tease out individual features. Additional bands were not included in this project because the primary objective was to determine which method can be best applied to thermal imagery alone.

Object-oriented classification appears to be the best approach to thermal imagery collected by law enforcement. However, a real-world scenario would be considerably different from the approach of this study. Unit locations and dimensions involved in this project were known quantities and were therefore somewhat easier to classify out, especially when, following segmentation, unit-related objects could be manually merged. This luxury would not be afforded in an actual search. Application of this method in a true law enforcement context would have to be applied in reverse. Following image segmentation, readily identifiable objects, such as trees, culverts, or pathways, would be merged into the correct perspective classes and ignored. The remaining unclassified area would then need to be heavily scrutinized for potential burial sites.

CHAPTER 6

CONCLUSIONS AND FUTURE RESEARCH

The preceding research was conducted in an effort to improve the application of thermal imaging to clandestine burial searches. Prior research and literature suggested that burials, in the absence of exothermic decomposition, would look relatively cool when compared to the undisturbed background. It has now been determined, at least in this local context, that this is not the case. Such burials might appear relatively cool, warm, or neutral. Further, it has been demonstrated that when signatures can be discriminated, there is a relationship between the depth of a grave and the resultant thermal signature. Additionally, as depth decreases, the grave is more likely to blend into the background and be missed during a search. If a grave is not observed thermally in a real world search, flight personnel can interpret this information as follows: 1) the conditions, both on the ground and/or weather-related, may not be right for the search; 2) the grave depth is too shallow to discriminate thermally under present conditions, or; 3) there is no grave in the AOI.

The relationship between depth and signature is more pronounced at the larger scales provided by near FOV imagery. Likewise, the ability to detect clandestine burials is scale dependent: imagery needs to be fairly large scale due to these features being relatively small. With respect to law enforcement searches, the sensor platforms typically available (helicopter and fixed wing) can be flown at low enough altitudes that large scale imagery can be readily collected.

Thermal scans recorded by law enforcement agencies can be analyzed with classification methods currently available to remote sensing analysts. This research

suggests that object oriented algorithms are the more robust option for single band thermal imagery. The limited spectral information and the inability to use additional image attributes severely limits the abilities of more traditional hard classifiers.

Although much information was gained from this research, many new questions arose that require additional study. Foremost, the underlying pattern behind grave thermal appearance, cool, warm, or neutral, needs to be determined. A better understanding of the effects of local soil and climate conditions on grave signatures would not only identify for investigators the best times in which to conduct searches, it will also give investigators an idea of *what* they are looking for. This question could be examined using soil temperature and moisture probes placed at various depths in simulated burials and undisturbed cores taken from unit profiles. Along with a dedicated weather station for the site, all data could be recorded continuously to a logger located on site, coinciding with periodic aerial scans. Data could be downloaded and analyzed for patterns.

A related issue is the effect of actual interred biological material on grave signature. The assumption prior to the study was that in the absence of exothermic decomposition, a grave should appear relatively cool. Since this is not the case, the effect of adding biological mass to a burial on soil moisture, temperature, and surface signature requires study. This could be done in conjunction with the ground probe study previously described. The total research site could consist of undisturbed area, a set of control units at various depths with no added remains, and a set of units at like depths containing buried domestic pigs (*Sus scrofa domestica*), all with associated ground probes. To minimize the number of required flights, a thermal sensor could be mounted

on an elevated platform over the site to record at regular intervals, especially during the earlier exothermic stages of decomposition.

Lastly, the current research can only provide definitive information for the immediate area (Cross Timbers ecozone of Texas) and similar environments. Although certain observations collected here may be repeated elsewhere (e.g., variable unit thermal appearance, depth-signature correlation, etc.), this study should replicated elsewhere to verify or disprove consistency. Texas provides a variety of ecological environments, and DPS flight hangars are widely dispersed. One possibility would be to construct research sites in various parts of Texas (desert, high plains, piney woods, etc.) near existing DPS facilities. Sites could be scanned regularly by DPS investigators prior to or following routine missions without interfering with their normal schedules. Recorded thermal scans could then be sent to UNT for subsequent analyses.

The results of the current and future projects will substantially benefit law enforcement agencies. The improved ability to thermally discriminate clandestine graves from an airborne perspective would be time-saving and greatly decrease the manpower required for more conventional ground searches. Development of the image analysis and classification techniques may in time help produce new predictive models for determining time of deposition and depth of potential burials. Improved accuracy in signature recognition will increase the likelihood of obtaining a search warrant for suspect premises by strengthening probable cause. Unmanned drones could be equipped with thermal imagers and piloted into environments where suspected clandestine and/or mass burials are associated with human rights violations (e.g.

Bosnia, Afghanistan, etc.). Additional benefits would include reduced risks to ground search personnel in hostile contexts.

APPENDIX A

SOIL DESCRIPTIONS

The strata comprising Justin fine sandy loam soils are as follows (per the soil manual):

- Ap: 0 to13 centimeters (0 to 5 inches). Dark brown, moist, fine sandy loam. Slightly acidic, with abrupt, smooth boundary observed between Ap and A1

- A1: 13 to 31 centimeters (5-12 inches). Dark brown sandy loam. Slightly acidic, with a clear wavy boundary between A1 and B21t

- B21t: 31 to 43 centimeters (12-17 inches). Red/brown moist sandy loam with fine red mottles, with the potential for iron oxide deposits

- B22t: 43 to 84 centimeters (17-33 inches). Moist red/yellow clay loam, with some red mottles and a gradual, smooth boundary

- B23t: 84 to 203 centimeters (33-80 inches). Moist brown/yellow clay with yellow/red mottles, and soft masses of calcium carbonate in the lower levels

Soil observed during excavation of all units, including those from the 2006 study, were consistent with the descriptions above. Iron oxide deposits were noted in all units that were 0.5 meters in depth or greater, with larger deposits observed in Set A and the Preliminary Set. A calcium carbonate layer was located in the bases of units C and I (1.5 meter units); no calcium carbonate was noted in unit O (1.5 meter unit of Set B).

APPENDIX B

WEATHER CONDITIONS RECORDED AT STATION 03391 (NOAA), RENTON REGIONAL AIRPORT

Table B1. NOAA reported weather conditions per flight. Records were selected based on the closest recording to the reported time over the research site.

Date	Time	Temperature (°F)	Temperature (°C)	Dew Point (°C)	Humidity (%)
4/30/2006	53	55	12.8	9.4	80
8/28/2008	2353	80	26.7	20.6	69
11/21/2008	2353	36	2.2	-5	59
9/1/2009	2353	75	23.9	16.1	62
9/2/2009	2353	75	23.9	17.8	69
10/20/2009	2353	69	20.6	15.6	73
2/27/2010	2353	39	3.9	0	76

APPENDIX C

WEATHER DATA BY SURVEY (TABLES C1-C6) AS REPORTED BY NOAA FOR THE FLIGHT DATE (“*”), THE PRECEDEING WEEK, AND DATE FOLLOWING A FLIGHT. DATA WERE COLLECTED FROM STATION 03391 (NOAA) AT THE DENTON REGIONAL AIRPORT. PREPORTED ARE THE MAXIMUM (T_{max}), MINIMUM (T_{min}) AND AVERAGE (T_{avg}) TEMPERATURE, AS WELL AS DEW POINT, IN DEGREES CELCIUS (°C). HUMIDITY IS EXPRESSED AS A PERCENTAGE. PRECIPITATION (Precip) IS IN CENTIMETERS. “T” DENOTES TRACE PRECIPITATION

Table C1. Weather data for the Preliminary flight week.

Date	T_{max}	T_{min}	T_{avg}	Humidity	Dew Point	Precip
4/22/2006	28.9	13.9	21.7	50.9	13.9	0
4/23/2006	30.6	18.3	24.4	37.2	16.1	0
4/24/2006	28.9	20.6	25.0	53.9	18.9	0
4/25/2006	24.4	12.2	18.3	77.8	10.6	0
4/26/2006	21.7	10.0	16.1	51.1	7.8	0
4/27/2006	26.1	7.8	17.2	42.5	8.9	0
4/28/2006	22.8	17.8	20.6	37.9	16.1	3.86
*4/29/2006	21.7	13.9	17.8	80.2	13.9	0.20
4/30/2006	28.3	11.1	20.0	50.5	9.4	0

Table C2. Weather data for the week of Flight 1.

Date	T_{max}	T_{min}	T_{avg}	Humidity	Dew Point	Precip
8/21/2008	32.8	20.6	26.7	75.5	20.0	0.41
8/22/2008	35.6	24.4	30.0	68.4	21.7	0.05
8/23/2008	35.6	22.8	29.4	60.9	20.6	0
8/24/2008	34.4	21.1	27.8	67.4	20.0	0
8/25/2008	33.3	22.2	27.8	65.8	20.6	T
8/26/2008	34.4	21.1	27.8	64	20.0	0
8/27/2008	35.6	23.9	30.0	62.6	20.6	T
*8/28/2008	35.6	23.3	29.4	61.5	20.0	0
8/29/2008	35.6	22.8	29.4	65	21.1	0

Table C3. Weather data for the week of Flight 2.

Date	T_{max}	T_{min}	T_{avg}	Humidity	Dew Point	Precip
11/14/2008	22.8	9.4	15.9	64.9	9.9	0.03
11/15/2008	11.7	-1.1	6.6	46.4	-4.8	0
11/16/2008	21.1	-1.7	9.1	49.4	-3.1	0
11/17/2008	25.6	2.2	13.6	45.4	-0.3	0
11/18/2008	15.6	4.4	9.3	52.1	0.4	0
11/19/2008	25.6	3.9	13.7	36.7	2.6	0
11/20/2008	14.4	3.3	9.3	55.3	0.02	0
*11/21/2008	7.8	-1.7	3.4	47	-7.8	T
11/22/2008	13.3	1.1	7.7	54.9	-1.1	0

Table C4. Weather data for the week of Flights 3 and 4.

Date	T_{max}	T_{min}	T_{avg}	Humidity	Dew Point	Precip
8/25/2009	38.9	23.9	31	55.6	19.9	0
8/26/2009	36.7	23.9	30.3	57.5	20.5	0
8/27/2009	31.7	21.7	24.9	77.6	20.4	0.61
8/28/2009	31.7	19.4	25.3	69.1	18.1	0.03
8/29/2009	31.7	16.1	24.1	63.8	15.8	0
8/30/2009	30.6	17.8	24.1	60.4	15.1	0
8/31/2009	30	17.2	24	58.5	14.65	0
*9/1/2009	31.7	18.9	25.6	56.8	15.9	0
*9/2/2009	33.9	21.7	27	54.7	16.8	0
9/3/2009	32.2	20.6	26.2	67.2	19.1	0.51

Table C5. Weather data for the week of Flight 5.

Date	T_{max}	T_{min}	T_{avg}	Humidity	Dew Point	Precip
10/13/2009	19.4	16.7	17.8	98.1	17.5	3.40
10/14/2009	28	19	22.2	94.4	21.2	0.03
10/15/2009	23.9	11	16.7	86.7	14.3	0
10/16/2009	20.6	10	13.9	75.3	9.2	0
10/17/2009	23.3	7.8	14.9	69.3	8.4	0
10/18/2009	21.1	5.6	13.8	74.7	9	0
10/19/2009	24.4	12.2	18.2	71.9	12.8	0
*10/20/2009	26.1	15	20.6	67.3	14	0
10/27/2009	20	15	18	96.4	17.4	7.11

Table C6. Weather data for the week of Flight 6.

Date	T_{max}	T_{min}	T_{avg}	Humidity	Dew Point	Precip
2/20/2010	16.1	11	13.1	86	10.7	T
2/21/2010	15	3.3	10.7	89.4	8.9	0.74
2/22/2010	4	1.1	2.5	78.9	-0.8	0
2/23/2010	5	0	1.8	70	-3.4	0
2/24/2010	8.3	-2.8	2.2	60.7	-5.3	0
2/25/2010	12.8	0	7.5	55.4	-1.6	T
2/26/2010	9.4	0.6	5.5	86.3	3.4	T
*2/27/2010	17.8	-1	6.5	68.4	-0.6	0
2/28/2010	17.2	0.6	9.7	57.4	0.6	0

APPENDIX D

MONTHLY WEATHER DATA AVERAGES, JANUARY 2003 THROUGH MAY 2010. TABLES ARE ARRANGED BY YEAR (TABLES D1-D8). DATA WERE COLLECTED FROM STATION 03391 (NOAA) AT THE DENTON REGIONAL AIRPORT. REPORTED ARE THE MAXIMUM (T_{max}), MINIMUM (T_{min}) AND AVERAGE (T_{avg}) TEMPERATURES, AS WELL AS DEW POINT (°C). TOTAL PRECIPTIATION (Precip) IS IN CENTIMETERS. "*" DENOTES NO DATA

Table D1. Monthly weather averages near the site for January through May of 2010.

Month	T_{max}	T_{min}	T_{avg}	Dew Point	Precip
January	12.4	-0.6	6.1	-0.1	6.68
February	9.0	-0.2	4.5	-0.1	7.37
March	18.9	5.1	12.2	4.7	9.88
April	23.9	11.7	17.9	11.3	8.18
May	29.4	16.9	23.3	16.3	4.72

Table D2. 2009 monthly weather averages near the site.

Month	T_{max}	T_{min}	T_{avg}	Dew Point	Precip
January	15.1	-1.7	6.8	-3.6	1.78
February	19.4	4.4	12.1	1.8	3.68
March	20.5	7.8	14.3	6.0	6.68
April	24.2	10.0	15.6	7.3	9.75
May	27.6	15.5	21.7	16.3	15.14
June	33.6	21.4	27.6	19.7	6.38
July	35.7	22.5	29.2	19.4	6.48
August	35.8	23.2	29.6	19.9	2.57
September	29.2	17.6	23.5	17.3	9.17
October	21.4	10.4	16.0	11.9	32.05
November	21.1	6.9	14.2	8.3	1.32
December	11.0	-1.2	5.3	-0.6	4.19

Table D3. 2008 monthly weather averages near the site.

Month	T_{max}	T_{min}	T_{avg}	Dew Point	Precip
January	13.4	-1.4	6.2	-1.9	0.25
February	18.7	1.9	10.5	1.1	6.65
March	21.7	7.8	15.0	6.1	16.26
April	24.4	10.4	17.6	9.8	7.39
May	29.7	16.5	23.2	15.1	9.50
June	35.3	22.8	28.9	19.2	6.45
July	36.8	23.2	30.1	18.3	0.86
August	34.9	22.7	28.9	19.7	13.34
September	30.6	16.9	23.9	15.9	2.39
October	26.6	11.3	19.1	9.4	3.28
November	20.5	5.3	13.1	3.8	6.05
December	14.7	-0.8	7.1	-1.3	1.12

Table D4. 2007 monthly weather averages near the site.

Month	T_{max}	T_{min}	T_{avg}	Dew Point	Precip
January	9.7	0.1	4.9	-0.3	6.63
February	15.2	0.3	8.7	0.8	1.32
March	22.7	10.6	16.8	8.8	9.98
April	21.6	9.9	15.8	9.4	17.09
May	27.5	18.1	22.9	17.7	17.37
June	31.3	21.1	26.2	20.3	35.81
July	32.8	21.9	27.6	21.2	4.01
August	35.9	23.4	29.7	21.2	0.20
September	32.5	20.2	26.5	18.8	8.41
October	27.7	13.0	20.5	11.9	6.58
November	21.2	8.3	14.9	6.5	3.48
December	14.9	0.7	7.9	1.2	3.89

Table D5. 2006 monthly weather averages near the site.

Month	T_{max}	T_{min}	T_{avg}	Dew Point	Precip
January	19.8	3.1	15.2	-1.8	4.85
February	15.4	1.7	8.7	-0.5	5.79
March	22.3	10.2	16.2	5.5	8.51
April	28.4	14.4	21.6	11.3	6.93
May	30.3	17.7	24.1	15.0	3.94
June	35.4	20.5	28.1	16.1	2.82
July	37.4	24.2	30.9	18.3	1.19
August	38.3	25.2	31.8	18.6	2.46
September	30.9	17.1	24.2	14.7	6.22
October	25.8	11.9	19.0	10.1	7.14
November	20.3	6.1	13.3	5.8	10.72
December	15.2	2.9	9.2	2.4	7.98

Table D6. 2005 monthly weather averages near the site.

Month	T_{max}	T_{min}	T_{avg}	Dew Point	Precip
January	15.1	3.0	9.2	3.0	8.79
February	16.5	5.2	10.9	4.4	3.99
March	19.7	6.2	13.1	4.2	6.25
April	*	*	*	*	*
May	28.1	16.7	22.6	14.8	6.22
June	34.1	21.5	27.9	18.4	2.69
July	35.0	22.2	28.7	19.4	3.43
August	36.1	22.9	29.6	19.4	4.22
September	35.3	20.1	27.8	15.8	0.76
October	27.2	11.8	19.6	9.4	1.57
November	22.8	6.4	14.7	3.5	0.10
December	15.2	-0.2	7.7	-3.4	0.05

Table D7. 2004 monthly weather averages near the site.

Month	T_{max}	T_{min}	T_{avg}	Dew Point	Precip
January	13.9	1.8	7.8	2.4	3.58
February	11.7	1.8	6.9	1.8	9.55
March	21.2	8.9	15.2	8.7	4.09
April	23.6	12.1	18.2	12.4	14.53
May	28.5	17.4	23.4	17.1	9.19
June	31.0	20.6	26.0	20.8	28.96
July	33.4	21.2	27.8	20.4	8.99
August	31.9	20.7	26.6	19.1	10.39
September	31.3	17.4	24.6	16.3	3.84
October	27.2	15.1	21.4	14.9	18.36
November	17.6	8.3	13.1	8.9	17.07
December	14.9	1.5	8.6	0.7	1.88

Table D8. 2003 monthly weather averages near the site.

Month	T_{max}	T_{min}	T_{avg}	Dew Point	Precip
January	12.3	-1.1	5.8	-0.4	0.46
February	12.0	1.3	6.9	2.6	7.87
March	19.3	5.7	12.8	6.6	1.85
April	25.7	11.1	18.8	11.2	3.25
May	29.3	17.0	23.4	17.6	12.14
June	31.5	19.1	25.4	19.4	8.86
July	36.3	22.9	29.8	20.3	2.46
August	36.3	22.9	29.8	20.1	3.05
September	28.9	17.0	23.1	16.3	11.15
October	27.4	11.6	20.0	11.9	0.61
November	19.3	8.5	14.3	7.6	7.95
December	15.4	1.0	8.2	0.3	1.91

APPENDIX E

STATISTICAL COMPARISONS BETWEEN TWO IMAGER POLARITIES, “WHITE HOT” VS. “BLACK HOT”

Table E1. Sample size (*n*), Shapiro-Wilks normality results and five number summaries for samples extracted (Unit ID) from Images 6r7 (white hot) and 6r10 (black hot). "*" denotes a normal distribution.

	Unit ID	*n*	S-W *W*	*P*	Five Number Summaries
6r7 (White Hot)	J	62	0.874	<0.0001	120, 113, 105, 95, 53
	K	64	0.9655	=0.0701*	112, 101, 81.5, 69, 40
	L	63	0.9429	=0.0056	48, 38, 26, 18, 10
	M	65	0.979	=0.3337*	96, 75, 56, 43, 11
	N	62	0.8382	<0.0001	124, 118, 111.5, 96, 55
	T	64	0.9563	=0.0237	19, 13, 10, 7, 4
6r10 (Black Hot)	J	62	0.7932	<0.0001	46, 14, 7, 4, 1
	K	64	0.9561	=0.0231	50, 37, 25, 13.5, 4
	L	63	0.972	=0.1606*	73, 66, 62, 56, 48
	M	65	0.9805	=0.3940*	65, 48, 42, 30, 16
	N	62	0.8284	<0.0001	46, 18, 7, 4, 0
	T	64	0.9414	=0.0044	79, 73, 70, 68.5, 55

Table E2. Sample collections from each image were highly significantly different (Kruskall-Wallis one way analysis of variance on ranked data). Samples separated into statistically distinct groups (SNK on ranked data, α=0.05), although the order are inversed. Likewise, the association between signature and depth (Spearman's correlation) is a near-perfect inverse.

	K-W *H*	DF	*P*	SNK Grouping	r_s	*P*
6r7	314.56	5	< 0.0001	N(1) = J(1) > K(0.5) > M(0.5) > L(0.25) > T(0)	0.8912	< 0.0001
6r10	314.77	5	< 0.0001	T(0) > L(0.25) > M(0.5) > K(0.5) > N(1) = J(1)	-0.8835	< 0.0001

APPENDIX F

STATISTICAL COMPARISONS BETWEEN THE THREE BANDS OF AN RBG COMPOSITE THERMAL IMAGE. MULTIPLE SAMPLES CONSISTING OF DISTURBED UNITS AND CONTROLS WERE EXTRACTED AND ANALYZED AND ARE PRESENTED

Table F1. Sample size (*n*), Shapiro-Wilks normality (SW-*W*) and five number summaries by band for each extracted sample (Unit ID) from Image 1r6. Although the descriptive statistics differed by band, the *W* statistic and associated probability are the same for a given sample.

Unit ID	*n*	SW-*W*	*P*	Band 1 (Red)	Band 2 (Green)	Band 3 (Blue)
B	492	0.934	<0.0001	107,100, 97, 92, 66	109, 102, 99, 94, 68	106, 99, 96, 91, 65
D	490	0.9316	<0.0001	82, 77, 75, 72, 57	84, 79, 77, 74, 59	81, 76, 74, 71, 56
E	491	0.9883	=0.0006	73, 59, 54, 49, 37	75, 61, 56, 51, 39	72, 58, 53, 48, 36
F	492	0.9923	=0.0123	59, 50, 47, 43, 34	61, 52, 49, 45, 36	58, 49, 46, 42, 33
G	489	0.9881	=0.0005	57, 48, 46, 44, 37	59, 50, 48, 46, 39	56, 47, 45, 43, 36
H	493	0.976	<0.0001	69, 63, 59, 55, 43	71, 95, 91, 57, 45	68, 62, 58, 54, 42
I	492	0.9861	<0.0001	73, 65, 63, 61, 54	75, 67, 65, 63, 56	72, 64, 62, 60, 53
P	492	0.9747	<0.0001	39, 32, 28, 26, 20	41, 34, 30, 28, 22	38, 31, 27, 25, 19
Q	492	0.9319	<0.0001	52, 33, 26, 22, 17	54, 35, 28, 24, 19	51, 32, 25, 21, 16
R	492	0.9868	<0.0001	67, 57, 48, 38, 20	69, 59, 50, 40, 22	66, 56, 47, 37, 19
S	492	0.9029	<0.0001	46, 32.5, 26, 23, 20	48, 34.5, 28, 25, 22	45, 31.5, 25, 22, 19

Table F2. Sample collections from each band were highly significantly different (Kruskall-Wallis one way analysis of variance on ranked data) with the same resulting Chi-square value for each band. Statistical separation into distinct groups (SNK on ranked data, α=0.05) was likewise the same, demonstrating that the band display redundant information.

Image 1r6	K-W *H*	DF	*P*	SNK Grouping
Band 1	4764.91	10	<0.0001	B > D > I > H > E > R > F > G > P > Q = S
Band 2	4764.91	10	<0.0001	B > D > I > H > E > R > F > G > P > Q = S
Band 3	4764.61	10	<0.0001	B > D > I > H > E > R > F > G > P > Q = S

APPENDIX G

FLOW CHART OF EXPERIMENTAL PROCEDURES (FIGURES G1-G3)

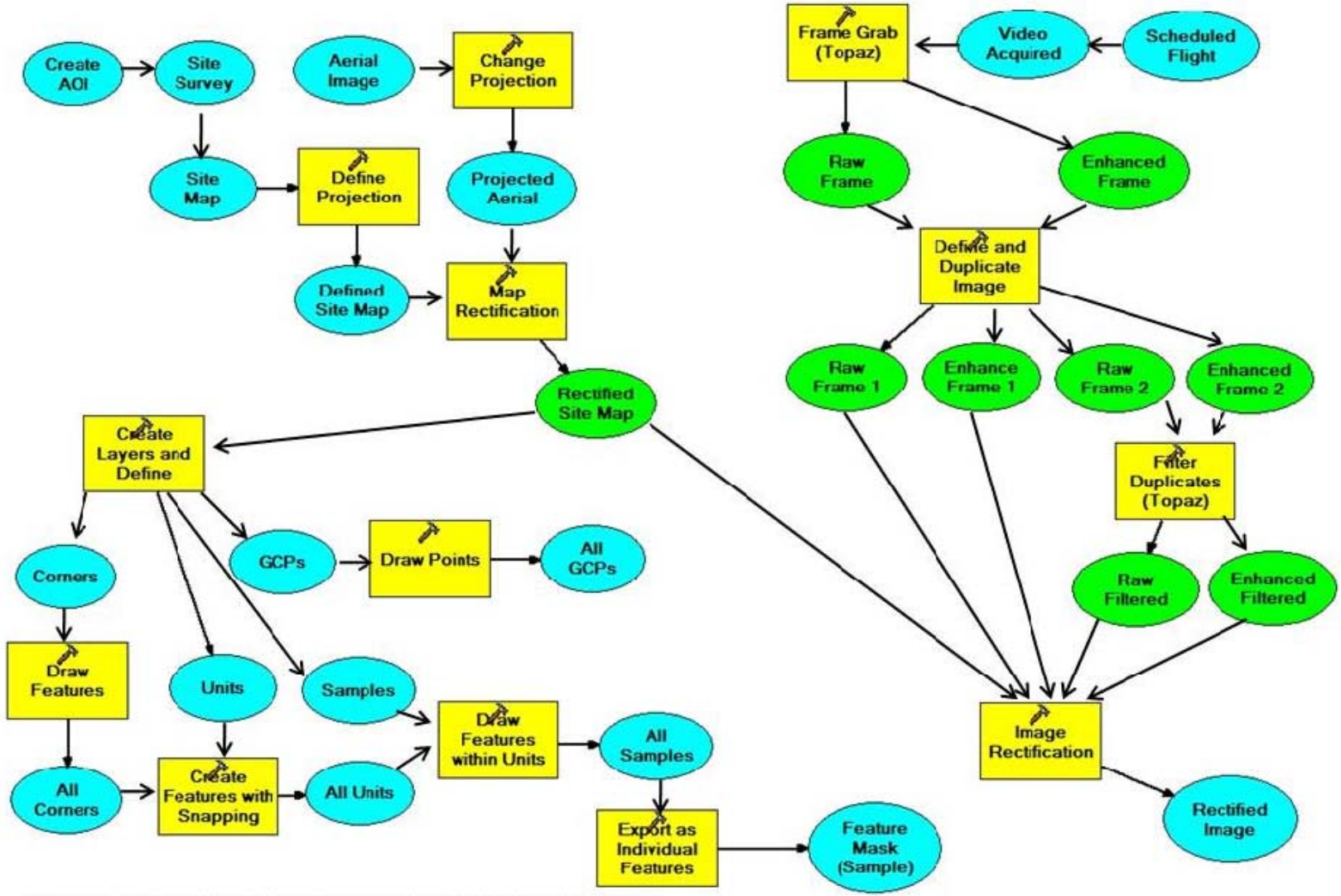

Figure G1. Statistical analysis process: layer and image preparation.

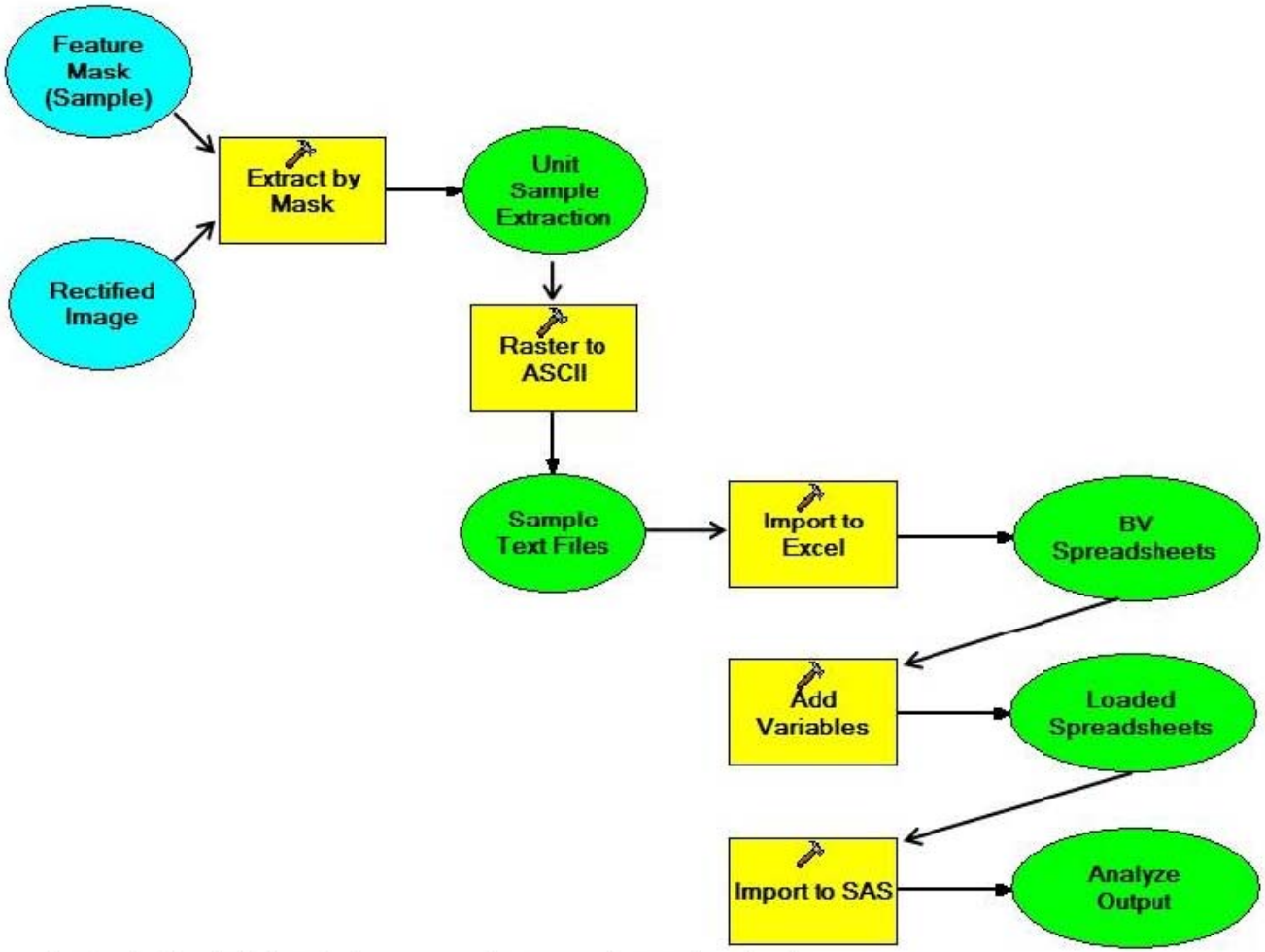

Figure G2. Statistical analysis process: data extraction and analysis.

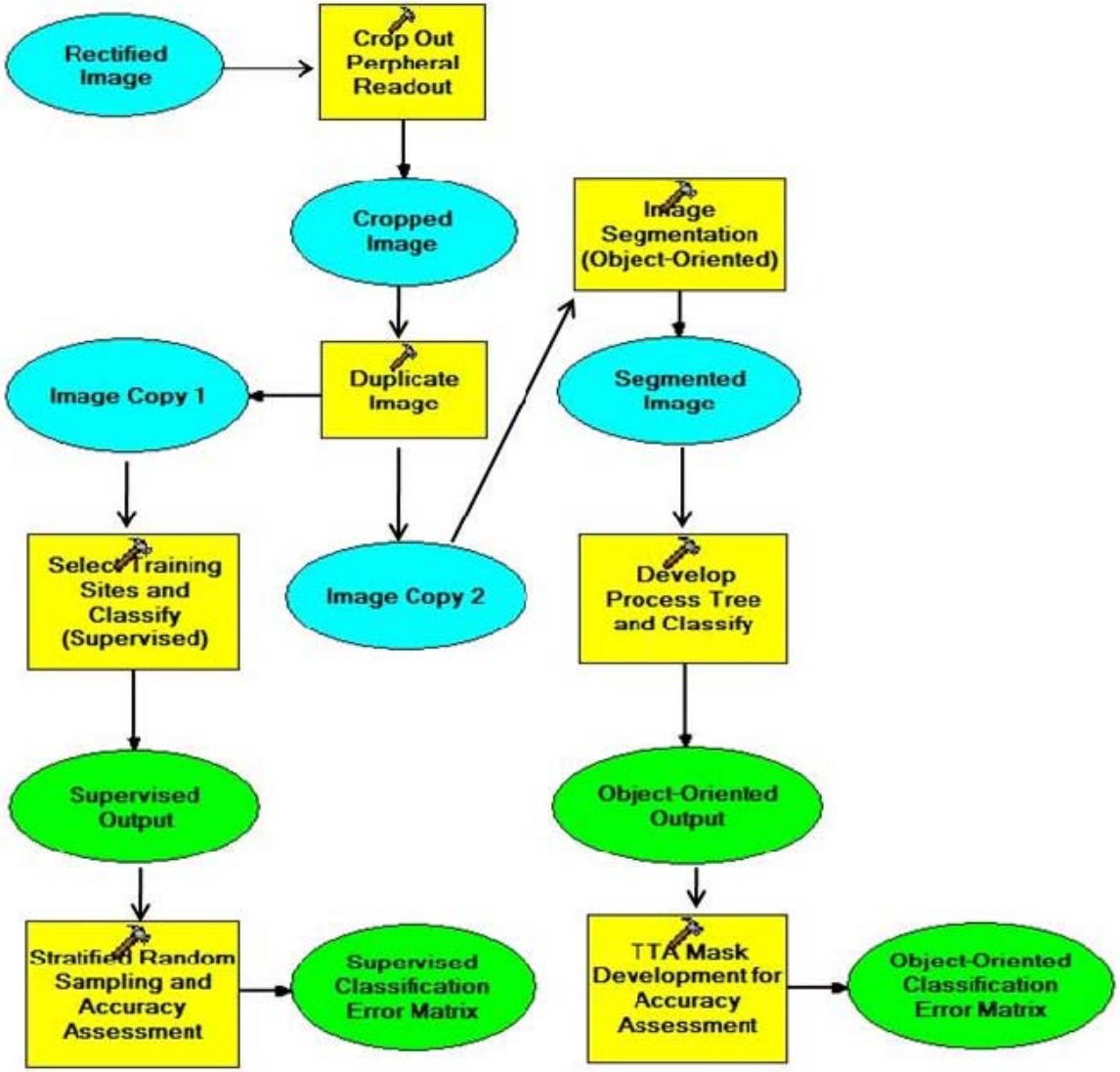

Figure G3. Classification study process.

APPENDIX H

RECTIFICATION DATA PRESENTED BY IMAGE, INCLUDING THE FINAL RMS_{error} , NUMBER OF ESTABLISHED LINKS, FINAL CELL SIZE, AND THE NUMBER OF DISTURBED AND CONTROL SAMPLES EXTRACTED

Table H1. Associated rectification information for each image, including RMSerror, the number of links, output cell size for rectified images, and the number of extracted samples.

				Samples	
Image	RMS_{error}	Links	Cell Size	Units	Controls
1r22	0.3345	15	0.16	10	10
1r22f	0.3055	15	0.16	10	10
1e22	0.3638	15	0.07	10	10
1e22f	0.3154	15	0.07	9	10
1r23	0.1974	13	0.05	6	2
1r23f	0.2058	12	0.05	4	2
1e23	0.2087	13	0.02	4	2
1e23f	0.2284	13	0.02	4	2
`4r22	0.3532	15	0.11	6	5
4r22f	0.2954	15	0.11	5	5
4e22	0.3099	15	0.04	5	5
4e22f	0.2621	15	0.04	5	5
4r25	0.3083	20	0.1	6	7
4r25f	0.339	18	0.1	6	7
4e25	0.3346	15	0.05	6	6
4e25f	0.2346	15	0.05	9	6
5r2	0.1505	10	0.04	6	1
5r2f	0.1586	9	0.04	6	1
5e2	0.1632	10	0.02	5	3
5e2f	0.1999	9	0.02	5	2
5r26	0.3166	15	0.15	11	10
5r26f	0.2698	12	0.15	10	10
5e26	0.2613	15	0.07	11	10
5e26f	0.2434	12	0.07	10	9
6r10	0.3565	20	0.14	10	8
6r10f	0.295	19	0.14	10	8
6e10	0.2549	20	0.07	10	8
6e10f	0.1987	17	0.07	10	7
6r11	0.3155	10	0.04	6	2
6r11f	0.2209	7	0.04	6	2
6e11	0.238	10	0.02	6	1
6e11f	0.2535	7	0.02	6	1

APPENDIX I

RECTIFIED IMAGES, BY SERIES (FIGURE I1-I25). COMPLETE SERIES 1_23, AS WELL AS IMAGES 4r25, 5r26, AND 6r11 ARE PRESENTED IN THE TEXT (CHAPTER 4) AND ARE NOT INCLUDED IN THIS APPENDIX

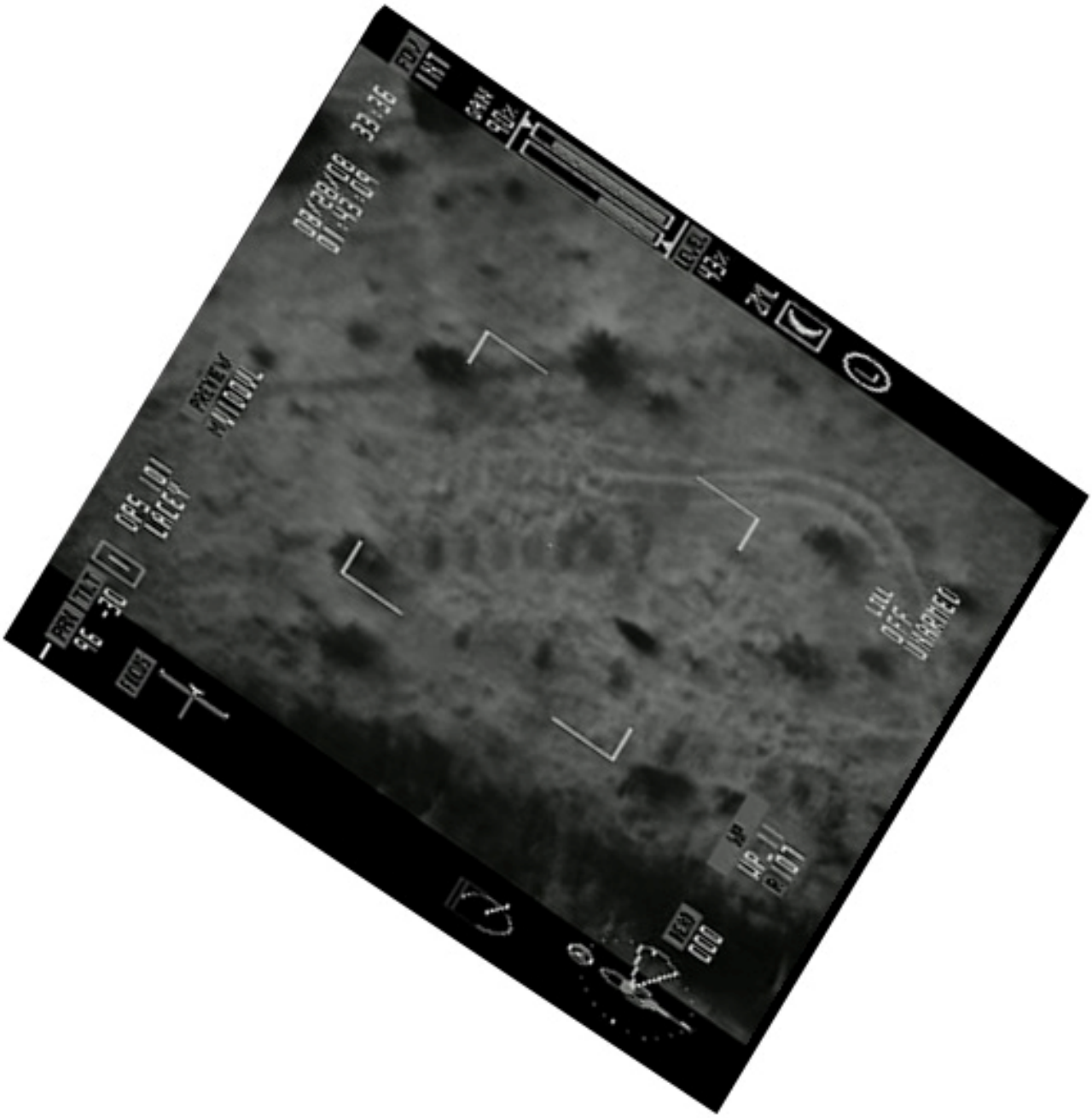

Figure I1. Rectified version of image 1r22.

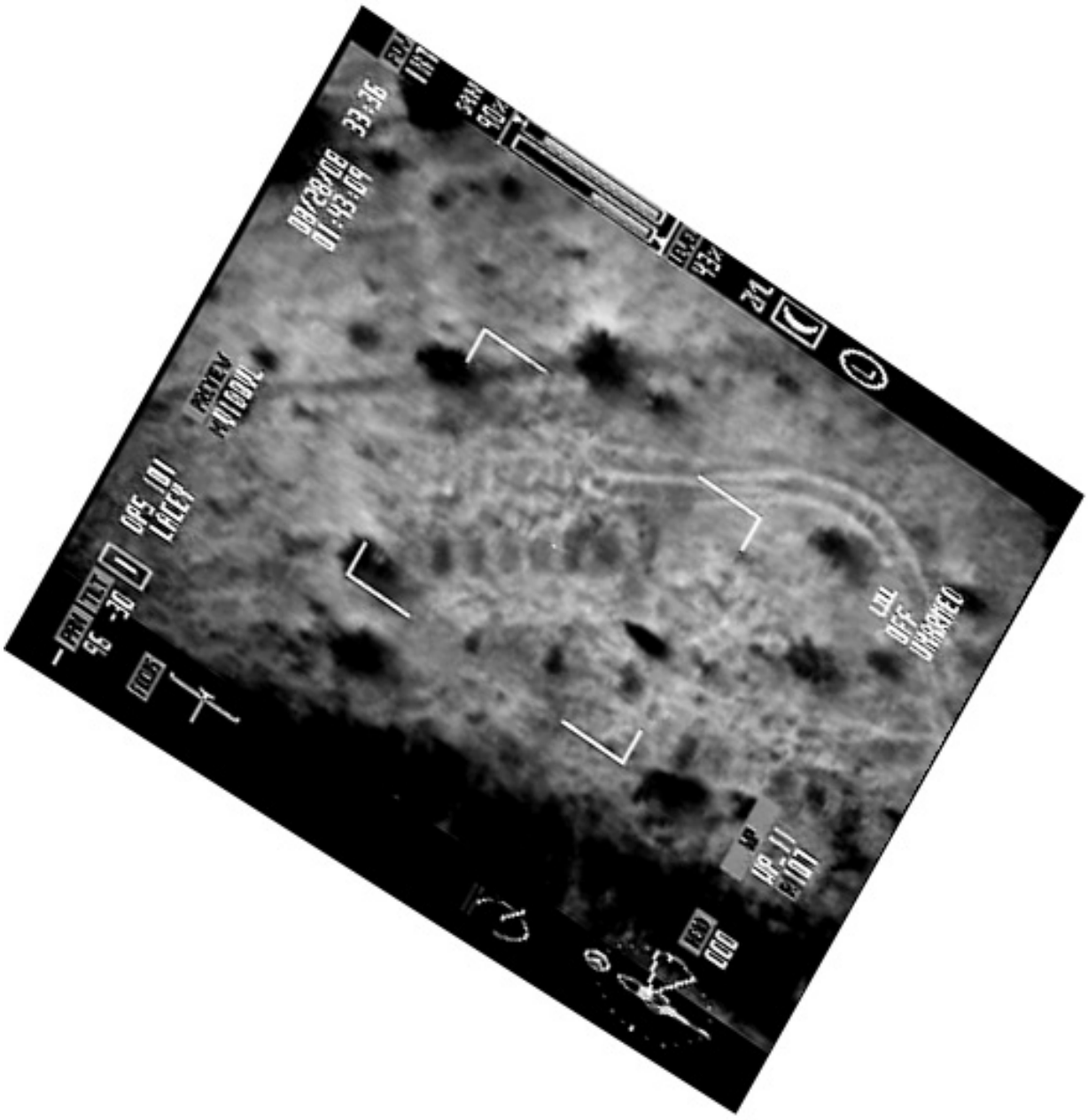

Figure I2. Rectified version of image 1r22f.

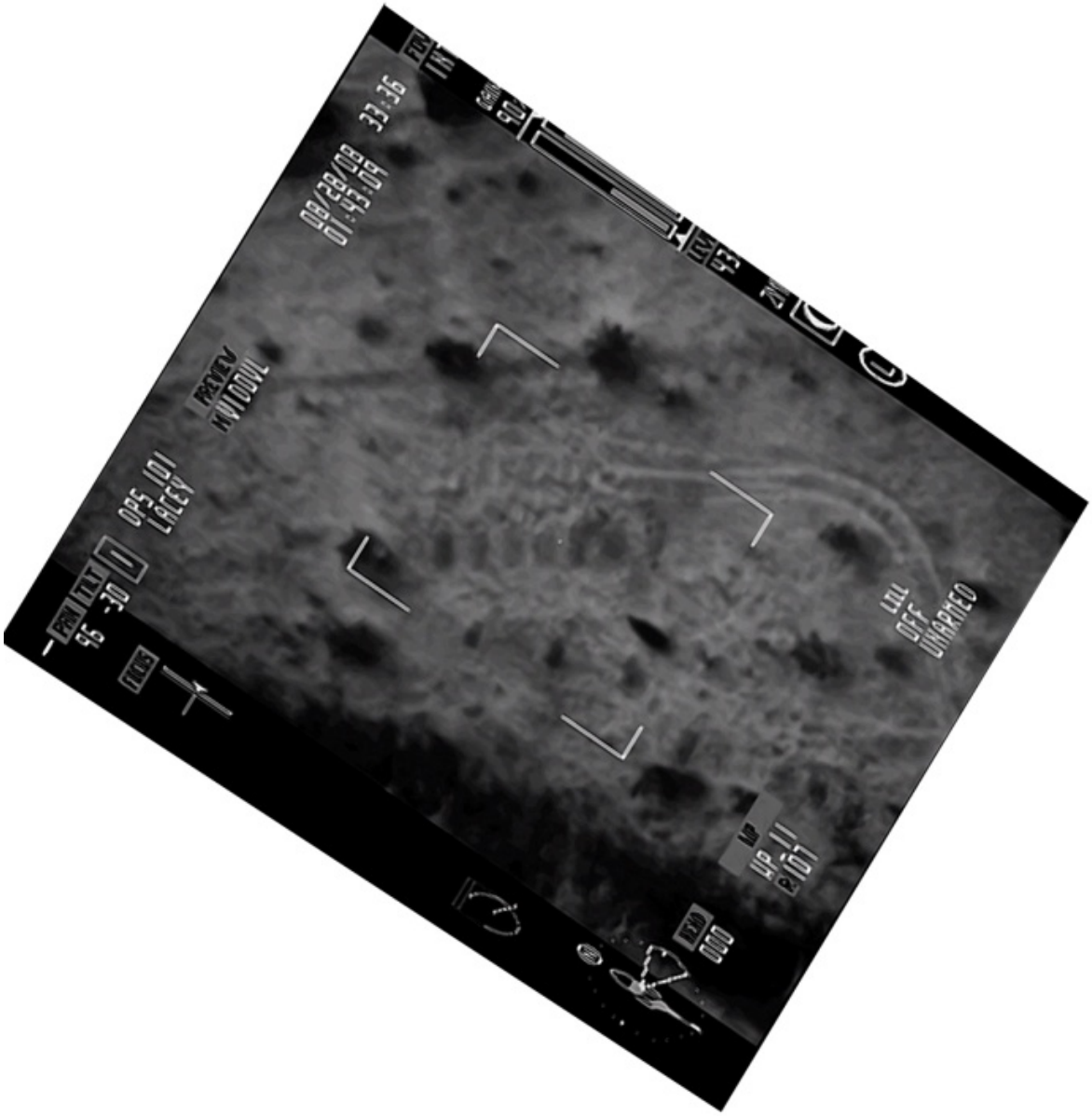

Figure I3. Rectified version of image 1e22.

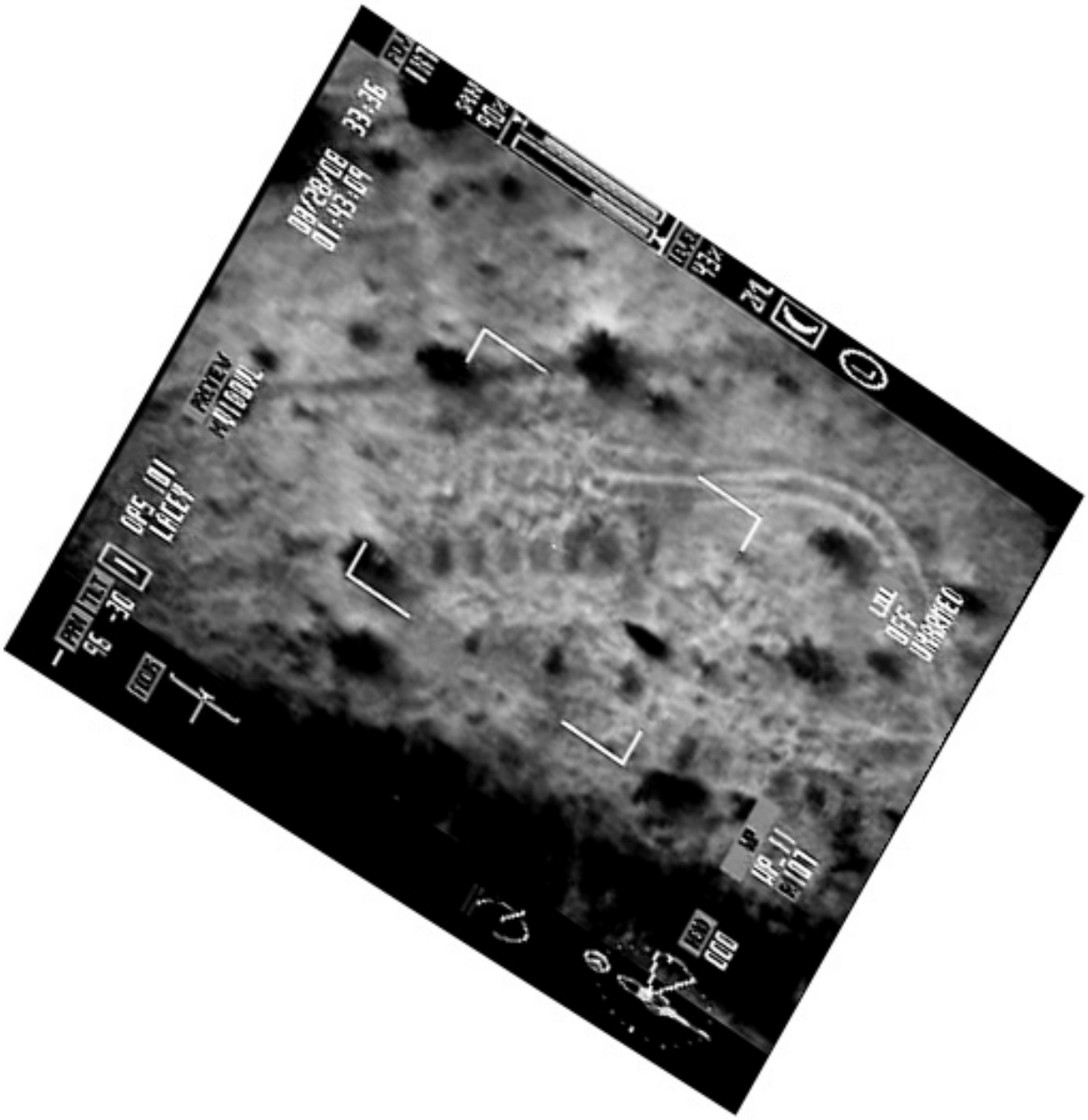

Figure I4. Rectified version of image 1e22f.

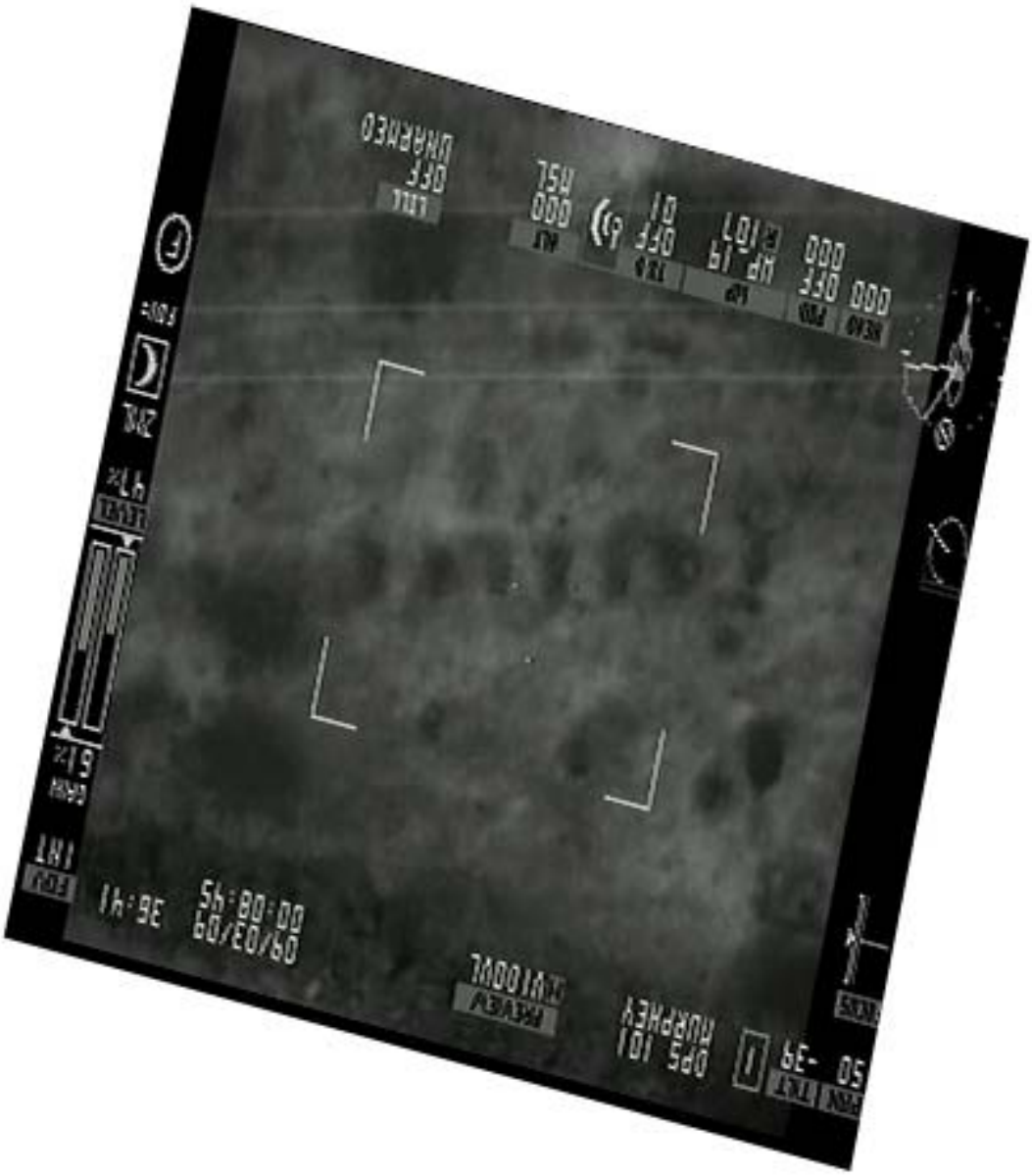

Figure I5. Rectified version of image 4r22.

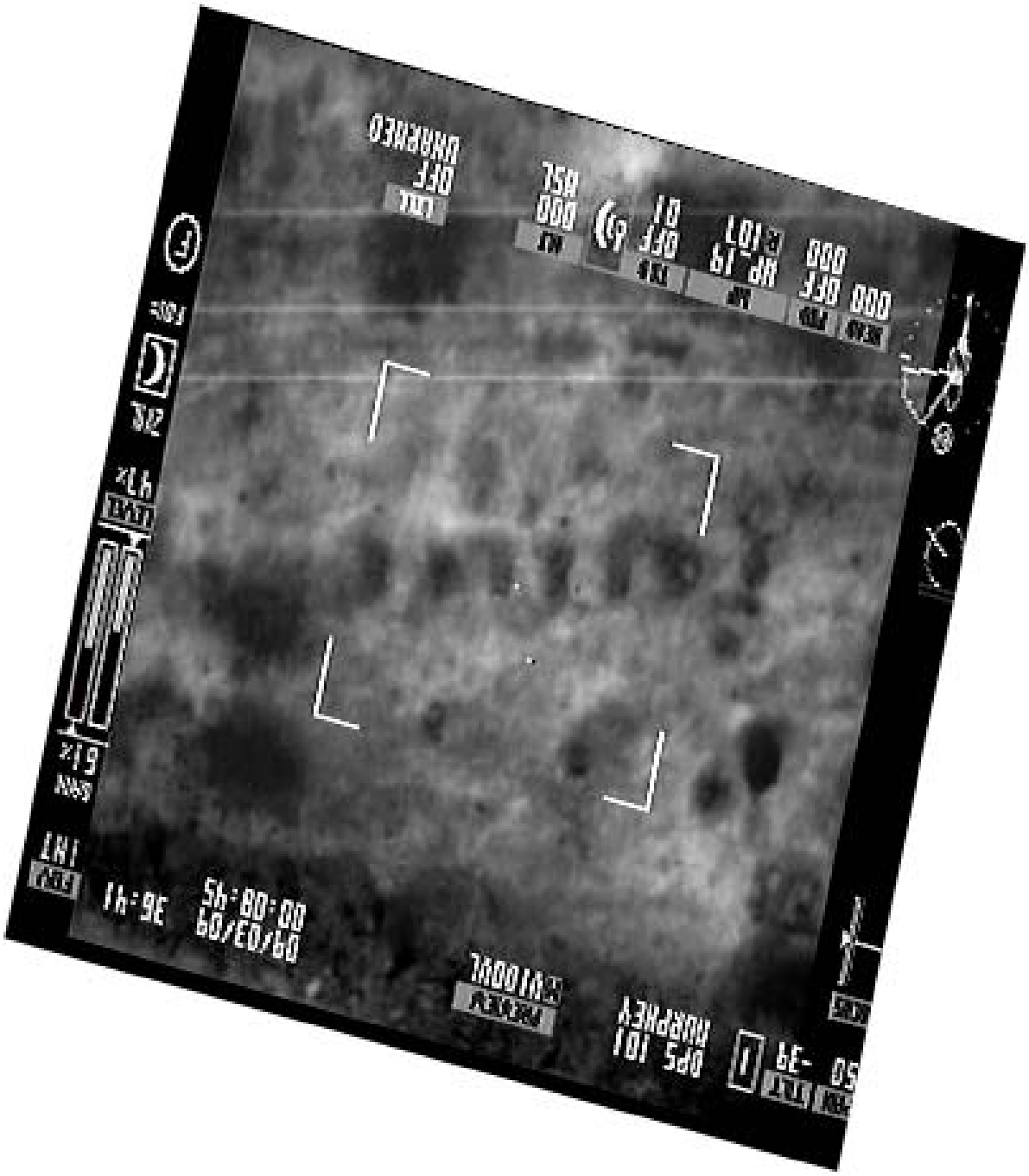

Figure I6. Rectified version of image 4r22f.

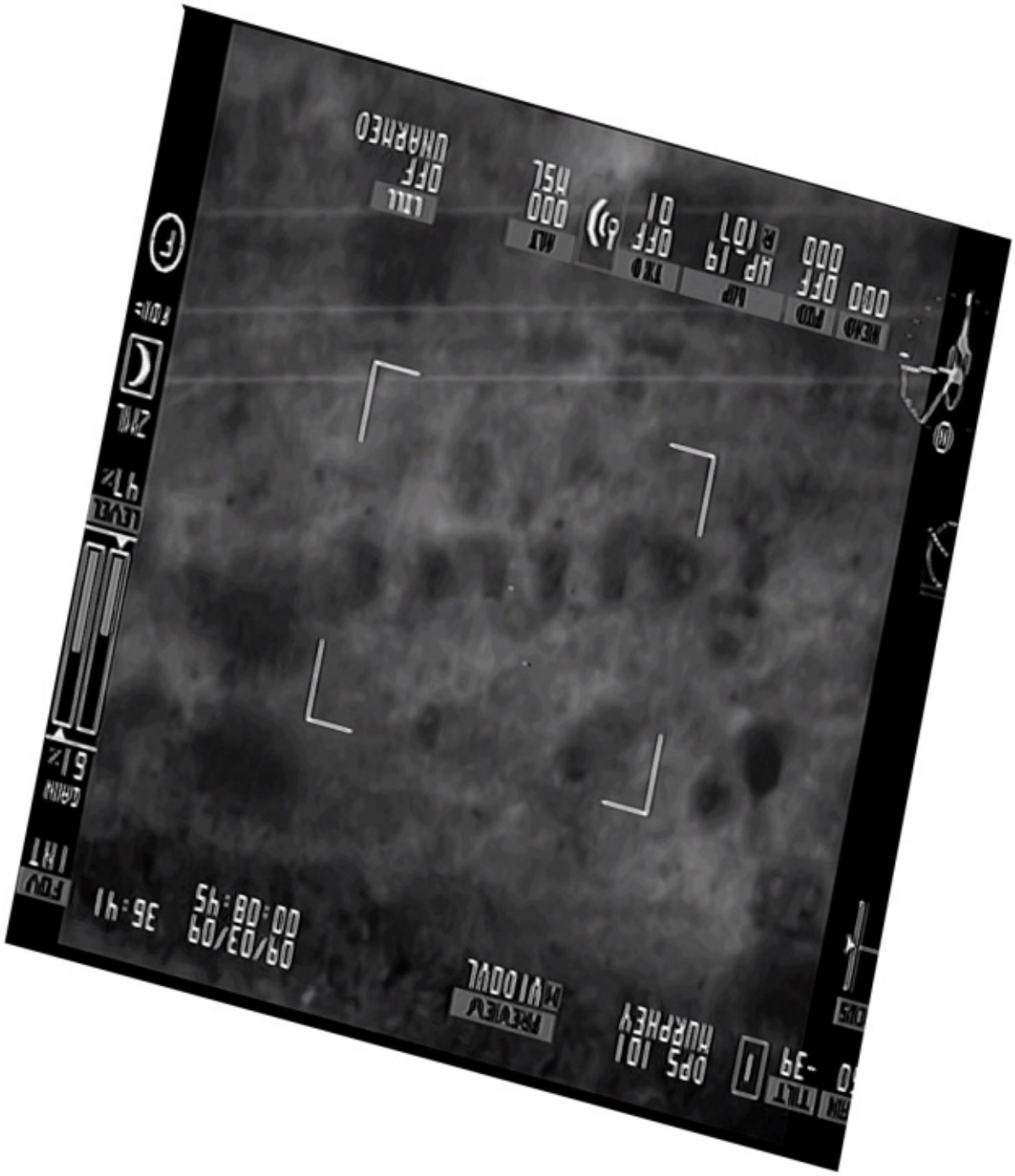

Figure I7. Rectified version of image 4e22.

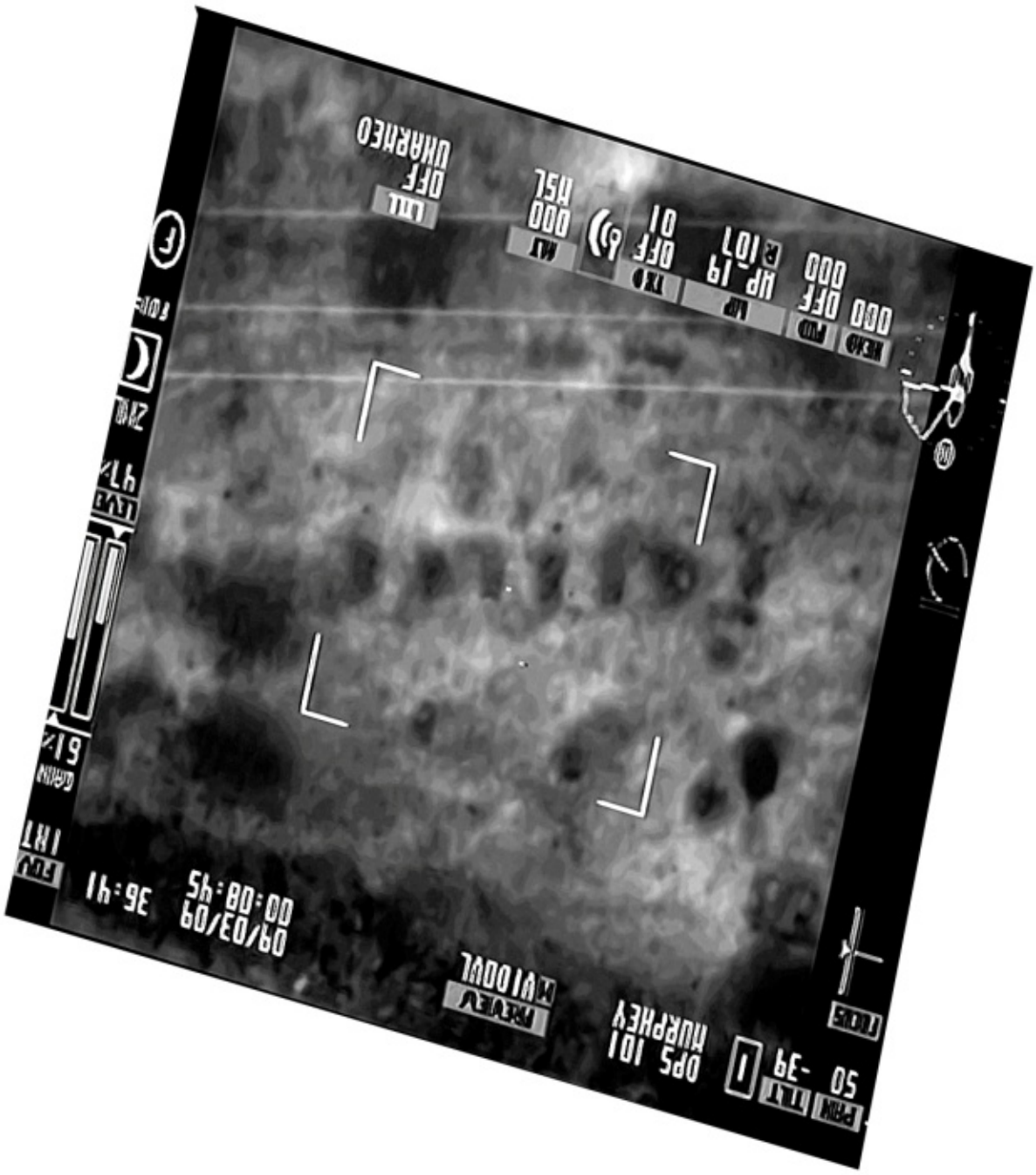

Figure I8. Rectified version of image 4e22f.

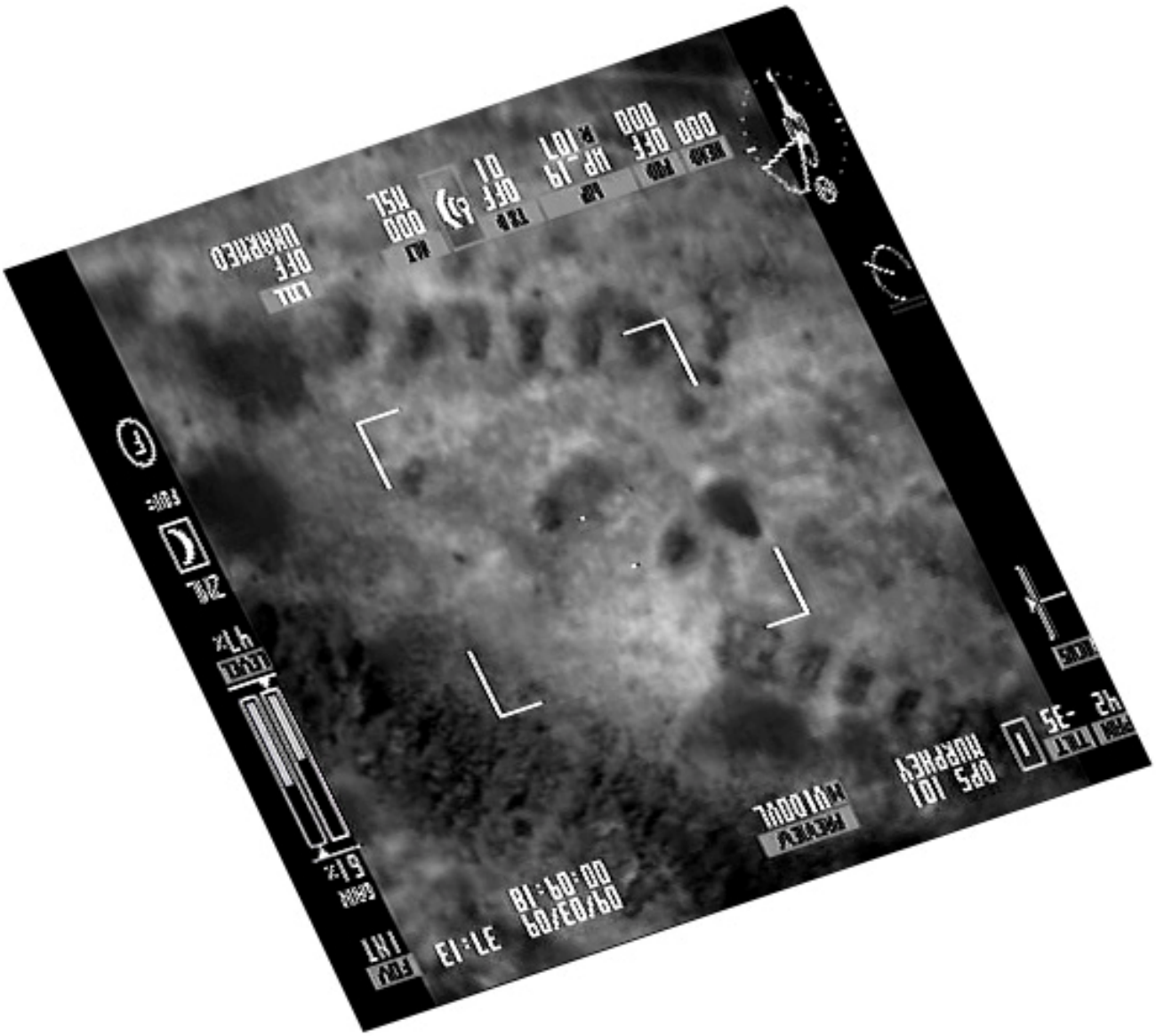

Figure I9. Rectified version of image 4r25f.

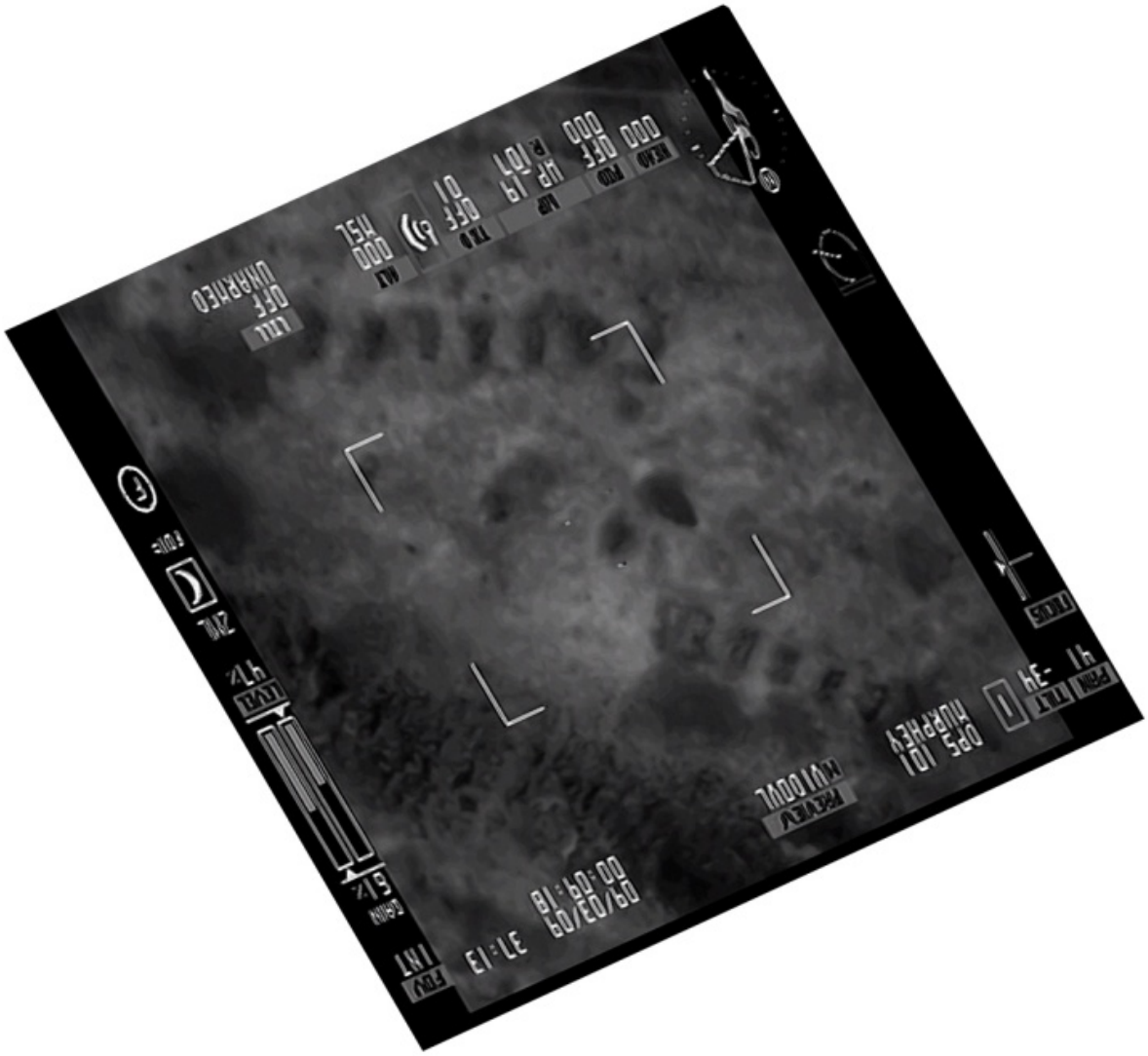

Figure I10. Rectified version of image 4e25.

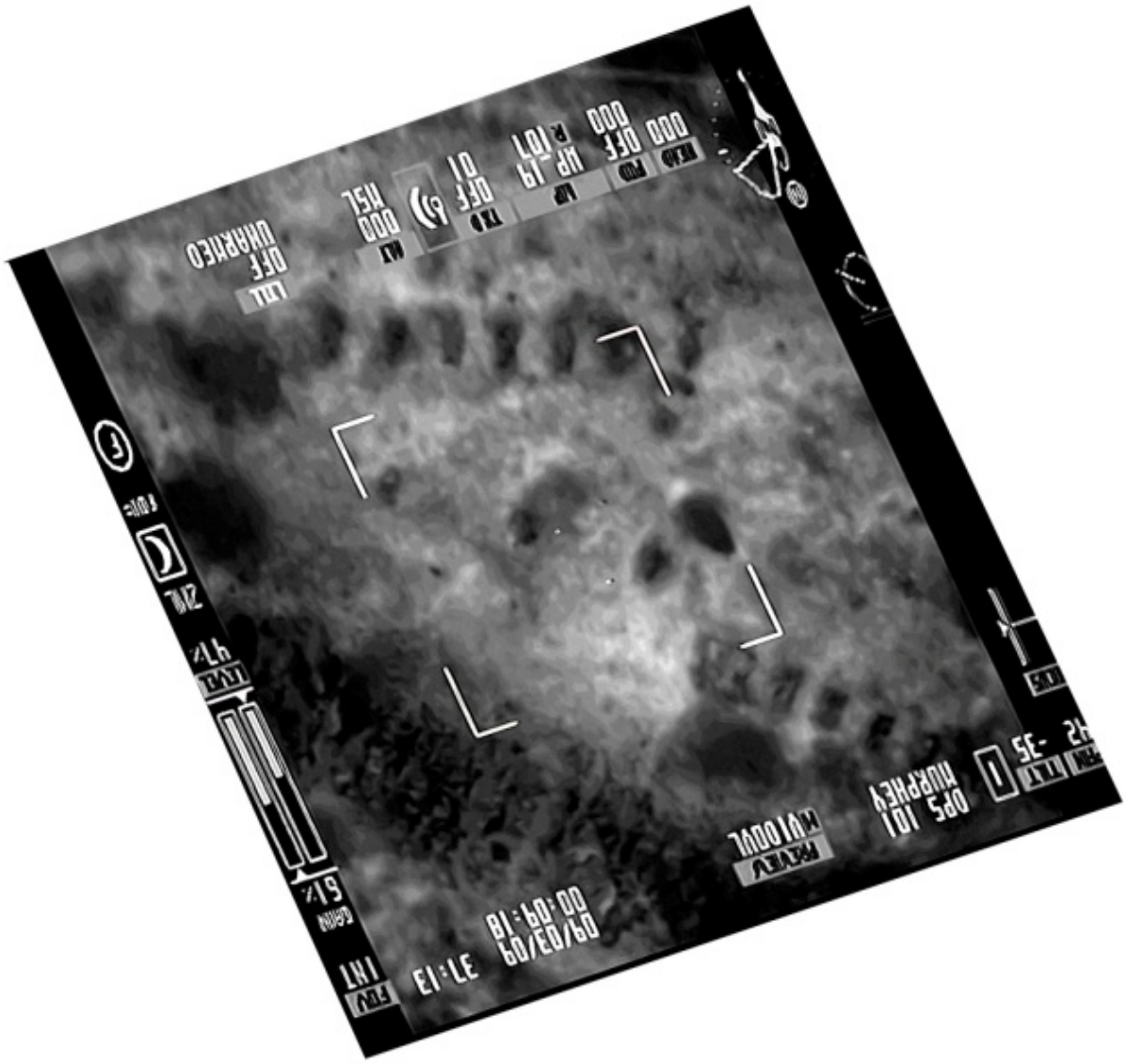

Figure I11. Rectified version of image 4e25f.

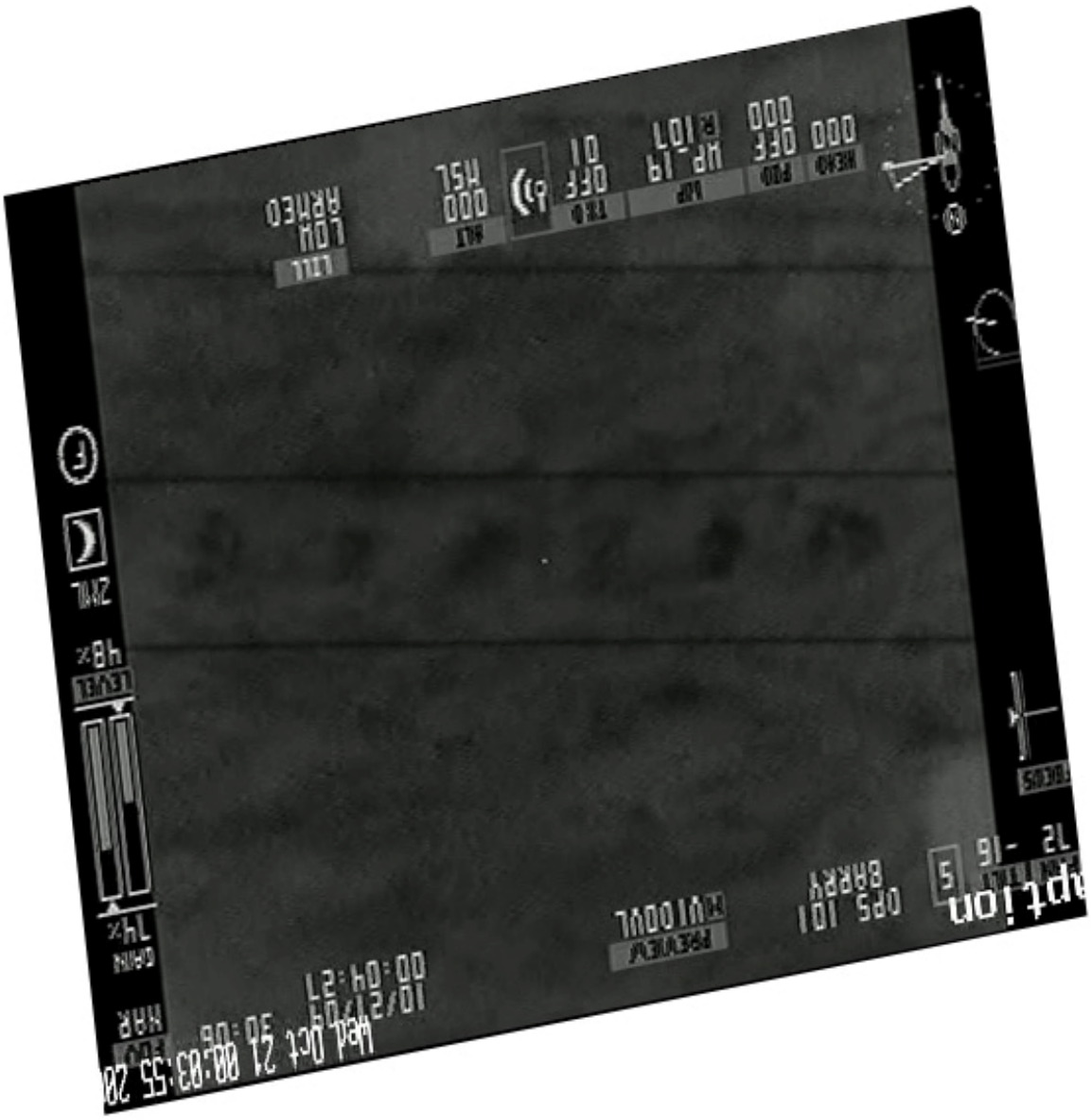

Figure I12. Rectified version of image 5r2.

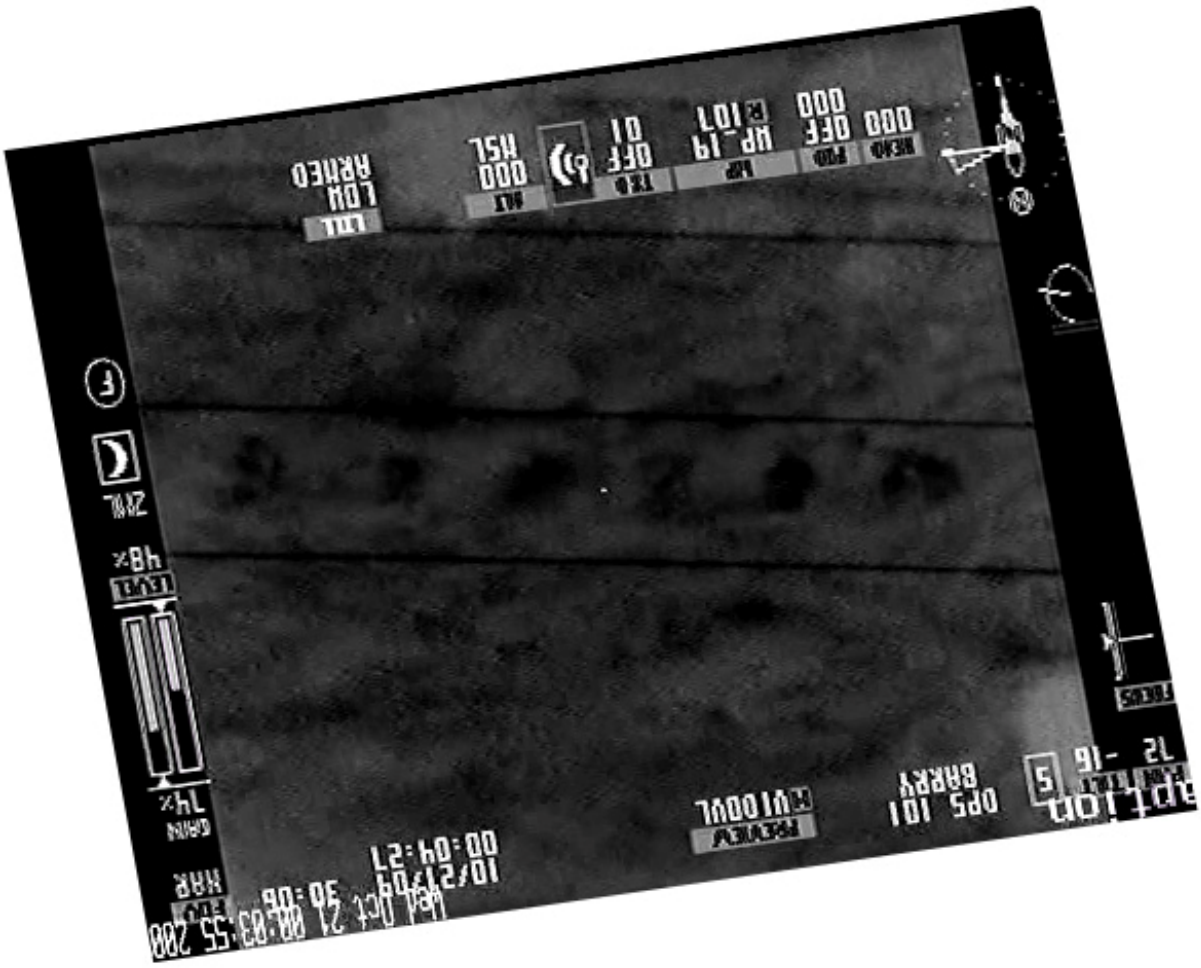

Figure I13. Rectified version of image 5r2f.

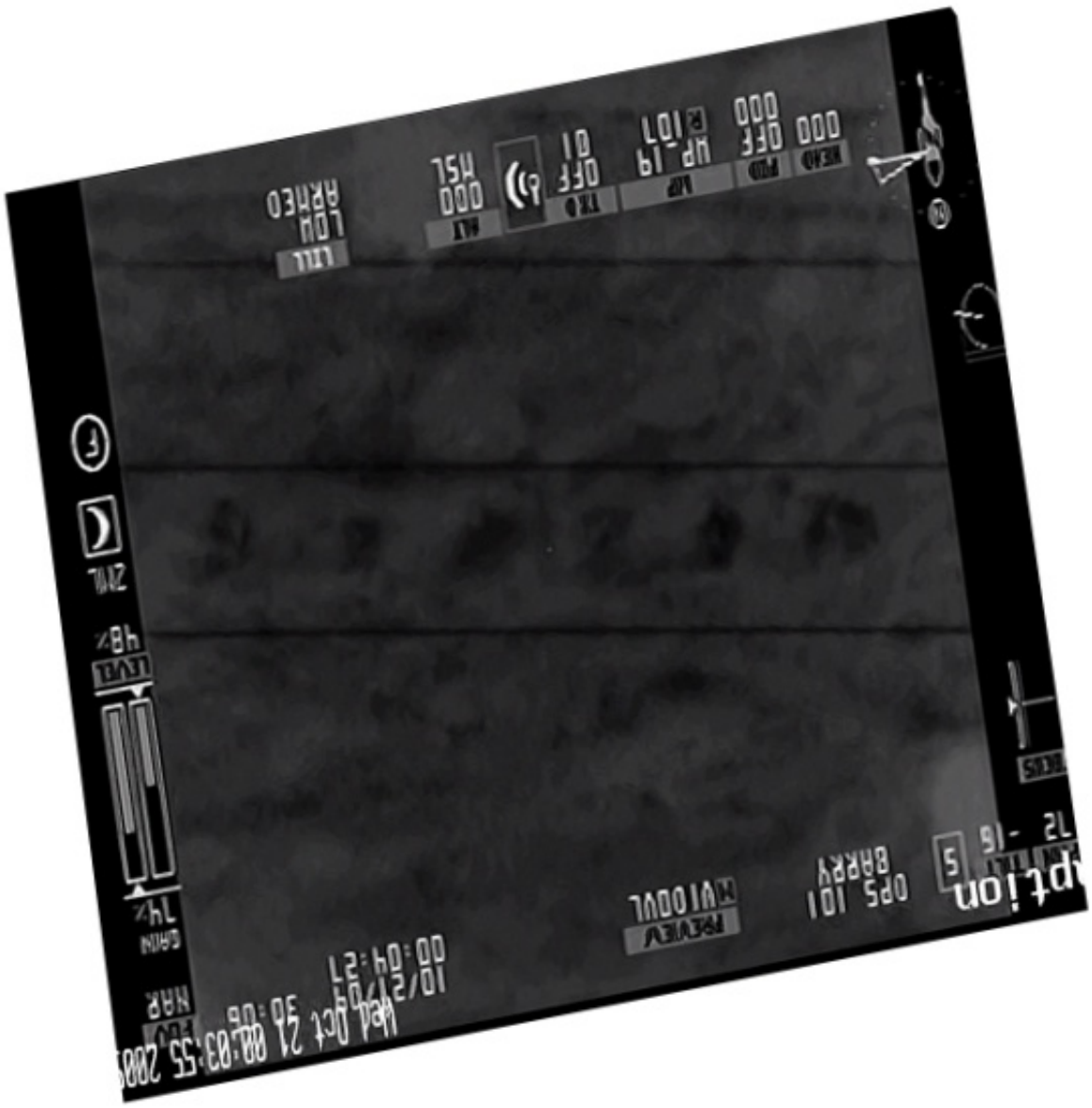

Figure I14. Rectified version of image 5e2.

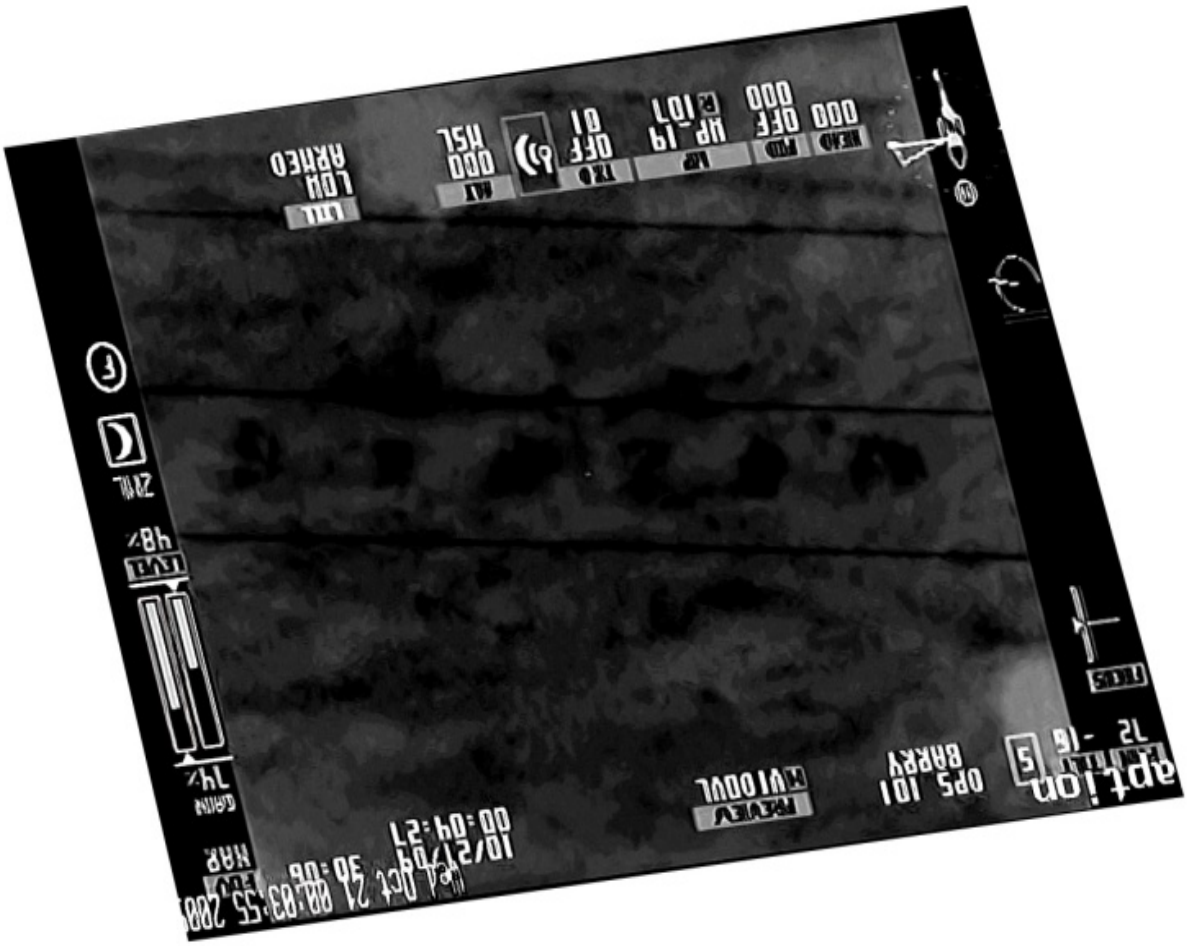

Figure I15. Rectified version of image 5e2f.

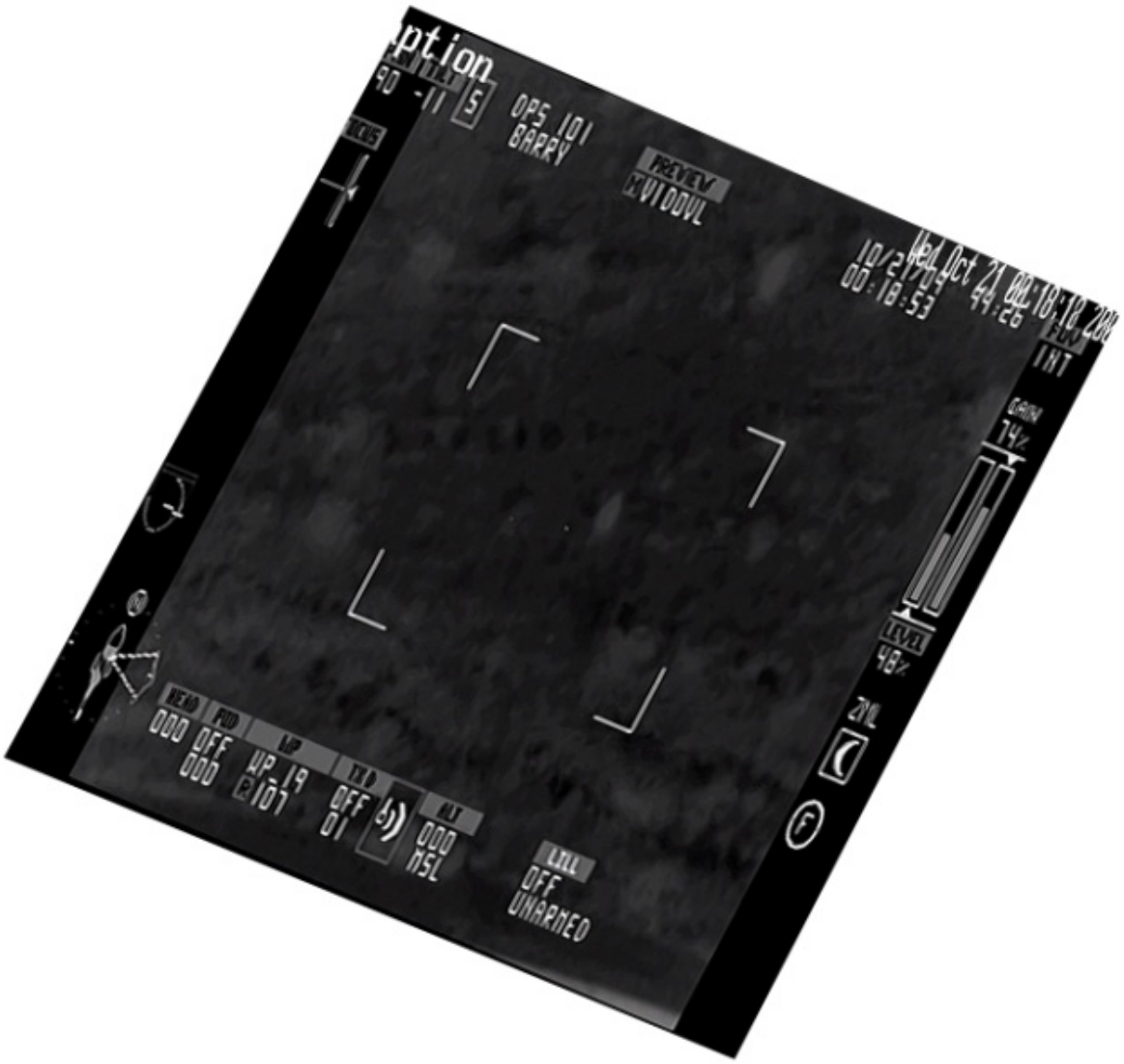

Figure I16. Rectified version of image 5r26f.

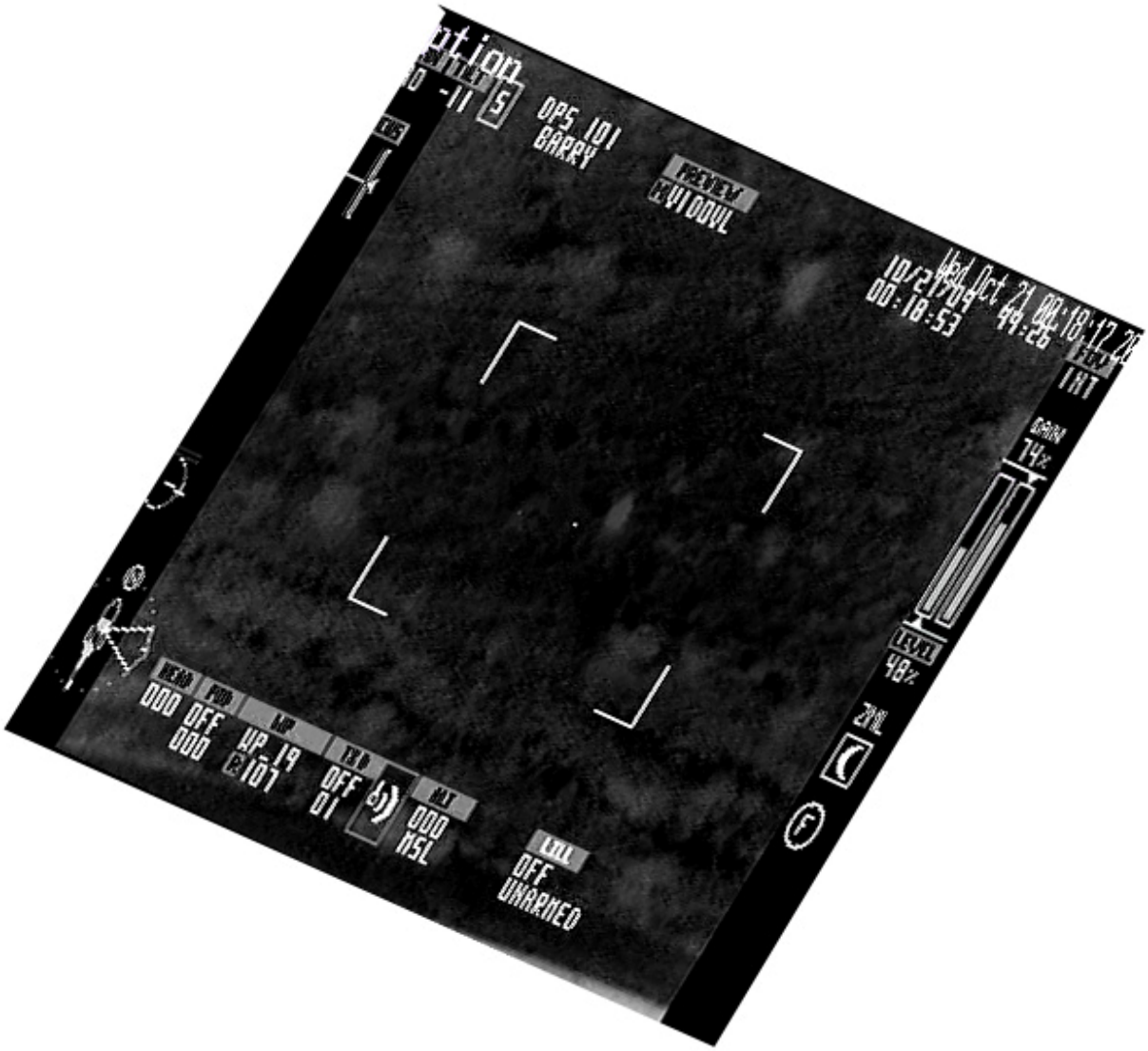

Figure I17. Rectified version of image 5e26.

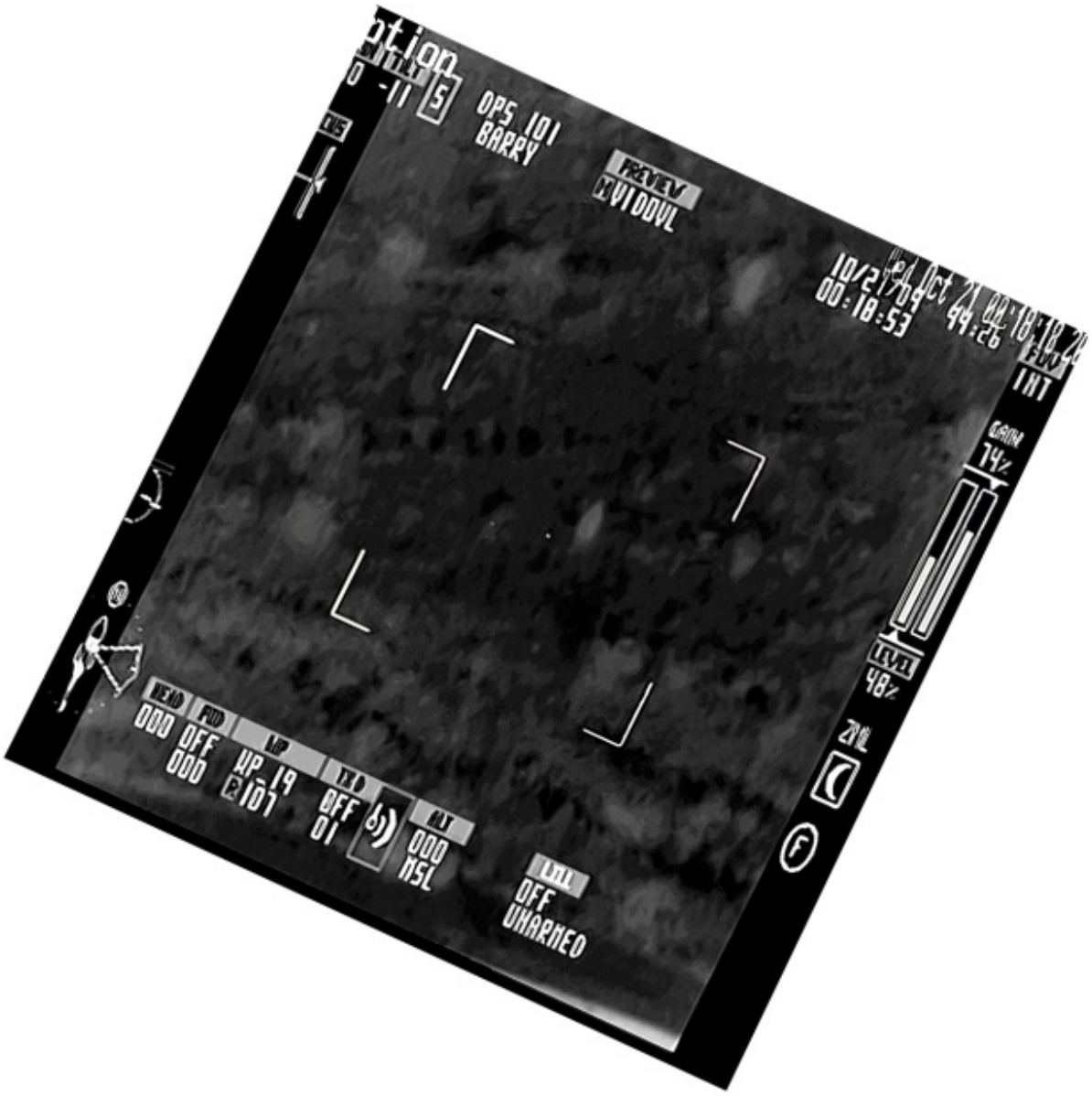

Figure I18. Rectified version of image 5e26f.

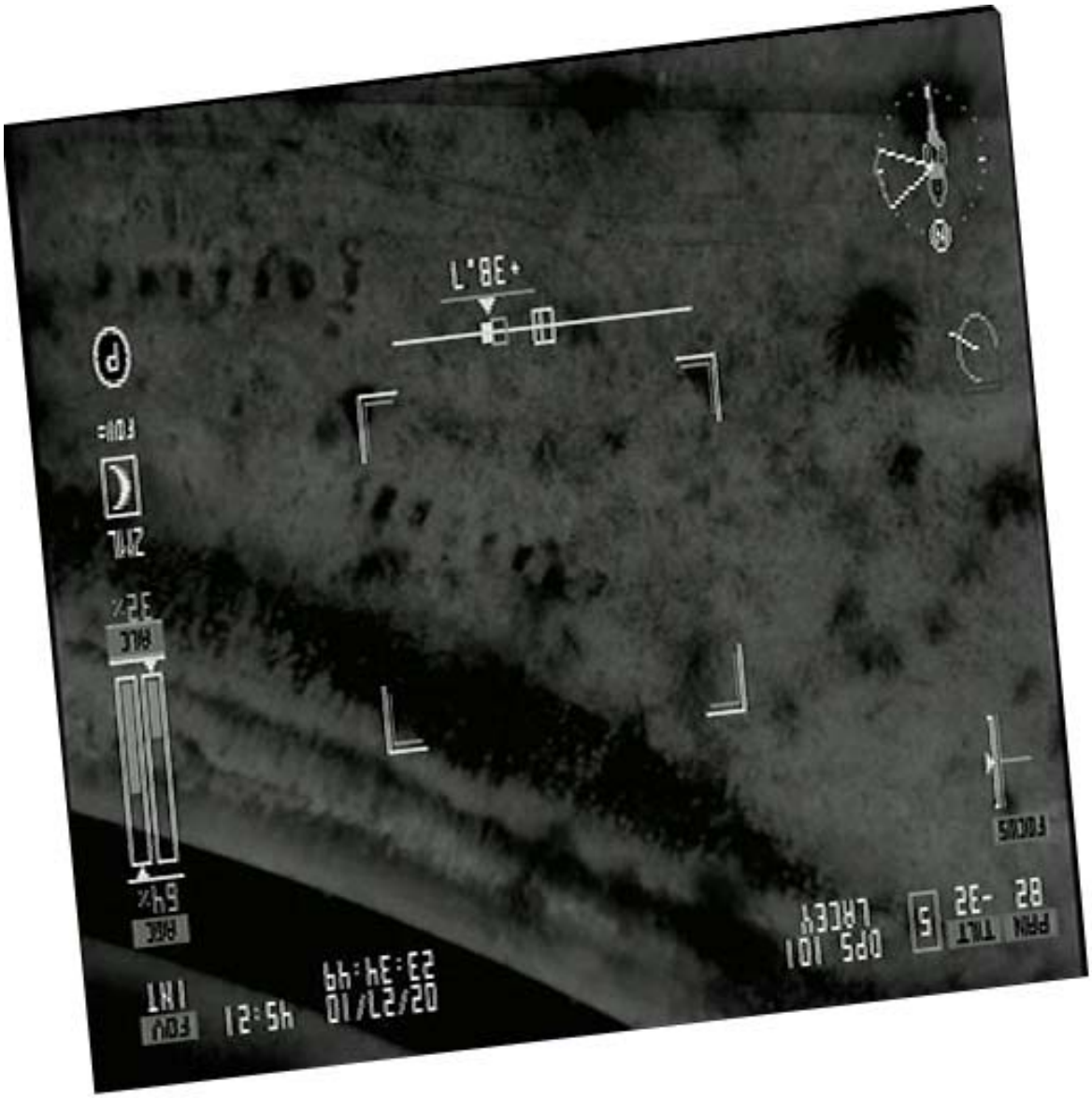

Figure I19. Rectified version of image 6r10.

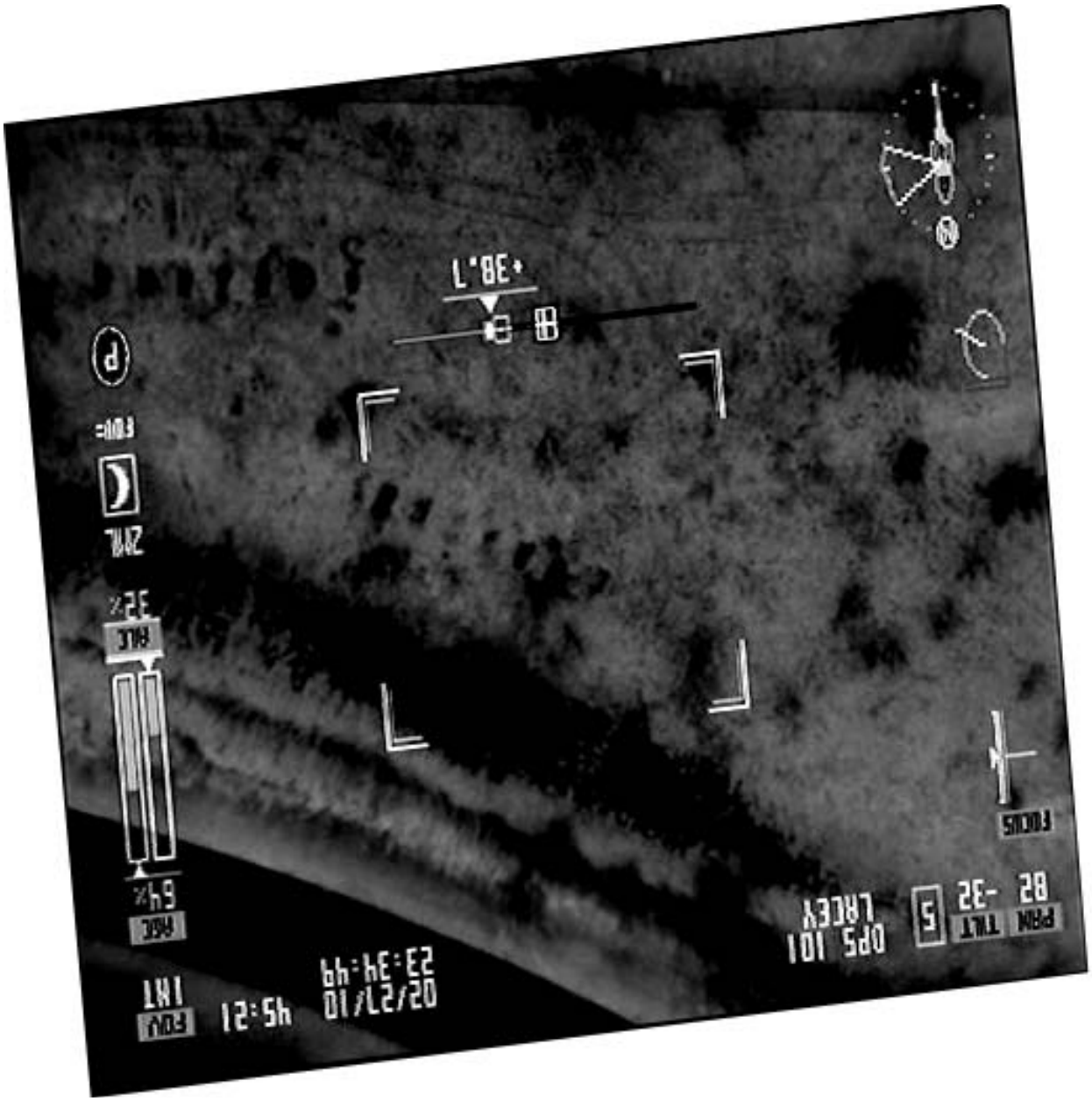

Figure I20. Rectified version of image 6r10f.

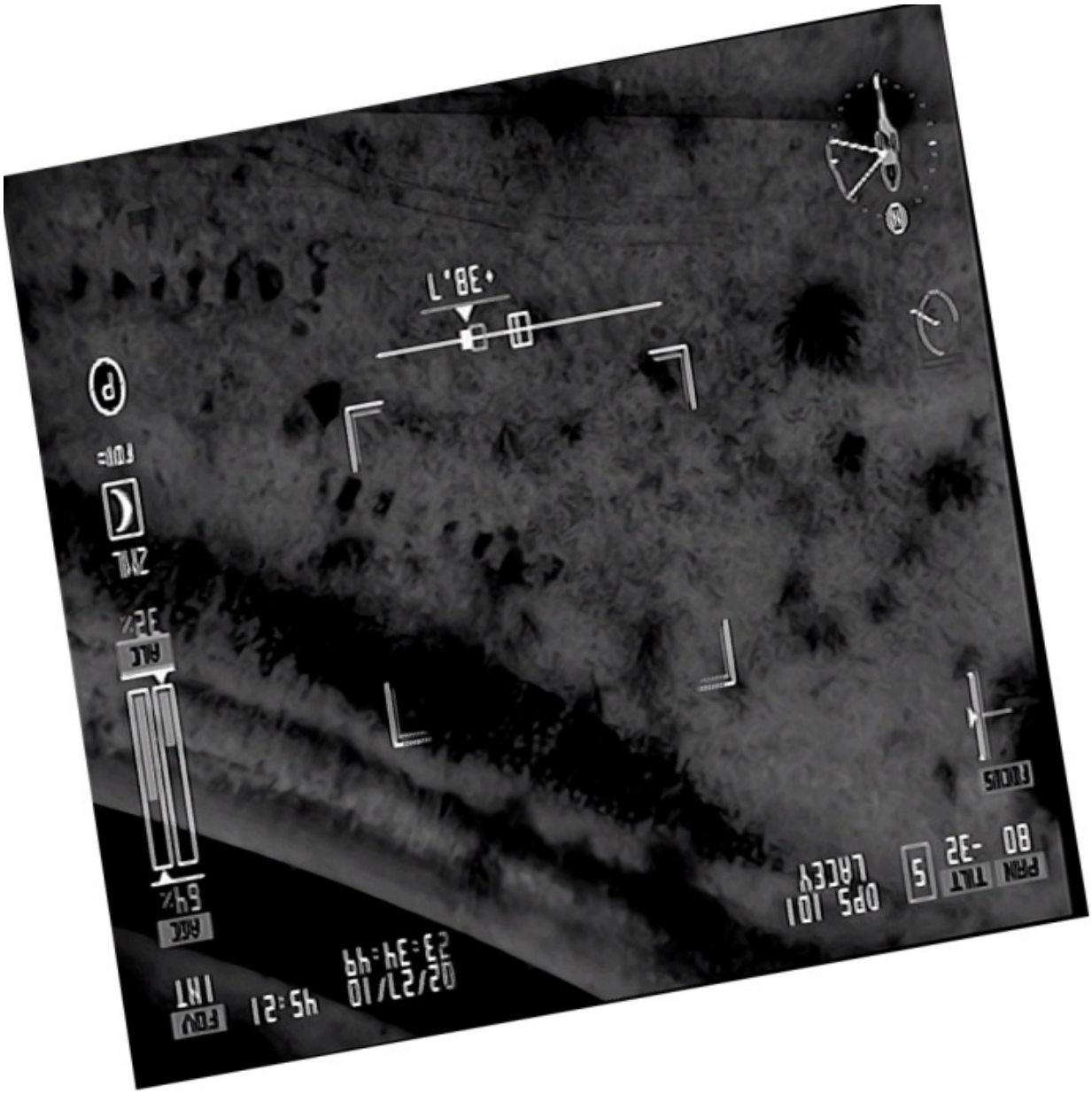

Figure I21. Rectified version of image 6e10.

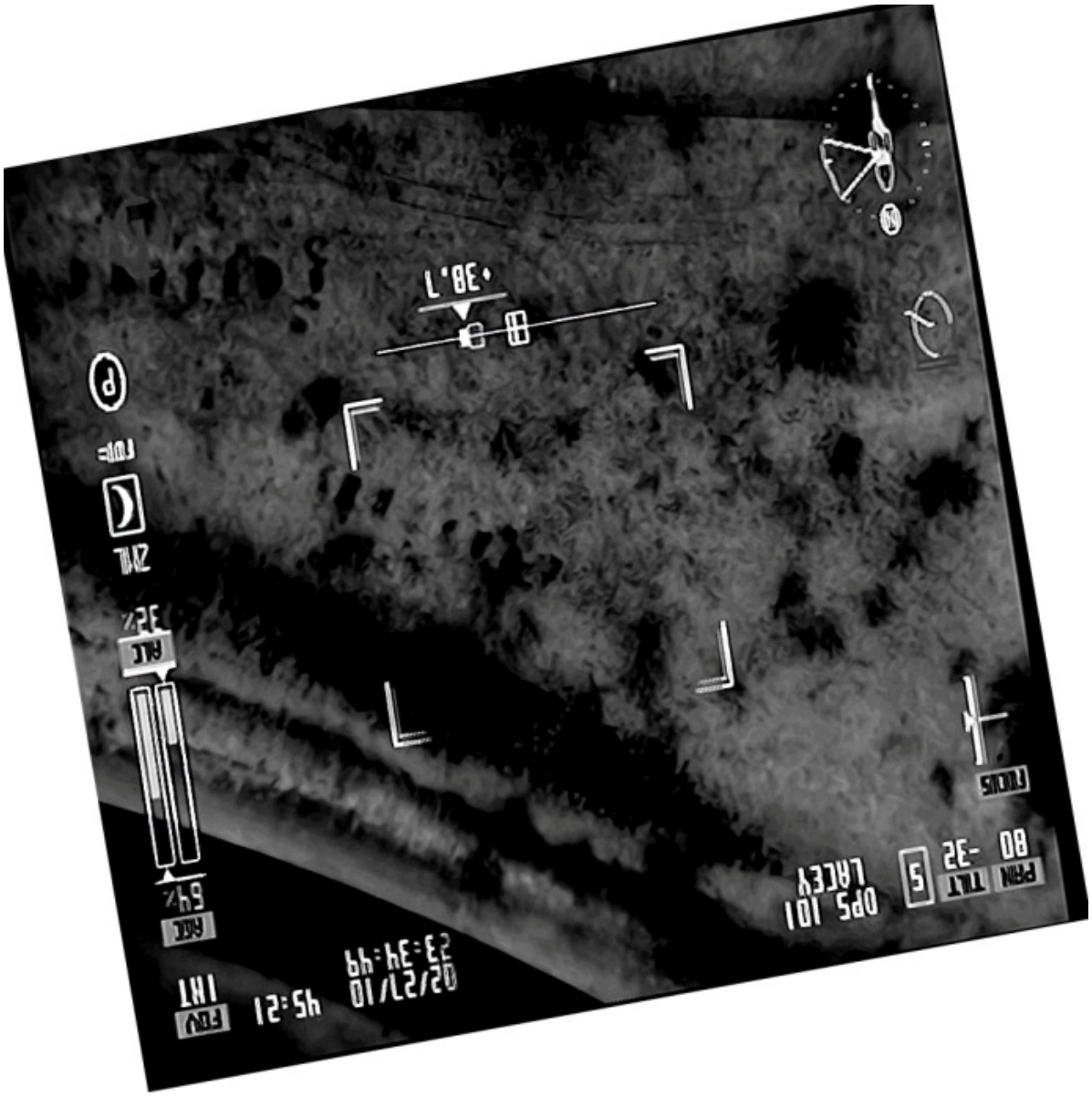

Figure I22. Rectified version of image 6e10f.

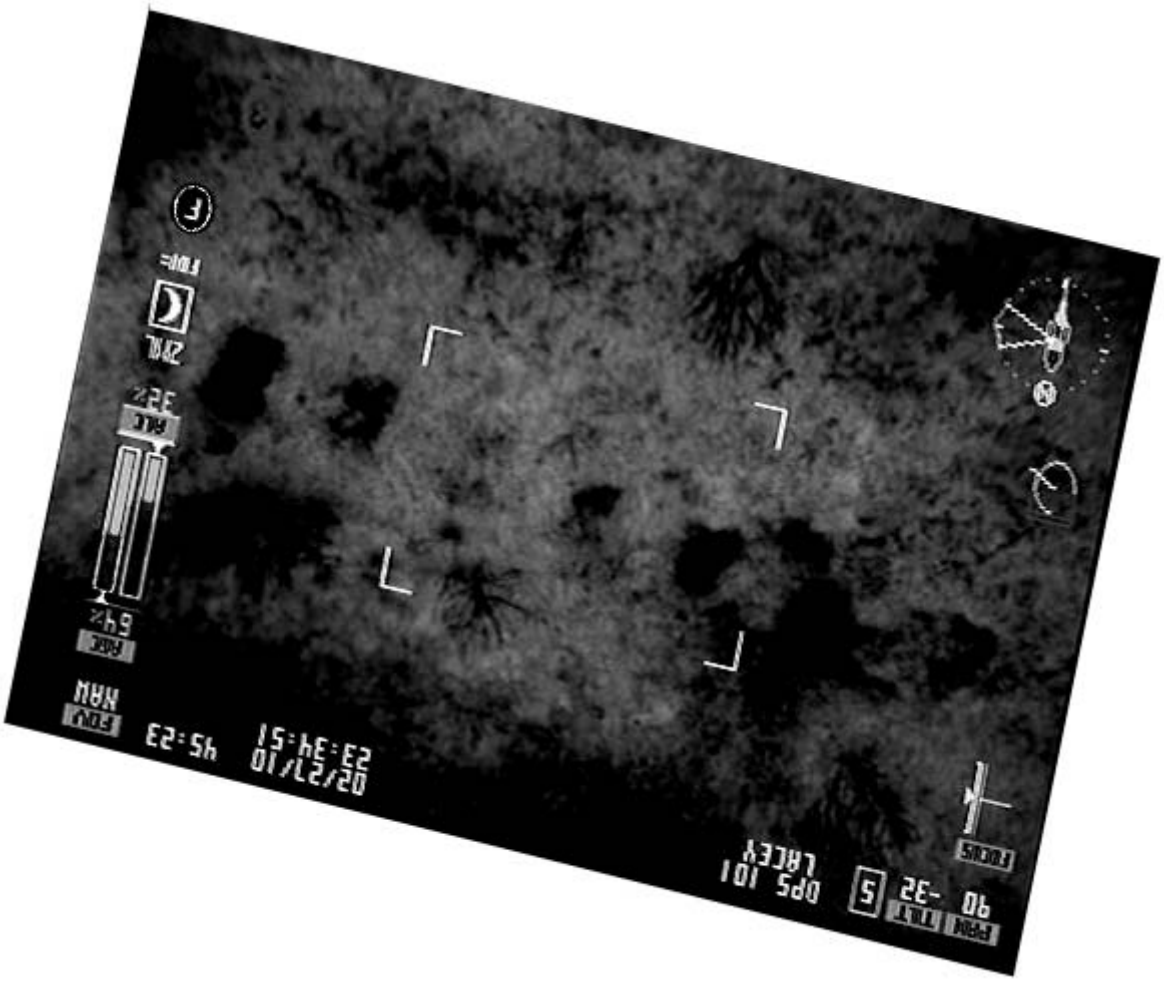

Figure I23. Rectified version of image 6r11f.

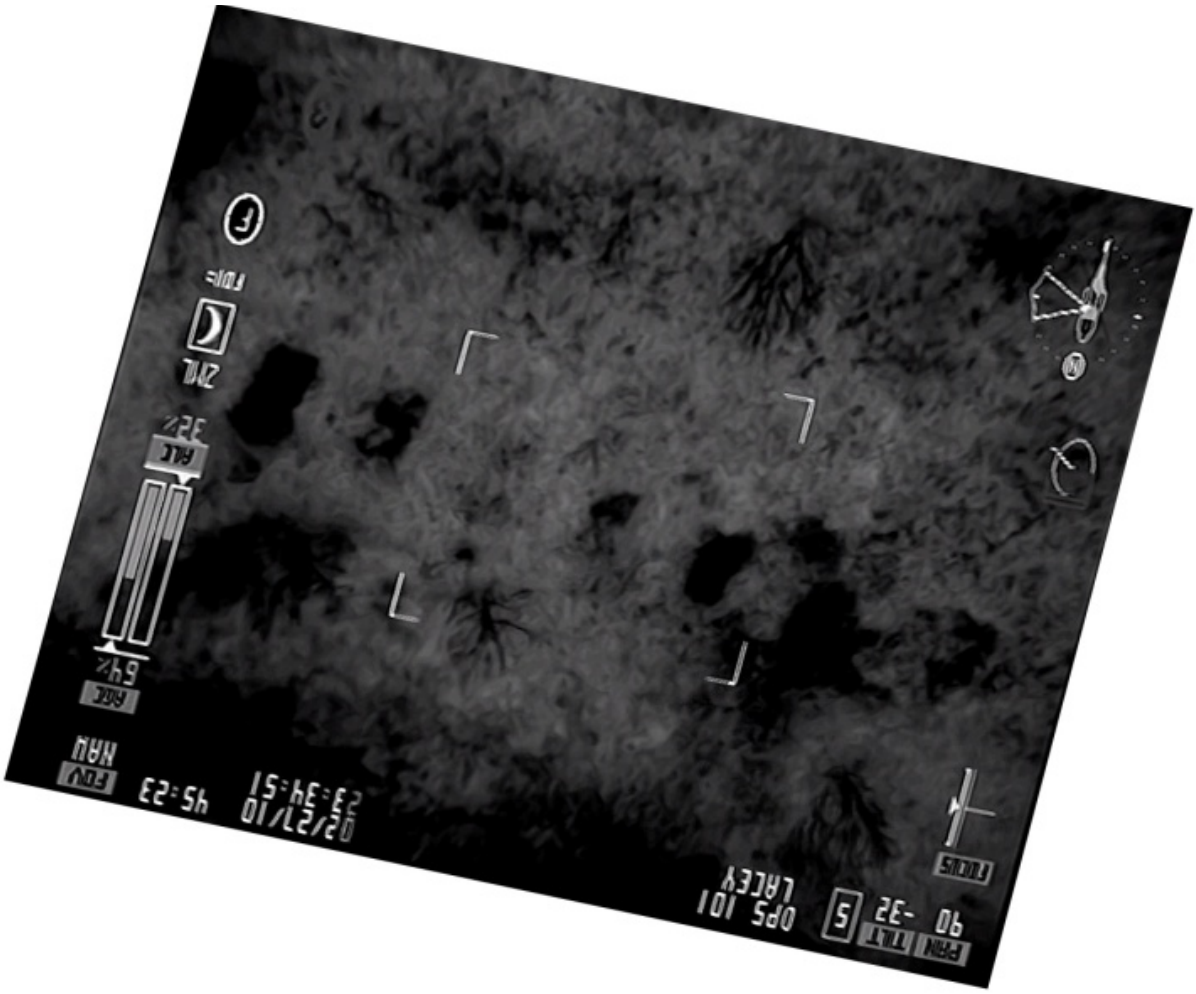

Figure I24. Rectified version of image 6e11.

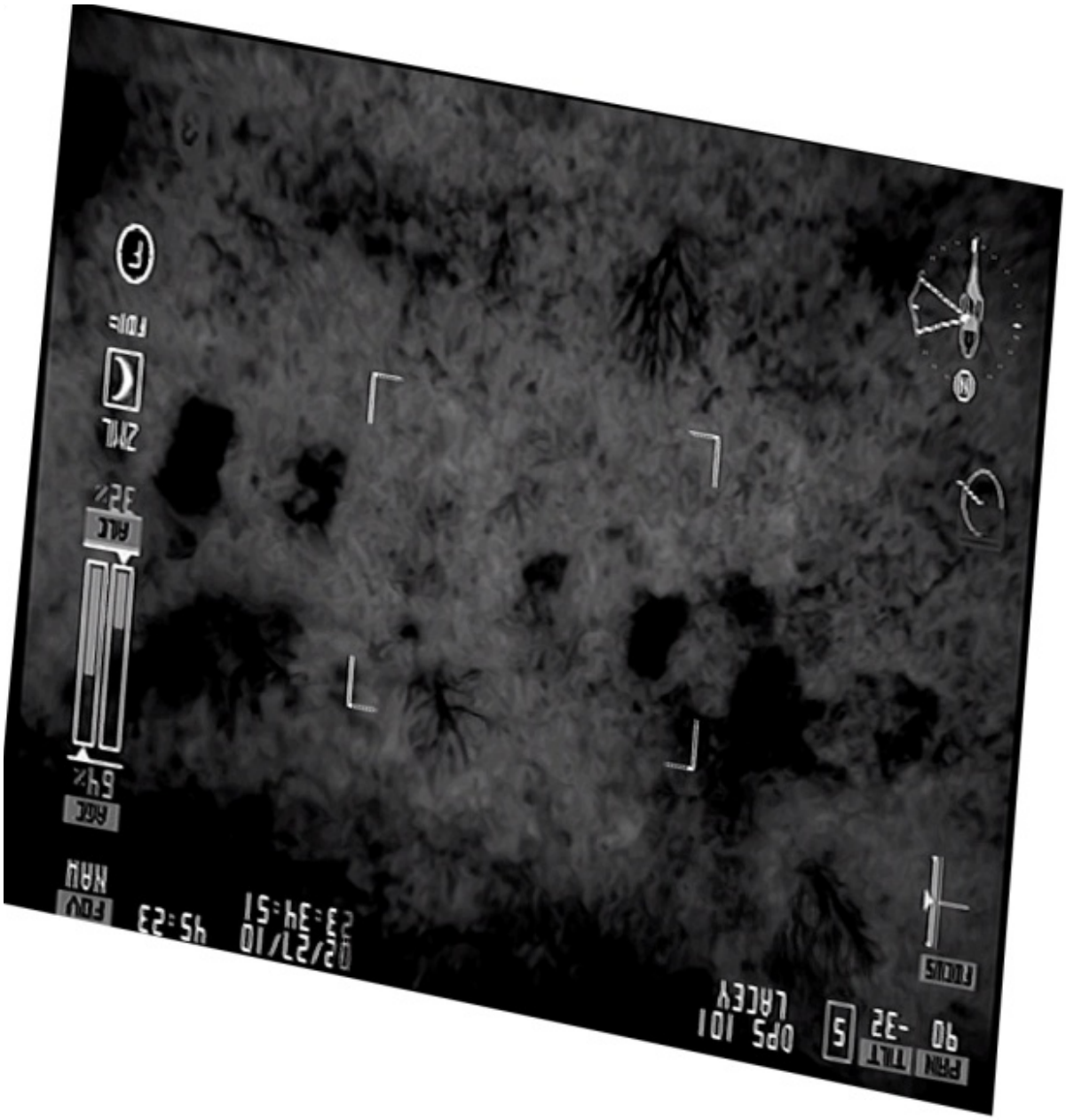

Figure I25. Rectified version of image 6e11f.

APPENDIX J

RESULTS OF STATISTICAL ANALYSES, PRESENTED BY IMAGE IN TABULAR FORMAT. SERIES 1_23, AS WELL AS IMAGES 4r25, 5r26, AND 6r11 WERE REPORTED IN CHAPTER 4 AND ARE NOT INCLUDED IN THIS APPENDIX

Table J1. Shapiro-Wilks normality testing and five number summaries for samples extracted from image 4r25f. "*" denotes a normal distribution.

	Unit ID	*n*	S-W *W*	*P*	Five Number Summaries
4r25f	E	128	0.9847*	=0.1619	80, 54, 48, 41, 23
	F	125	0.9097	<0.0001	98, 73, 70, 66, 48
	G	130	0.9098	<0.0001	97, 61, 50, 42, 29
	J	121	0.8621	<0.0001	113, 97, 93, 84, 45
	K	124	0.9752	=0.0221	86, 65.5, 57, 52, 39
	L	122	0.9558	=0.0005	97, 58, 51, 40, 25
	(P)	125	0.9545	=0.0003	151, 127, 120, 115, 101
	(Q)	125	0.981*	=0.0762	142, 128, 120, 110, 91
	(R)	125	0.9432	<0.0001	146, 131, 122, 118, 105
	(T)	125	0.9537	=0.0003	124, 110, 104, 98, 91
	(U)	125	0.9433	<0.0001	101, 85, 72, 65, 57
	(V)	121	0.9569	=0.0007	126, 114, 108, 103, 85
	(Y)	128	0.9763	=0.0243	181, 153, 145, 137, 123

Table J2. Shapiro-Wilks normality testing and five number summaries for samples extracted from image 4e25.

	Unit ID	*n*	S-W *W*	*P*	Five Number Summaries
4e25	E	491	0.9829	<0.0001	54, 43, 38, 35, 25
	F	492	0.895	<0.0001	66, 53, 52, 51, 44
	G	489	0.9293	<0.0001	66, 46, 43, 37, 31
	J	493	0.8975	<0.0001	79, 70, 67, 60, 34
	K	491	0.9601	<0.0001	63, 53, 47, 44, 35
	L	492	0.9675	<0.0001	73, 52, 48, 42, 32
	(P)	492	0.9049	<0.0001	105, 87, 80, 77.5, 72
	(Q)	492	0.9669	<0.0001	96, 85, 79, 74, 66
	(R)	492	0.9145	<0.0001	96, 86, 80, 78, 74
	(U)	492	0.9634	<0.0001	80, 68, 61, 58, 50
	(V)	493	0.9422	<0.0001	89, 79, 77, 74, 62
	(Y)	492	0.976	<0.0001	114, 102, 96, 92, 84

Table J3. Shapiro-Wilks normality testing and five number summaries for samples extracted from image 4e25f.

	Unit ID	*n*	S-W *W*	*P*	Five Number Summaries
4e25f	E	491	0.9808	<0.0001	79, 46, 37, 29, 0
	F	492	0.9164	<0.0001	91, 68, 65, 63, 38
	G	489	0.9689	<0.0001	81, 49, 45, 31, 13
	H	493	0.9711	<0.0001	104, 69, 64, 55, 27
	J	493	0.8699	<0.0001	124, 100, 95, 81, 31
	K	491	0.9738	<0.0001	86, 64, 50, 43, 24
	L	492	0.9787	<0.0001	78, 49, 43, 30, 12
	M	493	0.9117	<0.0001	70, 30, 18, 7, 0
	N	491	0.536	<0.0001	255, 34, 14, 3, 0
	(P)	492	0.9181	<0.0001	164, 136, 123, 119, 97
	(Q)	492	0.9814	<0.0001	159, 137, 122, 114, 91
	(R)	492	0.9502	<0.0001	160, 141, 137, 124, 114
	(U)	492	0.9515	<0.0001	106, 85, 73, 64, 47
	(V)	493	0.979	<0.0001	148, 120, 115, 109, 83
	(Y)	492	0.9824	<0.0001	198, 166, 158, 150, 125

Table J4. Shapiro-Wilks normality testing and five number summaries for samples extracted from image 5r26f. "*" denotes a normal distribution.

	Unit ID	*n*	S-W *W*	*P*	Five Number Summaries
5r26f	E	59	0.8587	<0.0001	23, 10, 4, 0, 0
	F	56	0.6658	<0.0001	16, 3, 0, 0, 0
	G	60	0.8334	<0.0001	18, 8, 2.5, 0, 0
	H	60	0.5298	<0.0001	30, 2, 0, 0, 0
	I	60	0.4006	<0.0001	13, 0, 0, 0, 0
	J	55	0.3245	<0.0001	2, 0, 0, 0, 0
	K	54	0.9262	=0.0026	26, 17, 9, 3, 0
	L	54	0.9526	=0.0324	34,28, 22, 14, 1
	M	54	0.9704	=0.2015*	43, 28, 20.5, 17, 9
	N	55	0.566	<0.0001	33, 4, 0, 0, 0
	(P)	56	0.9756	=0.3139*	31, 22, 19,13, 4
	(Q)	56	0.9615	=0.0713*	26, 15.5, 12, 9, 2
	(R)	56	0.9774	=0.3718*	38, 25.5, 17.5, 12, 0
	(S)	56	0.9752	=0.2995*	34, 19, 14, 8, 0
	(T)	56	0.98	=0.4771*	24, 14, 11.5, 8, 1
	(U)	56	0.9163	=0.0009	21, 10, 5, 1, 0
	(V)	55	0.9122	=0.0007	15, 13, 8, 5, 0
	(W)	55	0.855	<0.0001	22, 9, 3, 0, 0
	(X)	60	0.8844	<0.0001	29, 11, 5, 2, 0
	(Y)	60	0.8608	<0.0001	19, 6, 3, 0, 0

Table J5. Shapiro-Wilks normality testing and five number summaries for samples extracted from image 5e26.

	Unit ID	*n*	S-W *W*	*P*	Five Number Summaries
5e26	E	253	0.9043	<0.0001	28, 26, 21, 18, 15
	F	252	0.9707	<0.0001	27, 19, 18, 16, 10
	G	255	0.8315	<0.0001	28, 21, 18, 17, 15
	H	252	0.9457	<0.0001	25, 17, 12, 9, 5
	I	253	0.9307	<0.0001	21, 18, 17, 15, 9
	J	252	0.9312	<0.0001	20, 11, 10, 8, 4
	K	252	0.975	=0.0002	36, 29, 26, 24, 19
	L	251	0.9532	<0.0001	38, 34, 31, 27, 22
	M	251	0.9164	<0.0001	39, 36, 34, 32, 24
	N	251	0.9747	=0.0002	37, 26, 20, 16, 7
	O	251	0.8288	<0.0001	35, 18, 11, 9, 5
	(P)	252	0.9607	<0.0001	33, 29, 28, 27, 24
	(Q)	252	0.9413	<0.0001	30, 27, 26, 25, 23
	(R)	252	0.9344	<0.0001	37, 31, 28, 27, 24
	(S)	252	0.908	<0.0001	39, 35, 33, 27, 23
	(T)	252	0.9189	<0.0001	28, 26, 26, 25, 22
	(U)	252	0.883	<0.0001	30, 26, 25.5, 25, 15
	(V)	252	0.9602	<0.0001	32, 27, 26, 25, 21
	(W)	252	0.9156	<0.0001	28, 22, 19, 17, 14
	(X)	253	0.9521	<0.0001	29, 26, 25, 24, 18
	(Y)	253	0.9699	<0.0001	30, 25, 22, 21, 17

Table J6. Shapiro-Wilks normality testing and five number summaries for samples extracted from image 5e26f.

	Unit ID	*n*	S-W *W*	*P*	Five Number Summaries
5e26f	E	253	0.9188	<0.0001	41, 25, 21, 8, 0
	F	252	0.8853	<0.0001	26, 10, 6, 3, 0
	G	255	0.8457	<0.0001	30, 15, 8, 6, 0
	H	252	0.7371	<0.0001	28, 9, 0, 0, 0
	I	253	0.9202	<0.0001	16, 7, 4, 1, 0
	J	252	0.3078	<0.0001	11, 0, 0, 0, 0
	K	252	0.9823	=0.0031	44, 30, 25, 20.5, 7
	L	251	0.9421	<0.0001	51, 42, 32, 24, 10
	M	251	0.9333	<0.0001	52, 45, 40, 30, 20
	N	251	0.8816	<0.0001	56, 21, 9, 2, 0
	(P)	252	0.9895	=0.0177	37, 31, 29, 27, 20
	(Q)	252	0.9292	<0.0001	36, 26, 25, 23, 20
	(R)	252	0.949	<0.0001	47, 35, 29, 23, 17
	(S)	252	0.8916	<0.0001	50, 44, 37.5, 25, 20
	(T)	252	0.9599	<0.0001	30, 25, 24, 23, 19
	(U)	252	0.93	<0.0001	38, 26, 25, 23, 10
	(V)	252	0.9647	<0.0001	30, 24, 23, 21, 10
	(W)	252	0.9704	<0.0001	52, 30, 24, 20.5, 2
	(X)	253	0.9659	<0.0001	28, 23, 21, 17, 3
	(Y)	253	0.9752	=0.0002	30, 22, 16, 12, 3

Table J7. Shapiro-Wilks normality testing and five number summaries for samples extracted from image 6r11f.

	Unit ID	*n*	S-W *W*	*P*	Five Number Summaries
6r11f	J	769	0.0518	<0.0001	28, 0, 0, 0, 0
	K	769	0.7095	<0.0001	75, 18, 0, 0, 0
	L	768	0.9931	=0.0013	111, 75, 62, 49, 0
	M	770	0.9221	<0.0001	96, 57, 34, 6, 0
	N	769	0.4593	<0.0001	53, 0, 0, 0, 0
	O	768	0.3006	<0.0001	43, 0, 0, 0, 0
	(T)	769	0.8783	<0.0001	99, 60, 24, 0, 0
	(U)	769	0.9441	<0.0001	113, 81, 66, 46, 0

Table J8. Kilmogorov-Smirnov normality testing and five number summaries for samples extracted from image 6e11.

	Unit ID	*n*	K-S *D*	*P*	Five Number Summaries
6e11	J	3074	0.3843	<0.01	54, 1, 1, 1, 0
	K	3076	0.2207	<0.01	80, 27, 6, 1, 0
	L	3073	0.0438	<0.01	95, 71, 62, 53, 18
	M	3075	0.666	<0.01	78, 50, 37, 18, 0
	N	3075	0.4205	<0.01	47, 2, 1, 1, 0
	O	3073	0.4023	<0.01	33, 2, 1, 1, 0
	(U)	3073	0.1787	<0.01	255, 85, 76, 62, 11

Table J9. Kilmogorov-Smirnov normality testing and five number summaries for samples extracted from image 6e11f.

	Unit ID	*n*	K-S *D*	*P*	Five Number Summaries
6e11f	J	3074	0.3843	<0.01	54, 1, 1, 1, 0
	K	3076	0.2207	<0.01	80,27, 6, 1, 0
	L	3073	0.0438	<0.01	95, 71, 62, 53, 18
	M	3075	0.0666	<0.01	78, 50, 37, 18, 0
	N	3075	0.4205	<0.01	47, 2, 1, 1, 0
	O	3073	0.4023	<0.01	33, 2, 1, 1, 0
	(T)	3073	0.1608	<0.01	95,75, 69, 64, 1

Table J10. Shapiro-Wilks normality testing and five number summaries for samples extracted from image 1r22. "*" denotes a normal distribution.

	Unit ID	*n*	S-W *W*	*P*	Five Number Summaries
1r22	D	50	0.9683*	=0.1972	55, 51, 46, 43, 41
	E	51	0.9488	=0.0282	77, 69, 66, 62, 59
	F	49	0.9102	=0.0012	77, 75, 73, 69, 67
	G	50	0.9605*	=0.0932	76, 74, 73, 72, 69
	H	45	0.9809*	=0.0547	67, 60, 58, 55, 52
	I	50	0.823	<0.0001	68, 57, 55, 53, 52
	K	49	0.9611*	=0.1053	78, 69, 66, 62, 58
	L	48	0.9668*	=0.1889	96, 89, 84, 79.5, 74
	M	49	0.9708*	=0.2609	68, 59, 54, 51, 46
	N	48	0.9123	=0.0016	65, 47, 41, 37, 34
	(P)	49	0.9608*	=0.1021	108, 102, 99, 96, 83
	(Q)	49	0.9688*	=0.2177	112, 106, 99, 95, 81
	(R)	49	0.9496	=0.0356	118, 91, 82, 72, 63
	(S)	49	0.947	=0.028	109, 105, 101, 97, 86
	(T)	49	0.9501	=0.0376	106, 95, 89, 84, 77
	(U)	49	0.9598*	=0.0933	96, 91, 87, 81, 73
	(V)	48	0.9589*	=0.0909	109, 97, 88, 78, 69
	(W)	48	0.9455	=0.0264	87, 85, 82, 80, 77
	(X)	50	0.9476	=0.0273	106, 99, 92, 82, 76
	(Y)	50	0.9796*	=0.5340	111, 100, 95.5, 92, 85

Table J11. Shapiro-Wilks normality testing and five number summaries for samples extracted from image 1r22f. "*" denotes a normal distribution.

	Unit ID	*n*	S-W *W*	*P*	Five Number Summaries
1r22f	D	50	0.9405	=0.0141	84, 60, 53, 47, 39
	E	51	0.9653*	=0.1397	122, 100, 89, 82, 72
	F	49	0.9552*	=0.0602	114, 108, 104, 98, 93
	G	50	0.9802*	=0.5586	113, 108, 105, 103, 96
	H	45	0.9295	=0.009	99, 80, 74, 67, 60
	I	50	0.8623	<0.0001	96, 72, 64, 61, 57
	J	48	0.9725*	=0.3155	92, 72.5, 58.5, 48, 31
	K	49	0.9625*	=0.1197	108, 97, 94, 87, 75
	L	48	0.9765*	=0.4442	157, 142, 132.5, 123, 109
	M	49	0.9700*	=0.2429	90, 69, 61, 54, 43
	(P)	49	0.884	=0.0002	177, 170, 164, 158, 131
	(Q)	49	0.9852*	=0.7898	196, 175, 162, 157, 130
	(R)	49	0.9541*	=0.0543	220, 188, 151, 125, 84
	(S)	49	0.9738*	=0.3407	194, 181, 171, 162, 135
	(T)	49	0.9579	=0.0772	167, 157, 145, 134, 115
	(U)	49	0.9705*	=0.2534	156, 144, 132, 125, 105
	(V)	48	0.9416	=0.0187	183, 162, 139.5, 119.5, 100
	(W)	48	0.9254	=0.0046	149, 132, 130, 125, 118
	(X)	50	0.9747*	=0.3548	178, 166, 157.5, 150, 133
	(Y)	50	0.9573*	=0.0686	192, 169, 158, 148, 132

Table J12. Shapiro-Wilks normality testing and five number summaries for samples extracted from image 1e22.

	Unit ID	*n*	S-W *W*	*P*	Five Number Summaries
1e22	D	254	0.9387	<0.0001	60, 50, 46, 44, 39
	E	253	0.9673	<0.0001	86, 72, 68, 63, 58
	F	252	0.9237	<0.0001	83, 78, 76, 71, 66
	G	255	0.9632	<0.0001	81, 77, 76, 74, 69
	H	252	0.9727	<0.0001	73, 62, 58, 53, 48
	I	253	0.8079	<0.0001	71, 57, 53, 52, 48
	K	252	0.9786	=0.0008	88, 73.5, 69, 65.5, 54
	L	251	0.964	<0.0001	111, 99, 94, 86, 76
	M	251	0.9726	<0.0001	69, 58, 53, 49, 40
	N	251	0.905	<0.0001	72, 44, 36, 29, 22
	(P)	252	0.9087	<0.0001	118, 110, 104,101, 82
	(Q)	252	0.9716	<0.0001	125, 113, 105, 102, 85
	(R)	252	0.9573	<0.0001	125, 94.5, 83, 73, 62
	(S)	252	0.9393	<0.0001	123, 113, 110, 100, 85
	(T)	252	0.9522	<0.0001	114, 102, 95, 87, 82
	(U)	252	0.9404	<0.0001	103, 96, 91, 83, 63
	(V)	252	0.9422	<0.0001	119, 104, 93, 81, 72
	(W)	252	0.9649	<0.0001	95, 88, 86, 85, 78
	(X)	253	0.9299	<0.0001	114, 105, 101, 88, 81
	(Y)	253	0.9712	<0.0001	121, 108, 103, 98, 82

Table J13. Shapiro-Wilks normality testing and five number summaries for samples extracted from image 1e22f.

	Unit ID	*n*	S-W *W*	*P*	Five Number Summaries
1e22f	D	254	0.9373	<0.0001	74, 50, 41, 38, 27
	E	253	0.955	<0.0001	119, 95, 89, 77, 70
	F	252	0.9252	<0.0001	122, 115.5, 109, 98, 89
	G	255	0.9845	=0.0071	123, 114, 110, 107, 95
	H	252	0.9703	<0.0001	94, 77, 70, 60, 50
	I	253	0.7858	<0.0001	100, 71, 60, 57, 50
	K	252	0.9787	=0.0008	125, 100, 94, 84, 65
	L	251	0.966	<0.0001	179, 152, 136, 125, 111
	M	251	0.9694	<0.0001	138, 93, 76, 59, 34
	(P)	252	0.9034	<0.0001	201, 190, 177.5, 168, 119
	(Q)	252	0.9619	<0.0001	224, 204.5, 180, 170, 124
	(R)	252	0.9574	<0.0001	223, 155, 128, 103.5, 80
	(S)	252	0.9576	<0.0001	219, 200, 191, 175.5, 147
	(T)	252	0.9305	<0.0001	199, 185, 173.5, 151.5, 123
	(U)	252	0.9207	<0.0001	194, 146, 136, 127, 110
	(V)	252	0.9507	<0.0001	219, 186, 171, 137.5, 105
	(W)	252	0.9734	<0.0001	158, 140, 136, 131, 114
	(X)	253	0.9409	<0.0001	189, 158, 137, 130, 109
	(Y)	253	0.959	<0.0001	210, 193, 177, 162, 134

Table J14. Results of Kruskall-Wallis testing, SNK multiple range test on ranked data (α=0.05), and Spearman's ranked correlation on image series 1_22.

	K-W *H*	DF	*P*	SNK Grouping	r_s	*P*
1r22	852.92	19	<0.0001	S(0) = Q(0) = P(0) = Y(0) > X(0) = T(0) = V(0) = U(0) = L(0.25) > R(0) = W(0) > G(0.5) = F(0.25) > K(0.5) = E(0.5) > H (1) = I(1.5) = M(0.5) > D(1) > N(1)	-0.8661	<0.0001
1r22f	852.2	19	<0.0001	S(0) = Q(0) > P(0) = Y(0) > X(0) > T(0) > V(0) = L(0.25) > U(0) > W(0) > R(0) > G(0.5) = F(0.25) > K(0.5) > E(0.5) > H(1) > I(1.5) > M(0.5) > D(1) = N(1)	-0.8691	<0.0001
1e22	4316.45	19	<0.0001	S(0) = Q(0) > P(0) > = Y(0) > X(0) > T(0) > V(0) = L(0.25) > U(0) > W(0) > R(0) > G(0.5) = F(0.25) > K(0.5) > E(0.5) > H(1) > I(1.5) > M(0.5) = D(1) = N(1)	-0.8439	<0.0001
1e22f	4089.5	18	<0.0001	S(0) > Q(0) > Y(0) = P(0) > T(0) > V(0) > X(0) > U(0) = L(0.25) = W(0) > R(0) > G(0.5) > F(0.25) > K(0.5) > E(0.5) > M(0.5) >H(1) = I(1.5) > D(1)	-0.85	<0.0001

Table J15. Shapiro-Wilks normality testing and five number summaries for samples extracted from image 4r22. "*" denotes a normal distribution.

	Unit ID	*n*	S-W *W*	*P*	Five Number Summaries
4r22	E	101	0.9558	=0.0019	58, 52, 48, 44, 39
	F	103	0.976*	=0.0574	67, 60, 57, 55, 47
	G	103	0.9593	=0.003	66, 53, 50, 46, 39
	H	104	0.9075	<0.0001	71, 60, 53, 50, 43
	I	101	0.956	=0.002	64, 51, 47, 42, 38
	J	102	0.943	=0.0003	62, 54, 50, 40, 30
	(P)	103	0.6601	<0.0001	142, 82, 79, 76, 70
	(Q)	103	0.9643	=0.0071	86, 79, 74, 71, 67
	(R)	103	0.9644	=0.0072	92, 85, 82, 79, 69
	(S)	103	0.9439	=0.0003	97, 85, 77, 71, 67
	(Y)	101	0.9785*	=0.0979	88, 79, 76, 73, 67

Table J16. Shapiro-Wilks normality testing and five number summaries for samples extracted from image 4r22f. "*" denotes a normal distribution.

	Unit ID	*n*	S-W *W*	*P*	Five Number Summaries
4r22f	E	101	0.9739	=0.0428	80, 63, 54, 47, 37
	F	103	0.9742	=0.0417	99, 83, 77, 73, 54
	G	103	0.9596	=0.0032	95, 68, 61, 52, 37
	H	104	0.9657	=0.0085	90, 70, 65.5, 60, 42
	I	101	0.9576	=0.0025	76, 60, 48, 41, 34
	(P)	103	0.6737	<0.0001	255, 131, 124, 118, 104
	(Q)	103	0.9691	=0.0163	139, 126, 118, 111, 102
	(R)	103	0.9744	=0.0428	154, 140, 134, 128, 106
	(S)	103	0.94	=0.0002	160, 136, 120, 106, 98
	(Y)	101	0.9904*	=0.6943	142, 124, 118, 111, 94

Table J17. Shapiro-Wilks normality testing and five number summaries for samples extracted from image 4e22.

	Unit ID	*n*	S-W *W*	*P*	Five Number Summaries
4e22	E	768	0.9755	<0.0001	60, 50, 45, 42, 33
	F	769	0.9842	<0.0001	71, 60, 58, 54, 46
	G	770	0.9769	<0.0001	63, 52, 48, 44, 31
	H	775	0.9523	<0.0001	65, 54, 52, 50, 36
	I	770	0.9467	<0.0001	56, 44, 40, 36, 30
	(P)	769	0.8185	<0.0001	152, 87, 82, 79, 72
	(Q)	769	0.9477	<0.0001	89, 84, 78, 75, 67
	(R)	769	0.9443	<0.0001	99, 93, 87, 86, 70
	(S)	769	0.954	<0.0001	102, 88, 79, 73, 64
	(Y)	770	0.9805	<0.0001	94, 83, 79, 75, 67

Table J18. Shapiro-Wilks normality testing and five number summaries for samples extracted from image 4e22f.

	Unit ID	*n*	S-W *W*	*P*	Five Number Summaries
4e22f	E	768	0.9707	<0.0001	74, 52, 48, 42, 22
	F	769	0.9823	<0.0001	109, 82, 74, 68, 51
	G	770	0.9774	<0.0001	86, 64, 55, 46, 22
	H	775	0.9434	<0.0001	91, 66, 64, 60, 27
	I	770	0.9366	<0.0001	78, 47, 38, 29, 18
	(P)	769	0.826	<0.0001	255, 138, 128, 122, 99
	(Q)	769	0.9557	<0.0001	147, 136, 122, 117, 96
	(R)	769	0.9332	<0.0001	168, 154, 142, 139, 117
	(S)	769	0.9453	<0.0001	164, 136, 118, 102, 86
	(Y)	770	0.9447	<0.0001	175, 140, 130, 122, 109

Table J19. Results of Kruskall-Wallis testing, SNK multiple range test on ranked data (α=0.05), and Spearman's ranked correlation on image series 4_22.

	K-W *H*	DF	*P*	SNK Grouping	r_s	*P*
4r22	910.99	10	< 0.0001	R(0) > P(0) = S(0) = Y(0) = Q(0) > F(0.25) > H(1) > G(0.5) > J(1) > E(0.5) > I(1.5)	-0.839	< 0.0001
4r22f	855.82	9	< 0.0001	R(0) > P(0) > S(0) = Q(0) = Y(0) > F(0.25) > H(1) > G(0.5) > E(0.5) > I(1.5)	-0.869	< 0.0001
4e22	7076.2	9	< 0.0001	R(0) > P(0) > S(0) > Y(0) = Q(0) > F(0.25) > H(1) > G(0.5) > E(0.5) > I(1.5)	-0.867	< 0.0001
4e22f	6605.6	9	< 0.0001	R(0) > Y(0) > P(0) > Q(0) > S(0) > F(0.25) > H(1) > G(0.5) > E(0.5) > I(1.5)	-0.871	< 0.0001

Table J20. Normality testing results and five number summaries for samples extracted from image series 5_2. Shapiro-Wilks is presented for image 5r2 and 5r2f; Kilmogorov-Smirnov D was calculated for the remaining two images due to large sample sizes.

	Unit ID	*n*	S-W *W*	*P*	Five Number Summaries
5r2	D	770	0.981	<0.0001	42, 36, 33, 30, 23
	E	768	0.974	<0.0001	49, 39, 34, 30, 23
	F	769	0.9343	<0.0001	50, 35, 30, 26, 21
	G	770	0.9863	<0.0001	46, 36, 34, 31, 23
	H	775	0.9234	<0.0001	51, 34, 28, 24, 17
	I	770	0.9784	<0.0001	53, 42, 35, 30, 20
	(P)	769	0.9685	<0.0001	53, 42, 41, 40, 32
5r2f	D	770	0.9733	<0.0001	43, 28, 20, 12, 0
	E	768	0.9528	<0.0001	50, 33, 21, 9, 0
	F	769	0.8872	<0.0001	48, 24, 10, 1, 0
	G	770	0.9898	<0.0001	43, 25, 18, 12, 0
	H	775	0.8519	<0.0001	53, 25, 7, 0, 0
	I	770	0.9593	<0.0001	53, 33, 20, 10, 0
	(P)	769	0.9862	<0.0001	56, 39, 35, 31, 8
5e2	E	3073	0.1032	<0.01	46, 34, 27, 24, 14
	F	3073	0.1622	<0.01	46, 30, 22, 18, 14
	G	3074	0.1427	<0.01	45, 32, 28, 26, 15
	H	3075	0.1012	<0.01	46, 26, 20, 16, 6
	I	3076	0.0837	<0.01	50, 35, 27.5, 23, 15
	(P)	3073	0.1775	<0.01	47, 38, 37, 36, 31
	(Q)	3073	0.1434	<0.01	55, 45, 44, 43, 30
	(R)	3073	0.0836	<0.01	53, 41, 36, 33, 20
5e2f	E	3073	0.2035	<0.01	47, 24, 9, 0, 0
	F	3073	0.3012	<0.01	46, 19, 0, 0, 0
	G	3074	0.1949	<0.01	43, 17, 6, 0, 0
	H	3075	0.303	<0.01	45, 19, 0, 0, 0
	I	3076	0.159	<0.01	61, 28, 12, 0, 0
	(P)	3073	0.8569	<0.01	48, 34, 28, 23, 10
	(Q)	3073	0.1228	<0.01	59, 39, 30, 19, 0

Table J21. Results of Kruskall-Wallis testing, SNK multiple range test on ranked data (α=0.05), and Spearman's ranked correlation on image series 5_2.

	K-W *H*	DF	*P*	SNK Grouping	r_s	*P*
5r2	1520.1	6	< 0.0001	P(0) > I(1.5) > E(0.5) = G(0.5) > D(1) > F(0.25) > H(1)	-0.214	< 0.0001
5r2f	1366.7	6	< 0.0001	P(0) > E(0.5) = I(1.5) = D(1) > G(0.5) > F(0.25) = H(1)	-0.218	< 0.0001
5e2	17625	7	< 0.0001	Q(0) > P(0) > R(0) > I(1.5) > E(0.5) = G(0.5) > F(0.25) > H (1)	-0.648	< 0.0001
5e2f	6870.6	6	< 0.0001	P(0) = Q(0) > I(1.5) > E(0.5) > G(0.5) > H(1) > F(0.25)	-0.368	< 0.0001

Table J22. Shapiro-Wilks normality testing and five number summaries for samples extracted from image 6r10. "*" denotes a normal distribution.

	Unit ID	*n*	S-W *W*	*P*	Five Number Summaries
6r10	E	63	0.8928	<0.0001	26, 13, 8, 4, 2
	F	64	0.876	<0.0001	36, 17.5, 11, 8, 5
	G	62	0.9503	<0.0001	45, 28, 16.5, 9, 2
	H	60	0.7889	<0.0001	43, 12.5, 5.5, 3, 0
	I	63	0.8498	<0.0001	30, 12, 6, 4, 1
	J	62	0.7932	<0.0001	46, 14, 7, 4, 1
	K	64	0.9561	=0.0231	50, 37, 25, 13.5, 4
	L	63	0.972*	=0.1606	73, 66, 62, 56, 48
	M	65	0.9805*	=0.394	65, 48, 42, 30, 16
	N	62	0.8284	<0.0001	46, 18, 7, 4, 0
	(P)	64	0.9662*	=0.0765	61, 57, 55, 52, 45
	(Q)	64	0.964*	=0.0586	74, 66.5, 62, 56, 49
	(R)	64	0.9427	=0.0051	69, 55, 52.5, 49, 43
	(S)	64	0.8545	<0.0001	61, 57.5, 54.5, 41.5, 28
	(T)	64	0.9414	=0.0044	79, 73, 70, 68.5, 55
	(U)	64	0.8561	<0.0001	83, 77, 73, 68.5, 44,
	(V)	62	0.9341	=0.0025	78, 70, 61, 57, 51
	(W)	62	0.9612*	=0.0671	71, 65, 61, 57, 50

Table J23. Shapiro-Wilks normality testing and five number summaries for samples extracted from image series 6r10f. "*" denotes a normal distribution.

	Unit ID	*n*	S-W *W*	*P*	Five Number Summaries
6r10f	E	63	0.2242	<0.0001	10, 0, 0, 0, 0
	F	64	0.3452	<0.0001	4, 0, 0, 0, 0
	G	62	0.6255	<0.0001	30, 5, 0, 0, 0
	H	60	0.4828	<0.0001	42, 0, 0, 0, 0
	I	63	0.2561	<0.0001	21, 0, 0, 0, 0
	J	62	0.2214	<0.0001	8, 0, 0, 0, 0
	K	64	0.8087	<0.0001	35, 16, 3, 0, 0
	L	63	0.9655*	=0.0742	83, 72, 66, 53, 37
	M	65	0.9572	=0.0246	74, 42, 32, 15, 0
	N	62	0.3725	<0.0001	26, 0, 0, 0, 0
	(P)	64	0.9744*	=0.2052	63, 57, 51.5, 47.5, 34
	(Q)	64	0.9611	=0.0418	87, 75, 66.5, 55, 45
	(R)	64	0.9442	=0.006	76, 54.5, 50, 43.5, 35
	(S)	64	0.8344	<0.0001	63, 57, 52.5, 32.5, 5
	(T)	64	0.9777*	=0.2995	95, 84.5, 81, 78, 71
	(U)	64	0.8554	<0.0001	102, 92, 87.5, 80.5, 36
	(V)	62	0.9368	=0.0032	99, 82, 68.5, 57, 44
	(W)	62	0.9792*	=0.3725	84, 72, 64, 58, 46

Table J24. Shapiro-Wilks normality testing and five number summaries for samples extracted from image series 6e10.

	Unit ID	*n*	S-W *W*	*P*	Five Number Summaries
6e10	E	253	0.6664	<0.0001	30, 5, 2, 1, 0
	F	252	0.7193	<0.0001	64, 22.5, 4, 2, 0
	G	255	0.8458	<0.0001	54, 23, 8, 2, 0
	H	252	0.6754	<0.0001	53, 15.5, 2, 1, 0
	I	253	0.5538	<0.0001	38, 3, 1, 1, 0
	J	252	0.5831	<0.0001	31, 3, 1, 1, 0
	K	252	0.9209	<0.0001	54, 25, 15, 4, 0
	L	251	0.96	<0.0001	75, 67, 62, 54, 42
	M	251	0.9793	=0.001	74, 48, 36, 22, 1
	N	251	0.5602	<0.0001	48, 4, 2, 1, 0
	(P)	252	0.98	=0.0013	67, 57, 52, 50, 41
	(Q)	252	0.9545	<0.0001	81, 69, 62, 55, 48
	(R)	252	0.9482	<0.0001	74, 55, 51, 48, 40
	(S)	252	0.8901	<0.0001	62, 55, 37, 32, 19
	(T)	252	0.9549	<0.0001	85, 77, 75, 71, 60
	(U)	252	0.8067	<0.0001	88, 81, 77, 74, 37
	(W)	252	0.9565	<0.0001	73, 67, 62, 57, 41
	(Y)	253	0.98	=0.0013	75, 69, 65, 63, 57

Table J25. Shapiro-Wilks normality testing and five number summaries for samples extracted from image series 6e10f.

	Unit ID	*n*	S-W *W*	*P*	Five Number Summaries
6e10f	E	253	0.0557	<0.0001	9, 0, 0, 0, 0
	F	252	0.5026	<0.0001	71, 0, 0, 0, 0
	G	255	0.4289	<0.0001	38, 0, 0, 0, 0
	H	252	0.1881	<0.0001	37, 0, 0, 0, 0
	I	253	\	\	0, 0, 0, 0, 0
	J	252	0.0738	<0.0001	8, 0, 0, 0, 0
	K	252	0.6188	<0.0001	49, 7.5, 0, 0, 0
	L	251	0.9686	<0.0001	90, 73, 64, 51, 29
	M	251	0.8759	<0.0001	78, 42, 18, 0, 0
	N	251	0.3304	<0.0001	55, 0, 0, 0, 0
	(P)	252	0.9797	=0.0011	73, 56, 48, 44, 28
	(Q)	252	0.9415	<0.0001	95, 77, 61.5, 52, 43
	(R)	252	0.9307	<0.0001	91, 56, 48, 41, 27
	(T)	252	0.7776	<0.0001	102, 90, 85, 79, 28
	(U)	252	0.8616	<0.0001	111, 94, 88.5, 76.5, 20
	(W)	252	0.9701	<0.0001	86, 72, 63, 54, 29
	(Y)	253	0.9601	<0.0001	83, 75, 71, 64, 47

Table J26. Results of Kruskall-Wallis testing, SNK multiple range test on ranked data (α=0.05), and Spearman's ranked correlation on image series 6_10.

	K-W *H*	DF	*P*	SNK Grouping	r_s	*P*
6r10	967.23	17	<0.0001	T(0) = U(0) > V(0) = Q(0) = W(0) = L(0.25) > P(0) = R(0) = S(0) > M(0.5) > K(0.5) > G(0.5) = F(0.25) > N(1) = J(1) = E(0.5) = I(1.5) = H(1)	-0.811	<0.0001
6r10f	995.7	17	<0.0001	U(0) = T(0) > V(0) > Q(0) = W(0) = L(0.25) > P(0) = R(0) = S(0) > M(0.5) > K(0.5) > G(0.5) = H(1) = N(1) = I(1.5) = F(0.25) = E(0.5 = J(1)	-0.806	<0.0001
6e10	3790.4	17	<0.0001	U(0) = T(0) > Y(0) > Q(0) = W(0) = L(0.25) > P(0) = R(0) > S(0) > M(0.5) > K(0.5) = F(0.25) = G(0.5) > H(1) > N(1) = E(0.5) = I(1.5) = J(1)	-0.799	<0.0001
6e10f	3665.7	16	<0.0001	T(0) = U(0) > Y(0) > Q(0) = L(0.25) = W(0) > R(0) = P(0) > M(0.5) > K(0.5) = F(0.25) > G(0.5) = N(1) > H(1) = J(1) = E(0.5) = I(1.5)	-0.821	<0.0001

APPENDIX K

CLASSIFIED IMAGE OUTPUTS. ALL SUPERVISED (SUP) AND OBJECT-ORIENTED (OO) CLASSIFICATIONS FOR SERIES 1_23, AS WELL AS IMAGES 6r11 AND 4r25, ARE PRESENTED IN CHAPTER 4 OF THE TEXT AND ARE NOT INCLUDED IN THIS APPENDIX

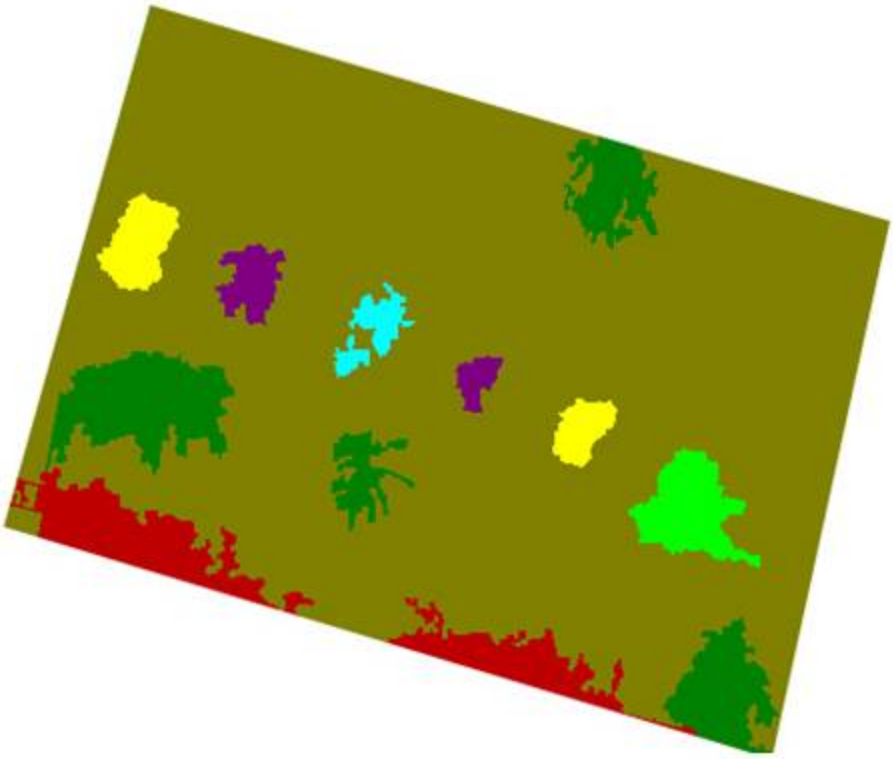

Figure K1. Object-oriented output of image 6r11f.

Figure K2. Supervised output of image 6r11f.

All units, etc.
Readout
Control

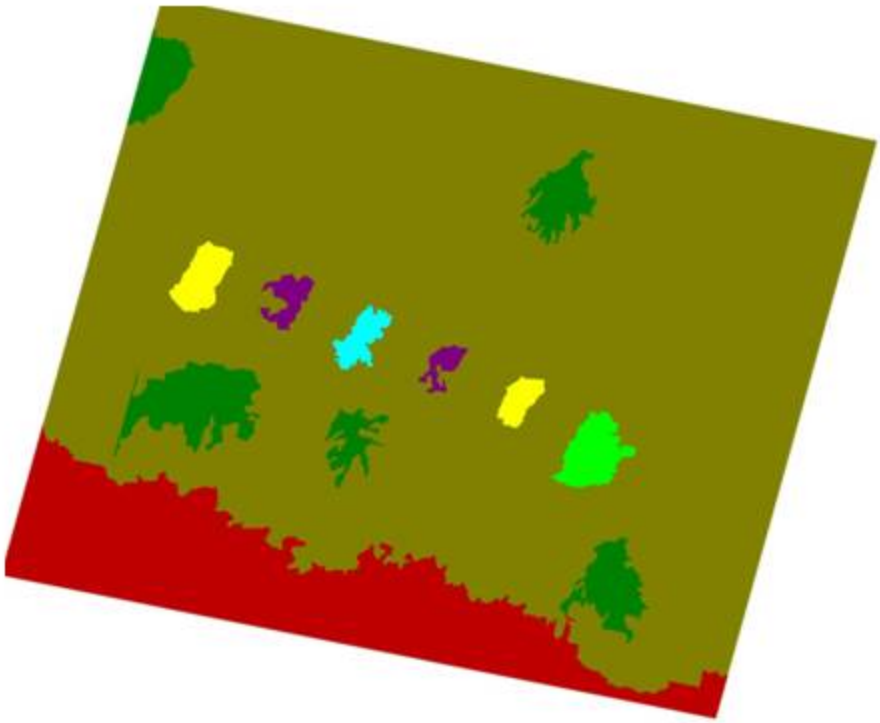

Figure K3. Object-oriented output of image 6e11.

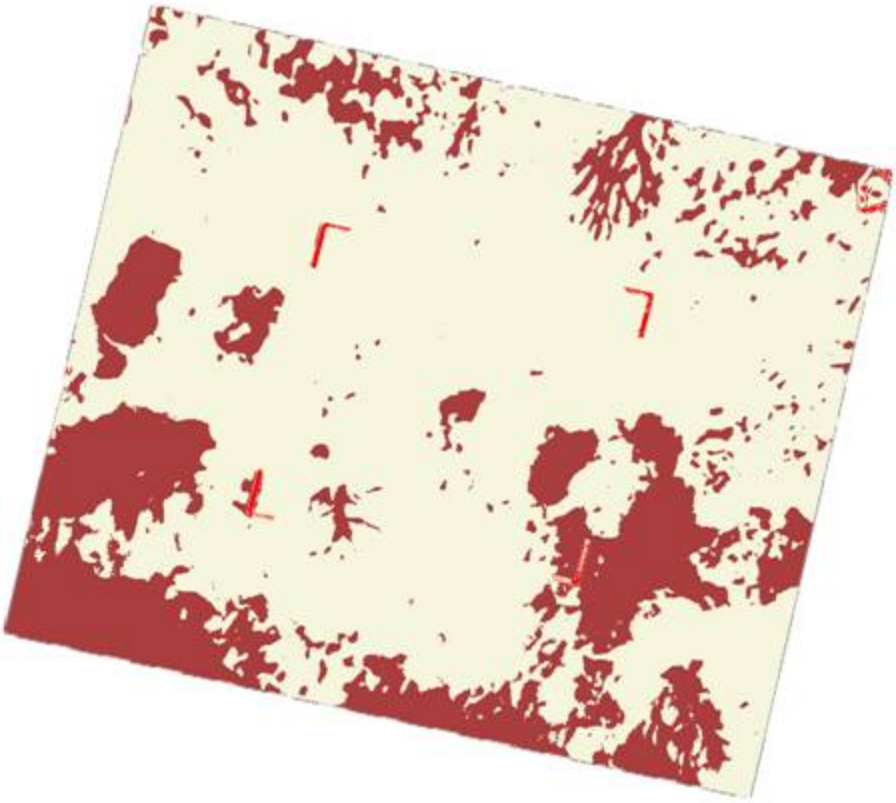

Figure K4. Supervised output of image 6e11.

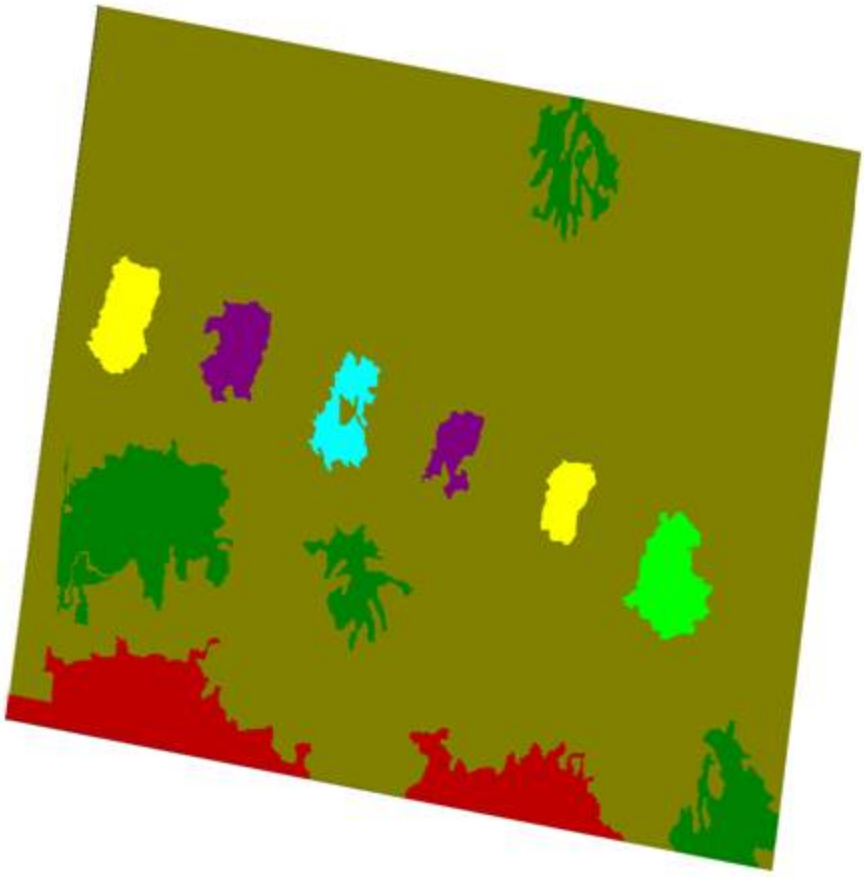

Figure K5. Object-oriented output of image 6e11f.

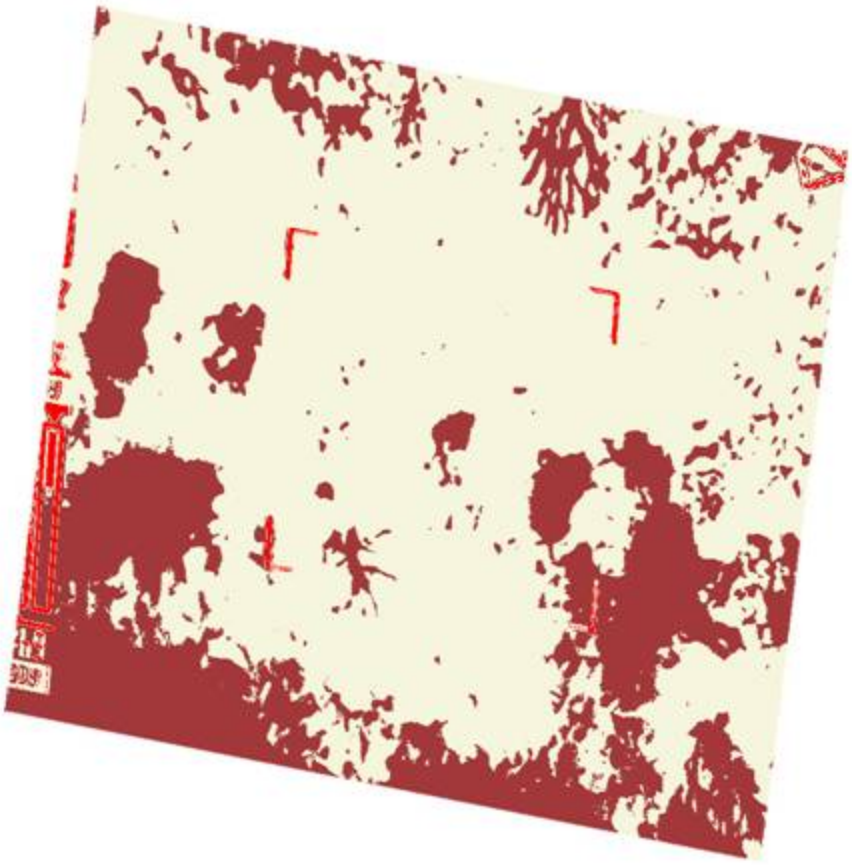

Figure K6. Supervised output of image 6e11f.

All units, etc.
Readout
Control

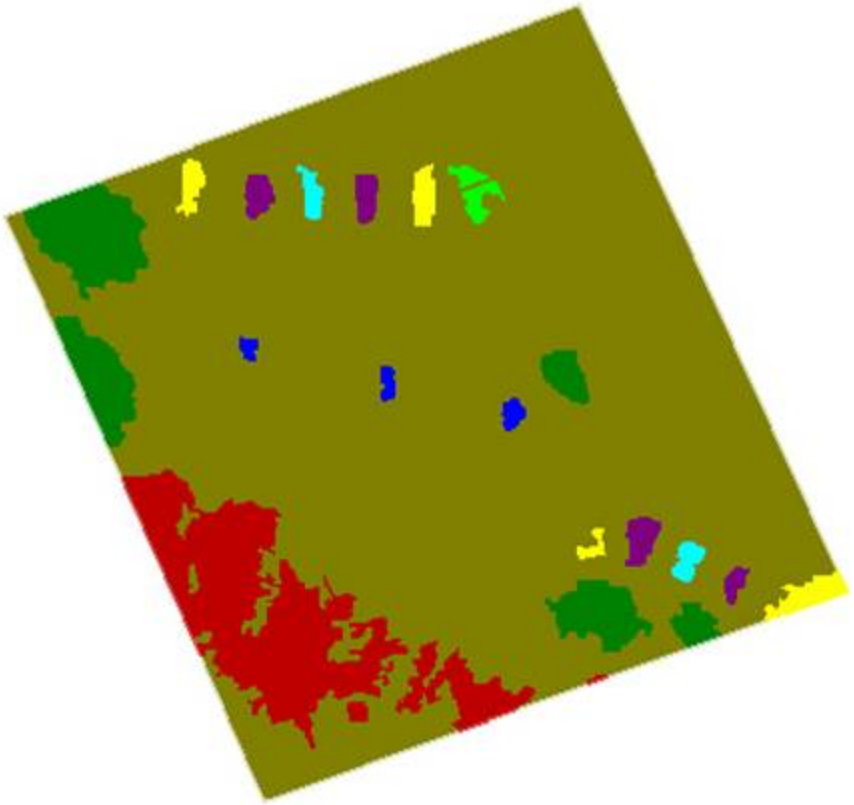

Figure K7. Object-oriented output of image 4r25f.

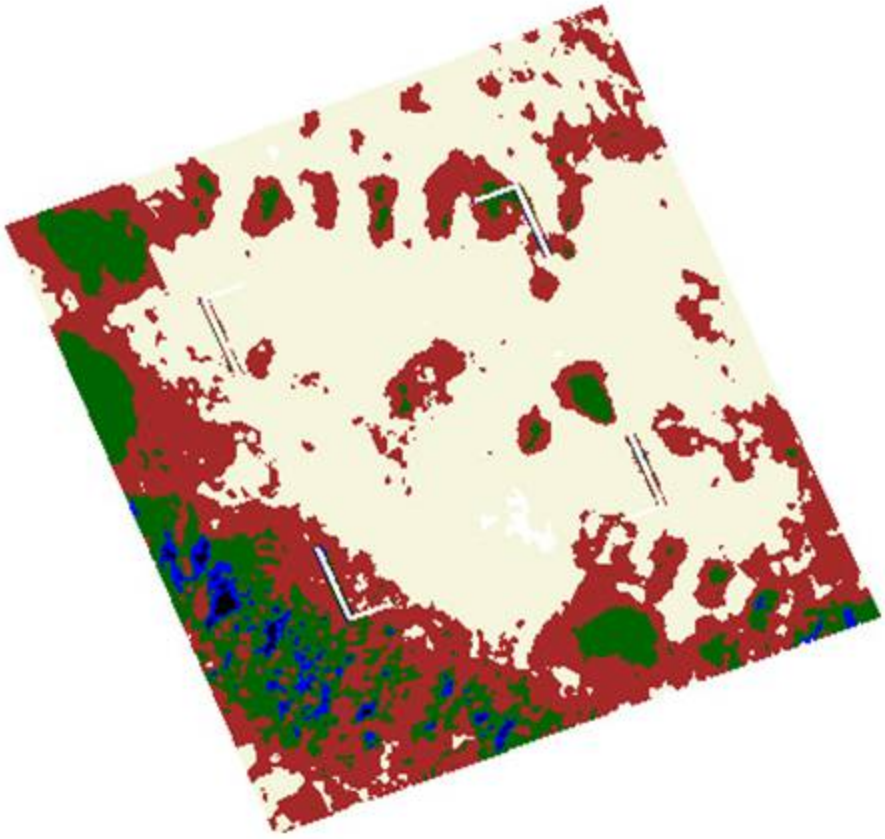

Figure K8. Supervised output of image 4r25f.

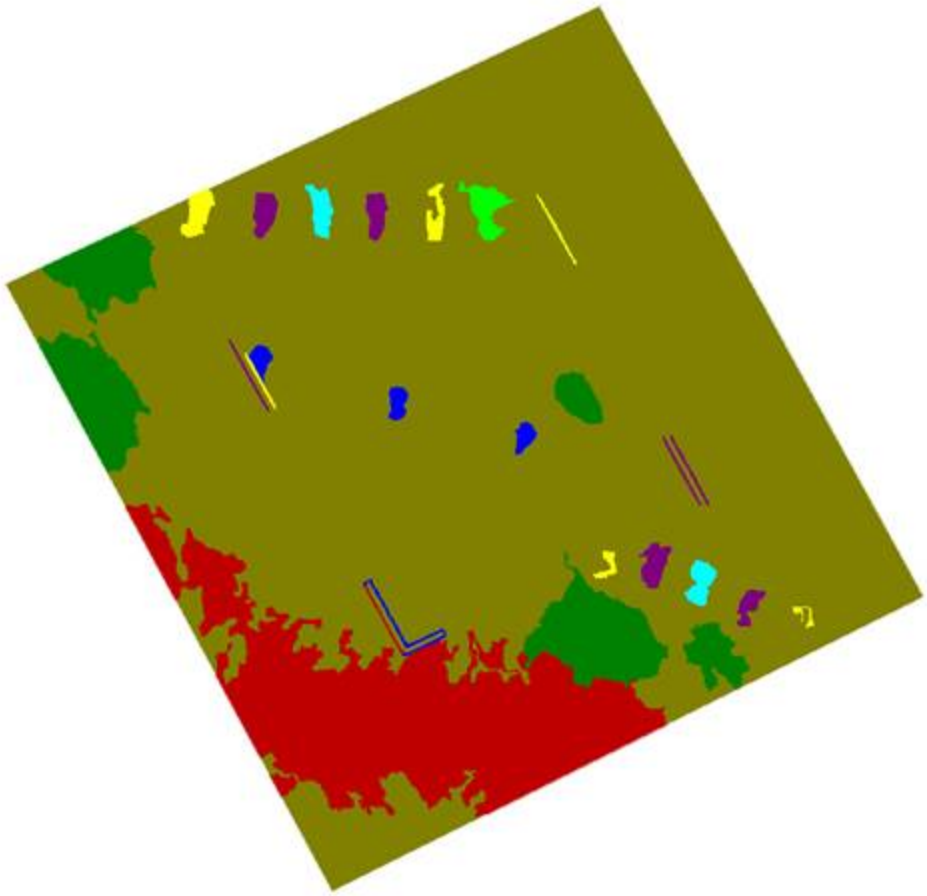

Figure K9. Object-oriented output of image 4e25.

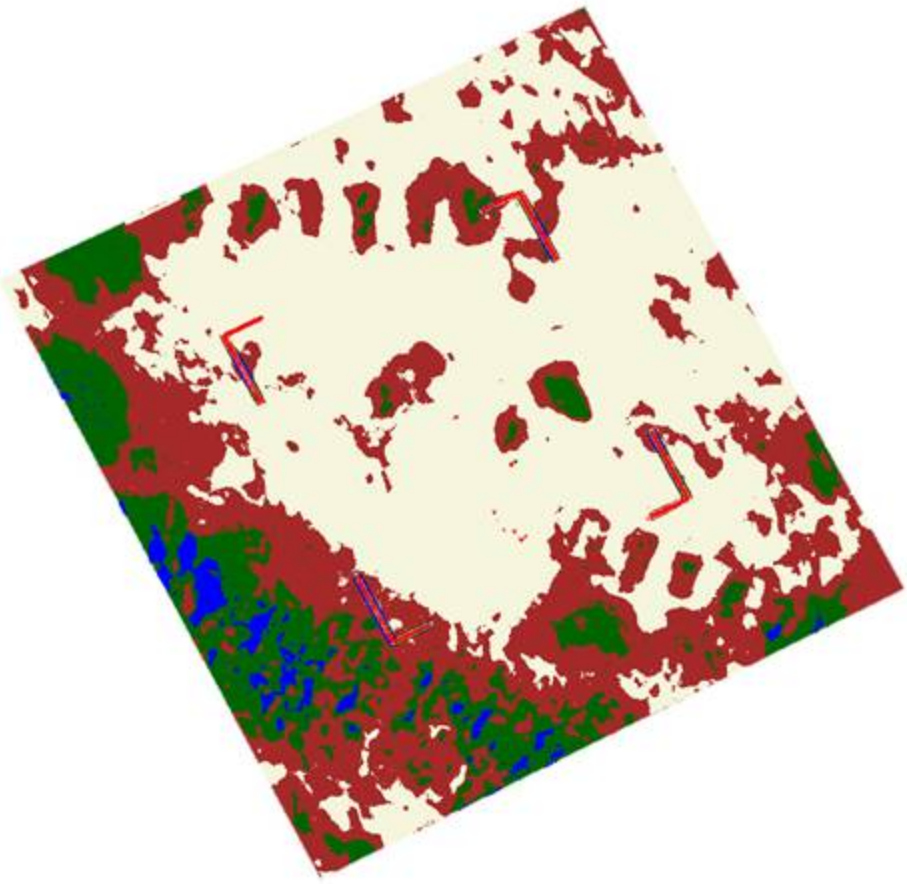

Figure K10. Supervised output of image 4e25.

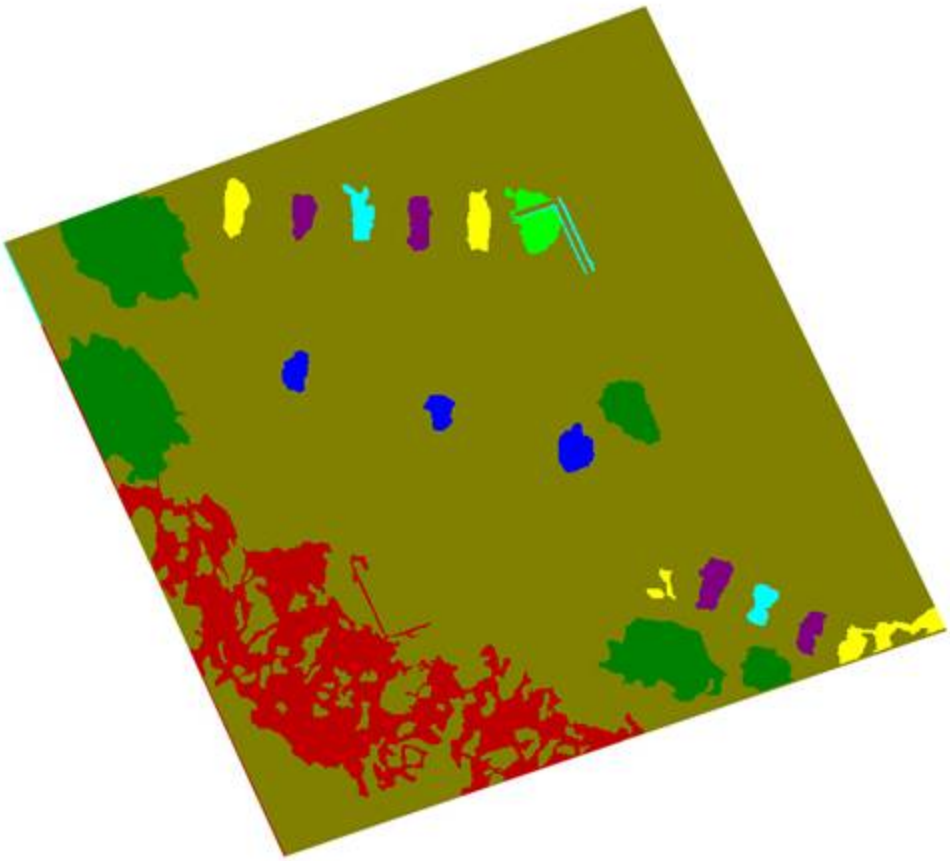

Figure K11. Object-oriented output of image 4e25f.

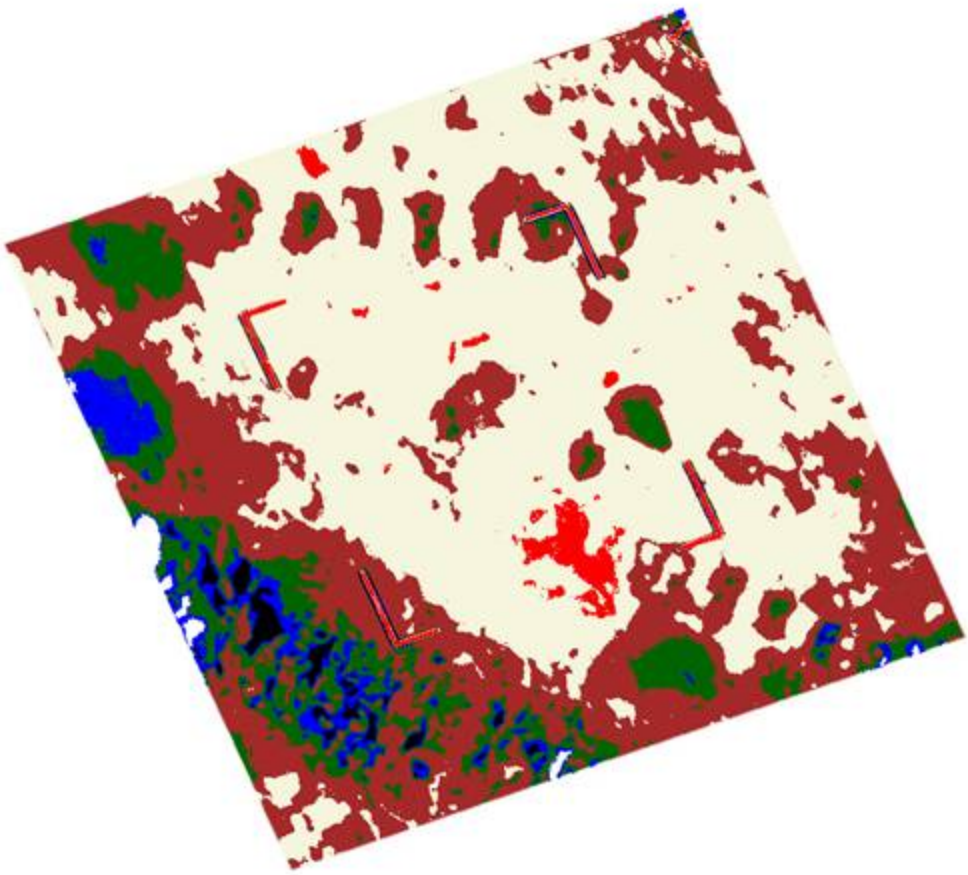

Figure K12. Supervised output of image 4e25f.

APPENDIX L

ACCURACY ASSESSMENTS FOR CLASSIFICATIONS. ALL SUPERVISED (SUP) AND OBJECT-ORIENTED (OO) CLASSIFICATION ACCURACY ASSESSMENTS FOR SERIES 1_23, AS WELL AS IMAGES 6r11 AND 4r25, ARE PRESENTED IN CHAPTER 4 OF THE TEXT AND ARE NOT INCLUDED IN THIS APPENDIX

Table L1. Accuracy assessment for object-oriented classification of image 6r11f.

Class Name	Classified Totals	Number Correct	Producer Accuracy	User Accuracy	Conditional Kappa
1.5 meter units	2023	2023	100.00%	100.00%	1
1.0 meter unit	720	720	100.00%	100.00%	1
0.5 meter unit	887	887	100.00%	100.00%	1
0.25 meter unit	295	295	100.00%	100.00%	1
Control	7232	7232	100.00%	100.00%	1
Trees	1674	1674	100.00%	100.00%	1
Ditch	21037	21037	100.00%	100.00%	1
Total	**33868**	**33868**			
Overall Accuracy	**100.00%**				
Overall Kappa	**1.00**				

Table L2. Accuracy assessment for the supervised classification output for image 6r11f.

Class Name	Reference Totals	Classified Totals	Number Correct	Producer Accuracy	User Accuracy	Conditional Kappa
Unit, etc.	24	25	23	95.83%	92.00%	0.872
Control	39	39	37	94.87%	94.87%	0.8687
Readout	1	0	0	0.00%	\	0
Total	**64**	**64**	**60**			
Overall Accuracy 93.75%						
Overall Kappa 0.8704						

Table L3. Accuracy assessment for object-oriented classification of image 6e11.

Class Name	Classified Totals	Number Correct	Producer Accuracy	User Accuracy	Conditional Kappa
1.5 meter units	7774	7774	100.00%	100.00%	1
1.0 meter unit	3092	3092	100.00%	100.00%	1
0.5 meter unit	3348	3348	100.00%	100.00%	1
0.25 meter unit	4035	4035	100.00%	100.00%	1
Control	30994	33094	100.00%	100.00%	1
Trees	9081	9081	100.00%	100.00%	1
Ditch	130714	130714	100.00%	100.00%	1
Total					
Overall Accuracy	**100.00%**				
Overall Kappa	**1.00**				

Table L4. Accuracy assessment for the supervised classification output for image 6e11.

Class Name	Reference Totals	Classified Totals	Number Correct	Producer Accuracy	User Accuracy	Conditional Kappa
Unit, etc.	19	16	13	68.42%	81.25%	0.7333
Control	45	48	42	93.33%	87.50%	0.5789
Readout	0	0	0	\	\	0
Total	**64**	**64**	**55**			
Overall Accuracy	**85.94%**					
Overall Kappa	**0.6471**					

Table L5. Accuracy assessment for object-oriented classification of image 6e11f.

Class Name	Classified Totals	Number Correct	Producer Accuracy	User Accuracy	Conditional Kappa
1.5 meter units	6846	6846	100.00%	100.00%	1
1.0 meter unit	3069	3069	100.00%	100.00%	1
0.5 meter unit	5140	5140	100.00%	100.00%	1
0.25 meter unit	4359	4359	100.00%	100.00%	1
Control	32331	32331	100.00%	100.00%	1
Trees	4520	4520	100.00%	100.00%	1
Ditch	19072	19072	100.00%	100.00%	1
Total	**75337**	**75337**			
Overall Accuracy	**100.00%**				
Overall Kappa	**1.00**				

Table L6. Accuracy assessment for the supervised classification output for image 6e11f.

Class Name	Reference Totals	Classified Totals	Number Correct	Producer Accuracy	User Accuracy	Conditional Kappa
Unit, etc.	18	19	18	100.00%	94.74%	0.9268
Control	44	44	43	97.73%	97.73%	0.9273
Readout	2	1	1	50.00%	100.00%	1
Total	**64**	**64**	**62**			
Overall Accuracy 96.88%						
Overall Kappa 0.9295						

Table L7. Accuracy assessment for object-oriented classification of image 4r25f.

Class Name	Classified Totals	Number Correct	Producer Accuracy	User Accuracy	Conditional Kappa
1.5 meter units	104	104	100.00%	100.00%	1
1.0 meter unit	92	92	100.00%	100.00%	1
0.5 meter unit	264	264	100.00%	100.00%	1
0.25 meter unit	182	182	100.00%	100.00%	1
Old Units	74	74	100.00%	100.00%	1
Control	8688	8688	100.00%	100.00%	1
Trees	331	331	100.00%	100.00%	1
Ditch	1167	1167	100.00%	100.00%	1
Total	**10902**	**10902**			
Overall Accuracy	**100.00%**				
Overall Kappa	**1.00**				

Table L8. Accuracy assessment for the supervised classification output for image 4r25f.

Class Name	Reference Totals	Classified Totals	Number Correct	Producer Accuracy	User Accuracy	Conditional Kappa
Units	2	20	2	100.00%	10.00%	0.071
Trees	3	8	3	100.00%	37.50%	0.3443
Ditch	14	1	1	7.14%	100.00%	1
Control	44	35	33	75.00%	94.29%	0.8171
Readout	1	0	0	\	\	0
Total	**64**	**64**	**39**			
Overall Accuracy 60.94%						
Overall Kappa 0.3543						

Table L9. Accuracy assessment for object-oriented classification of image 4e25.

Class Name	Reference Totals	Classified Totals	Number Correct	Producer Accuracy	User Accuracy	Conditional Kappa
1.5 meter units	491	491	491	100.00%	100.00%	1
1.0 meter unit	792	792	792	100.00%	100.00%	1
0.5 meter unit	737	737	737	100.00%	100.00%	1
0.25 meter unit	724	724	724	100.00%	100.00%	1
Old Units	370	370	370	100.00%	100.00%	1
Control	28639	29940	28639	95.65%	100.00%	0.8346
Trees	2065	2065	2065	100.00%	100.00%	1
Ditch	5031	3730	3730	100.00%	100.00%	1
Total	**38849**	**38849**	**37548**			
Overall Accuracy	**95.65%**					
Overall Kappa	**0.9194**					

Table L10. Accuracy assessment for the supervised classification output for image 4e25.

Class Name	Reference Totals	Classified Totals	Number Correct	Producer Accuracy	User Accuracy	Conditional Kappa
Units	7	20	4	57.14%	20.00%	0.1018
Trees	10	9	5	50.00%	55.56%	0.4733
Ditch	10	1	1	10.00%	100.00%	1
Control	37	34	30	81.08%	88.24%	0.7211
Readout	0	0	0	\	\	0
Total	**64**	**64**	**40**			
Overall Accuracy 62.50%						
Overall Kappa 0.4088						

Table L11. Accuracy assessment for object-oriented classification of image 4e25f.

Class Name	Reference Totals	Classified Totals	Number Correct	Producer Accuracy	User Accuracy	Conditional Kappa
1.5 meter units	1074	1074	1074	100.00%	100.00%	1
1.0 meter unit	871	871	871	100.00%	100.00%	1
0.5 meter unit	603	603	603	100.00%	100.00%	1
0.25 meter unit	753	753	753	100.00%	100.00%	1
Old Units	616	616	616	100.00%	100.00%	1
Control	20716	20019	20019	100.00%	96.64%	1
Trees	1268	1268	1268	100.00%	100.00%	1
Ditch	2059	6745	2059	30.53%	100.00%	0.2574
Unclassified		(3898)				
Total						
Overall Accuracy	**85.33%**					
Overall Kappa	**0.7451**					

Table L12. Accuracy assessment for the supervised classification output for image 4e25f.

Class Name	Reference Totals	Classified Totals	Number Correct	Producer Accuracy	User Accuracy	Conditional Kappa
Units	1	21	0	0.00%	0.00%	-0.0159
Trees	5	7	2	40.00%	28.57%	0.2252
Ditch	10	2	2	20.00%	100.00%	1
Control	48	33	32	67.67%	96.97%	0.8788
Readout	0	1	0	\		0
Total	**64**	**64**	**36**			
Overall Accuracy 56.25%						
Overall Kappa 0.2644						

REFERENCES

Ben-Dor E, Kochavi M, Vinizki L, Shionim M, Portugali J. 2001. Detection of buried walls using airborne thermal video radiometry. International Journal of Remote Sensing 22(18):3689-3702.

Casper's dictum (CD) [Internet]. [created 2007 Oct 12]. BBC Online; [last accessed 2010 Sept 16]. Available from: http://www.bbc.co.uk/dna/h2g2/A27879060

Davenport GC. 2001. Remote sensing applications in forensic investigations. Historical Archaeology 35(1):87-100.

Denton climatology 30-year normals (DC30-yn) [Internet]. [updated 2010]. National Oceanic and Atmospheric Administration (NOAA) National Weather Service Forecast Office [cited 2010 July 15]. Available from: www.srh.weather.gov/fwd/n?=dentonclimatology

Farsiu S, Robinson D, Elad M, Milanfar P. 2004. Advances and challenges in super-resolution. International Journal of Imaging Systems and Technology 14(2):47-57.

Ford A. 1980. Soil survey of Denton County, Texas. U.S. Department of Agricultural Soil Conservation Service (now National Resources Conservation Service). Washington D.C.: The Service. 160 p.

France DL, Griffin TJ, Swanburg JG, Lindemann JW, Davenport GC, Trammell V, Travis CT, Kondratieff B, Nelson A, Castellano K, Hopkins D and Adair T. 1992. A multidisciplinary approach to the detection of clandestine graves. Journal of Forensic Sciences 37(6):1445-1458.

France DL, Griffin TJ, Swanburg JG, Lindemann JW, Davenport GC, Trammell V,Travis CT, Kondratieff B, Nelson A, Castellano K, Hopkins D and Adair T. 1997. Necrosearch revisited: Further multidisciplinary approaches to the detection of clandestine graves. In: Haglund WD, Sorg MH, editors. Forensic taphonomy: The postmortem fate of human remains. 1st ed. New York: CRC Press. p 497-507.

Heath, Ralph C. 1983. Basic ground-water hydrology. US Geological Survey Water-Supply Paper 2220 (revised 2004). Washington D.C.: Government Printing Office. 86 pages.

Irvine JM, Evers TK, Smyre JL, Huff D, King AL, Stahl G, and Odenweller J. 1997. The detection and mapping of buried waste. International Journal of Remote Sensing 18(7):1583-1595.

Jensen JR. 2006. Remote sensing of the environment. 2nd ed. Upper Saddle River: Pearson Prentice Hall. 608 p.

Johnson JR, Lucey PG, and Horton KA. 1998. Infrared measurements of pristine and disturbed soils 1. Spectral contrast differences between field and laboratory data. Remote Sensing of Environment 64(1):34-46.

Killam EM. 1990. The detection of human remains. Springfield: Charles C. Thomas Publishers. p 135-177.

Lu D, Weng Q. 2007. A survey of image classification methods and techniques for improving classification performance. International Journal of Remote Sensing 28(5):823-870.

McMahan C, Fry RG, Brown KL. 1984. The vegetation types of Texas, including cropland: An illustrated synopsis to accompany the map. Wildlife Division, Texas Parks and Wildlife Department. PWB Bulletin 7000-120. 45 p.

National Climatic Data Center (NCDC) weather data [Internet]. [updated 2010]. National Oceanic and Atmospheric Administration (NOAA) Satellite and Information Service. Denton Municipal Airport Regional Marking Station [last accessed 2010 Sept 16]. Available from: http://www.ncdc.noaa.gov/oa/ncdc.html

North Central Texas County of Governments (NCTCOG) Data. 2007. Digital elevation model (two foot contours) tile e23797642a of Denton County, Texas. Arlington (TX): NCTCOG. Created Jan-Mar 2007 [accessed 2010 June 25]. Available at http://www.nctcog.org/ris/GIS

North Central Texas County of Governments (NCTCOG) Data. 2009. Aerial image tile e23797642a of Denton County, Texas. Arlington (TX): NCTCOG. Created Feb-Mar 2009 [accessed 2010 Mar 10]. Available at http://www.nctcog.org/ris/GIS

Ritter N. 2007. Missing persons and unidentified remains: the nation's silent mass disaster. NIJ Journal 256:1-7 [Internet]. [cited 2010 Mar 21]. Available from: http://www.ojp.usdoj.gov/nij/journals/256/missing-persons.html

Park SC, Park MK, Kang MG. 2003. Super-resolution image construction: A technical overview. IEEE Signal Processing Magazine 20(3):21-36.

Rodriguez WC, Bass WM. 1985. Decomposition of buried bodies and methods that may aid in their location. Journal of Forensic Sciences 30(3):836-852.

Saul JM, Saul FP, Thompson LM. 2007. Recovery and documentation of skeletal remains: A brief field guide. Austin: University of Texas Press.56 p.

Sever TL, Wagner DW. 1991. Analysis of prehistoric roadways in Chaco Canyon using remotely sensed data. In: Trombold CD, editor. Ancient road networks and settlement hierarchies in the New World. Cambridge: Cambridge University Press. p 42-52.

Scollar I, Tabbagh A, Hesse A, Herzog I. 1990. Archaeological prospecting and remote sensing. Cambridge: Cambridge University Press. Chapter 10, Thermal Prospecting; 591-635.

Sheets P, TL Sever. 1991. Prehistoric footpaths in Costa Rica: Transportation and communication in a tropical rainforest. In: Trombold CD, editor. Ancient road networks and settlement hierarchies in the New World. Cambridge: Cambridge University Press. p 53-62.

Whiteside T, Ahmad W. 2005. A comparison of object-oriented and pixel-based classification methods for mapping land cover in Northern Australia. Proceedings of SSC2005 Spatial Intelligence, Innovation and Praxis: the National Biennial Conference of the Spatial Sciences Institute. Melbourne: Spatial Sciences Institute.

Willhauck G. 2000. Comparison of object oriented classification techniques and standard image analysis for the use of change detection between SPOT multispectral satellite images and aerial photos. International Archives of Photogrammetry and Remote Sensing 33(B3):214-221.

Winter EM, Schlangen MJ, Bowman AP, Carter MR, Bennett CL, Fields DJ, Aimonetti WD, Lucey PG, Johnson JR, Horton KA, Williams TJ, Stocker AD, Oshagan A, DePersia AT, and Sayre CJ. 1996. Experiments to support the development of techniques for hyperspectral mine detection. Proceedings of the International Society of Optical Engineering (SPIE) 2759:139-148.

Yan G, Mas JF, Maathuis BHP, Xiangmin Z, Van Dikj PM. 2006. Comparison of pixel-based and object-oriented image classification approaches- a case study in a coal fire area, Wuda, Inner Mongolia, China. International Journal of Remote Sensing 27(18):4039-4055.